Quantum Transport in Strained Single-wall Carbon Nanotube Transistors

Linxiang Huang

A Thesis
in
The Department
of
Physics

Presented in Partial Fulfillment of the Requirements
for the Degree of Master of Science (Physics) at
Concordia University
Montréal, Québec, Canada

January 2021

Concordia University
School of Graduate Studies

This is to certify that the thesis prepared

By: **Linxiang Huang**

Entitled: **Quantum Transport in Strained Single-wall Carbon Nanotube Transistors**

and submitted in partial fulfillment of the requirements for the degree of

Master of Science

complies with the regulations of this University and meets the accepted standards with respect to originality and quality.

Signed by the final examining commitee:

_____ Examiner

Dr. Saurabh Maiti

_____ Examiner

Dr. Ingo Salzmann

_____ Supervisor

Dr. Alexandre Champagne

Approved by _____

Dr. Alexandre Champagne, Chair of Department

_____ 20 ____ _____

Dr. Pascale Sicotte, Dean of the Faculty of Arts and Science

Abstract

Quantum Transport in Strained Single-wall Carbon Nanotube Transistors

Linxiang Huang

Can we control quantum interferences and many-body interactions mechanically, i.e. by pulling on a nano-system? While many idealized theoretical proposals address this question, very few have been realized experimentally. To bridge this gap with single-wall carbon nanotubes (SWCNTs), we are developing simultaneously an experimental platform and an applied theoretical model. I have nanofabricated several high quality strain-tunable suspended SWCNT transistors. I first located and characterized SWCNTs (diameters $\leqslant$ 2 nm) grown by our former group member Andrew McRae, using scanning electron microscopy (SEM) and atomic force microscopy (AFM). I patterned nanoscale bowtie-shaped gold break junctions ($\approx$ 300 nm wide) on top of SWCNTs, using electron beam lithography (EBL). Finally, I suspended these break junctions by removing the supporting SiO_2 beneath them, using a buffered oxide etch (BOE). After opening nanogaps in gold break junctions via electromigration, it will allow straining of ultra-short SWCNT channels ($\approx$ 20 nm) with our custom-built quantum transport strain engineering (QTSE) platform. Besides the fabrication, I have also extended and modified the previous applied theory from describing strain transport behaviors in graphene to those in SWCNTs. This theoretical model considers dominant uniaxial strain effects on the band structure and all relevant experimental parameters. In quasi-metallic SWCNTs, I predicted that the uniaxial strain can widely tune conductance, leading to outstanding quantum transistors. In metallic ones, I observed a valley filter behaviour where electrons are only allowed to flow through certain valleys of the band structure. In semiconducting ones, I predicted the strong tunability of electron-hole asymmetry via uniaxial strain, which would permit us to engineer two vastly different transport behaviors into a single device.

Acknowledgements

I couldn't complete my MSc degree without the help from people I met during this two and half a year. Firstly, I would like to thank my supervisor Alex, for showing me the importance of being passionate about physics and giving me advices on how to produce good work. I am so grateful for having the opportunity to continue to my PhD after a MSc in Champagne group. I would also like to thank my colleagues: To Andrew, thanks for showing me the ropes and getting me started. Although we only met twice in person, your patience and kindness impressed me a lot. To Mattew and Gareth, thanks for all your help and advices. I really enjoy talking with you about research and cultures. To Israel, thank you for helping me orient myself in the lab and our discussions have been very fruitful. I look forward to working with you in next few years. To Guoqing, thank you a lot for showing me how to do high-quality fabrication. I believe we will meet in China someday after your graduation. To Fernanda and Wyatt, it has been such a pleasure to take courses with you in our department. Finally, to my family members, thanks for understanding and supporting me in pursuing a MSc abroad. Without your kindness and help, all of these would not have been possible.

Contents

List of Figures

List of Abbreviations

ac	Alternating Current.
AFM	Atomic Force Microscope.
BOE	Buffered Oxide Etch.
CAD	Computer Aided Design.
CNT	Carbon Nanotube.
CPD	Critical Point Drying.
CVD	Chemical Vapour Deposition.
DI	Deionized.
e-h	Electron-hole.
EBL	Electron Beam (e-beam) Lithography.
EL	Ethyl Lactate.
FBZ	First Brillouin Zone.
GQSTs	Graphene Quantum Strain Transistors.
H.c.	Hermitian Conjugate.
HMDS	Hexamethyldisilazane.
IPA	Isopropyl Alcohol.
MIBK	Methyl Isobutyl Ketone.
MWCNT	Multi-Walled Carbon Nanotube.
NEMS	Nanoelectromechanical Systems.
NN	Nearest-Neighbor.
NNN	Next-Nearest-Neighbor.
PMMA	Polymethyl Methacrylate.
QD	Quantum Dot.
QTSE	Quantum Transport Strain Engineering.
RIE	Reactive Ion Etching.
rpm	Rotations per Minute.
SEM	Scanning Electron Microscope.
SWCNT	Single Walled Carbon Nanotube.
TPI	Threads per Inch.

Chapter 1

Introduction to Strained Single-wall Carbon Nanotube NEMS

Nanoelectronmechanical systems (NEMS) are used to study the rich physics of electromechanics and explore potential device applications, such as coherent electron transport [1], strong electron correlations [2], electron-vibron couplings [3], etc. Low-dimensional carbon materials such as graphene and single-wall carbon nanotubes (SWCNTs) are an ideal playground for quantum NEMS, because they are mechanically flexible and robust [4–6], their electronics are very sensitive to mechanical deformation [7, 8] and their charge carriers have long mean free paths even at room temperature [9]. Despite numerous proposals to use mechanical strain to engineer transport in graphene/SWCNT NEMS [8, 10–14], experimental progress has been slow because of challenges in fabricating devices and instrumentation, as well as the idealization of theoretical models [10, 15–17].

Our group built a platform for quantum transport strain engineering (QTSE) of one dimensional (1D) and two dimensional (2D) systems. It allows me to apply large, tunable, and gate-independent uniaxial strain at low temperature ($T \approx 0.3$ K). So far, no one had made any strain-tunable suspended SWCNT devices compatible with this platform. During my MSc, I have fabricated six high-quality devices on four thin Si chips. To guide electronic transport measurements in these existing devices, I extended and modified the previous applied theory from graphene to describe SWCNT transistors. I predicted that the uniaxial strain can generate valley polarization in metallic tubes, create outstanding quantum strain transistors in quasi-metallic tubes, and tune two vastly different behaviours for hole and electron charge carriers in semiconducting tubes.

In this chapter, I first introduce the physical and electronic structure of SWCNTs, then discuss recent results of carbon nanotube NEMS, and the organization of this thesis.

1.1 Lattice and Electronic Structure of SWCNTs

I describe the lattice and band structure of single-wall carbon nanotubes. The Hamiltonian presented for unstrained SWCNTs in this section, will be modified later in Chapter 3 to calculate conductance in strained SWCNTs.

One or more layers of graphene can be rolled up into single-wall or multi-wall carbon nanotubes, respectively. CNTs can be synthesized using various methods, such as laser vaporization [18], arc-discharge [19], chemical vapor deposition (CVD), etc. Their diameters range from $\sim$ 1 nm to 100s of nm. Because of the simplicity of SWCNTs, they are the most studied both experimentally and theoretically. In this thesis, I will discuss strain transport behavior in SWCNTs.

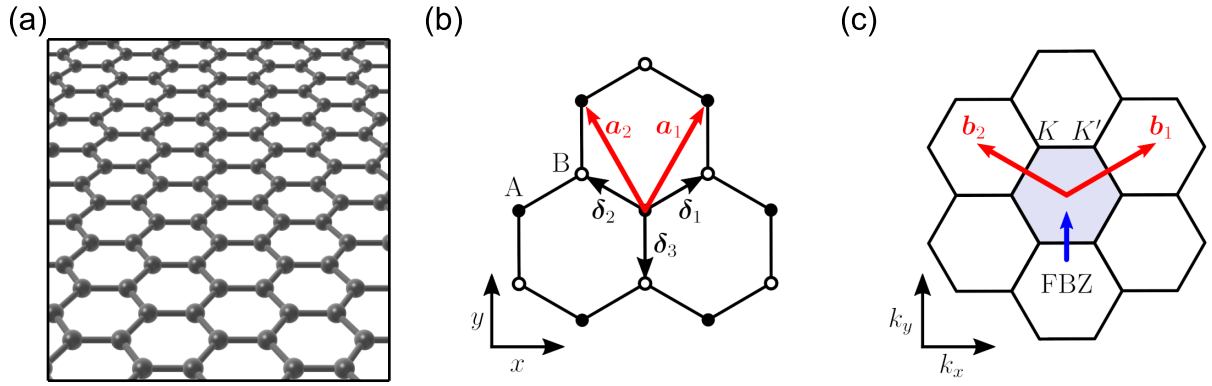

Figure 1.1: Lattice structure of graphene. (a) 3D rendered lattice of graphene. (b) Graphene lattice has a two-atom basis, (A,B). $\boldsymbol{\delta}_n$ are the nearest-neighbour vectors, while $\boldsymbol{a}_1$, $\boldsymbol{a}_2$ are the primitive lattice vectors. (c) Graphene lattice in reciprocal space shows K and K' valleys located at the corners of the first Brillouin zone, which correspond to the two sublattices in real space. Figure adapted from Ref. [20]

I start by describing the lattice structure of monolayer graphene, because SWCNTs are simply rolled-up monolayer graphene. Monolayer graphene is a 2 dimensional material made out of carbon atoms arranged in a honeycomb lattice, which has a three-fold rotational symmetry, see Fig. 1.1(a).

Carbon atoms form in-plane σ bonds because of the sp^2 hybridization, leading to the robust mechanical properties [21]. Only electrons in the out-of-plane π orbital contribute to the conductivity of graphene in the low-energy regime. Figure 1.1(b) shows that there are two sublattices in graphene, labelled A and B, separated with a distance of $a = 1.42$ Å. x and y axes are along the zigzag and armchair directions, respectively. We can write the

nearest-neighbour vectors $\boldsymbol{\delta}_n$ as [22]:

$$\boldsymbol{\delta}_1 = \frac{a}{2}\left(\sqrt{3}, 1\right), \quad \boldsymbol{\delta}_2 = \frac{a}{2}\left(-\sqrt{3}, 1\right), \quad \boldsymbol{\delta}_3 = a\left(0, -1\right), \tag{1.1}$$

and the primitive vectors $\boldsymbol{a}_1$, $\boldsymbol{a}_2$ are [22]:

$$\boldsymbol{a}_1 = \frac{a}{2}\left(\sqrt{3}, 3\right), \qquad \boldsymbol{a}_2 = \frac{a}{2}\left(-\sqrt{3}, 3\right). \tag{1.2}$$

In Fig. 1.1(c), I show the first Brillouin zone (FBZ), K and K' valleys, and reciprocal lattice vectors $\boldsymbol{b}_1$, $\boldsymbol{b}_2$. They can be calculated from the real space primitive vectors:

$$\boldsymbol{b}_1 = \frac{2\pi}{3a}\left(\sqrt{3}, 1\right), \qquad \boldsymbol{b}_2 = \frac{2\pi}{3a}\left(-\sqrt{3}, 1\right) \tag{1.3}$$

Analogous to the two atom basis in real space, there are two asymmetric corners of the FBZ, known as K and K' valleys. The positions of three K points can be written as [22]:

$$\boldsymbol{K}_1 = \frac{4\pi}{3\sqrt{3}a}\left(1, 0\right), \quad \boldsymbol{K}_2 = \frac{4\pi}{3\sqrt{3}a}\left(-\frac{1}{2}, \frac{\sqrt{3}}{2}\right), \quad \boldsymbol{K}_3 = \frac{4\pi}{3\sqrt{3}a}\left(-\frac{1}{2}, -\frac{\sqrt{3}}{2}\right) \tag{1.4}$$

Positions of those three K' points in momentum space can simply be found using the valley symmetry: $\boldsymbol{K}'_i = -\boldsymbol{K}_i$.

We use the tight binding (TB) model to determine the band strucutre of graphene. When only considering the nearest- and next-nearest neighbors, The electronic Hamiltonian can be written as [22, 23]:

$$H = -\gamma_0 \sum_{k,n} e^{-i\boldsymbol{k}\cdot\boldsymbol{\delta}_n}\left(a_k^\dagger b_k + \text{H.c.}\right) - \gamma_0' \sum_{k,\langle n,m\rangle} e^{-i\boldsymbol{k}\cdot\boldsymbol{\delta}_{nm}}\left(a_k^\dagger a_k + b_k^\dagger b_k + \text{H.c.}\right) \tag{1.5}$$

where $\gamma_0 \approx 2.7$ eV [22] and $\gamma_0' \approx 0.1\gamma_0 \approx 0.3$ eV [24] are the hopping energies for the nearest and next-nearest neighbors respectively. $\boldsymbol{\delta}_{nm} = \boldsymbol{\delta}_n - \boldsymbol{\delta}_m$ ($n \neq m$) represent the next-nearest neighbor vectors. $a_k^{(\dagger)}$, $b_k^{(\dagger)}$ destroys (creates) an electron with momentum k on sublattice A, B respectively. H.c. is the Hermitian conjugate. We can now determine the dispersion relation in graphene/SWCNTs [22, 23]:

$$E = \pm\left|\gamma_0 \sum_{k,n} e^{-i\boldsymbol{k}\cdot\boldsymbol{\delta}_n}\right| - \gamma_0' \sum_{k,\langle n,m\rangle} \cos\left(\boldsymbol{k}\cdot\boldsymbol{\delta}_{nm}\right) \tag{1.6}$$

where $\pm$ describe the conduction and valence bands, where electrons and holes are charge carriers respectively. After replacing $\boldsymbol{\delta}_n$, $\boldsymbol{\delta}_{nm}$ in the above equation, we can simplify the dispersion to [22]:

$$E_\pm(\boldsymbol{k}) = \pm\gamma_0\sqrt{3 + f(\boldsymbol{k})} - \gamma_0' f(\boldsymbol{k}) \tag{1.7}$$

$$f(\boldsymbol{k}) = 2\cos\left(\sqrt{3}k_x a\right) + 4\cos\left(\frac{\sqrt{3}}{2}k_x a\right)\cos\left(\frac{3}{2}k_y a\right) \tag{1.8}$$

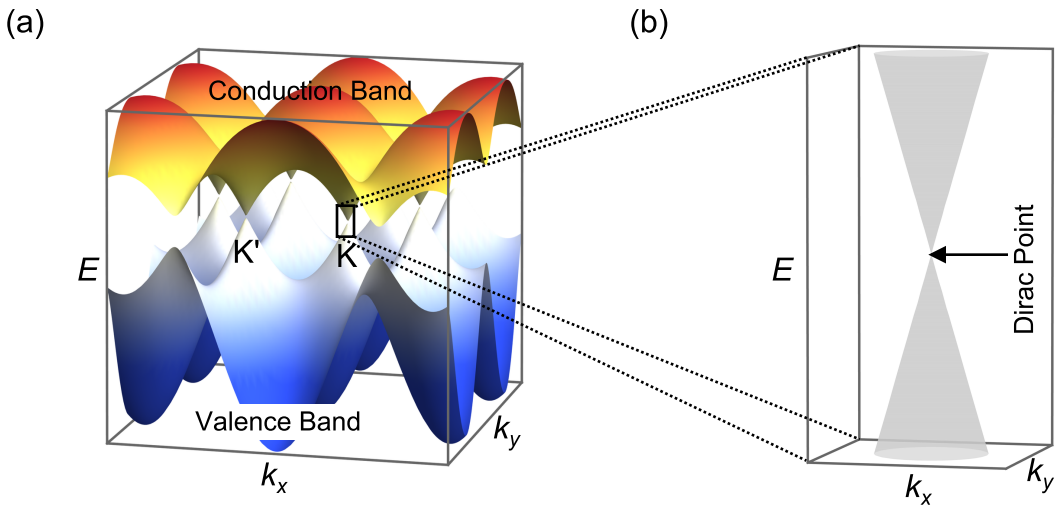

Figure 1.2: Band structure of graphene. (a) The conduction and valence bands touch at the Dirac points K, K'. (b) Zoom-in on the low-energy dispersion, i.e. the Dirac cones.

The second term arises from the next-nearest neighbor hopping energy γ_0', and causes the asymmetry between the conduction and valence bands. Figure 1.2(a) shows the 3D plot of the full graphene band structure, where contact points between two bands are Dirac points in K, K' valleys.

In the low-energy regime, the second term only shifts the energy of Dirac points without modifying the shape of band structure, which are called Dirac cones [22]:

$$E_{\pm}(\boldsymbol{k}) - E_{\mathrm{D}} = \pm\hbar v_F |k| \tag{1.9}$$

where E_{D} is the energy of Dirac point, and $v_F = 3|\gamma_0|/2\hbar = 8.8 \times 10^5$ m/s is the slope of the Dirac cones, known as the Fermi velocity [22]. Figure 1.2(b) shows the low-energy linear and isotropic dispersion. In analogy to photons, charge carriers (electrons and holes) in graphene propagate at a constant v_{F}, and behaves relativistically. The charge carriers are Dirac fermions, and described by:

$$H = \hbar v_F \boldsymbol{\sigma} \cdot \boldsymbol{k} \tag{1.10}$$

where $\boldsymbol{\sigma}$ are the Pauli spin matrices:

$$\sigma_x = \begin{pmatrix} 0 & 1 \\ 1 & 0 \end{pmatrix}, \qquad \sigma_y = \begin{pmatrix} 0 & -i \\ i & 0 \end{pmatrix} \tag{1.11}$$

Single-wall carbon nanotubes are equivalent to rolled-up graphene strips. Compared to graphene, the SWCNT Hamiltonian is similar in unstrained tubes, but now there is an

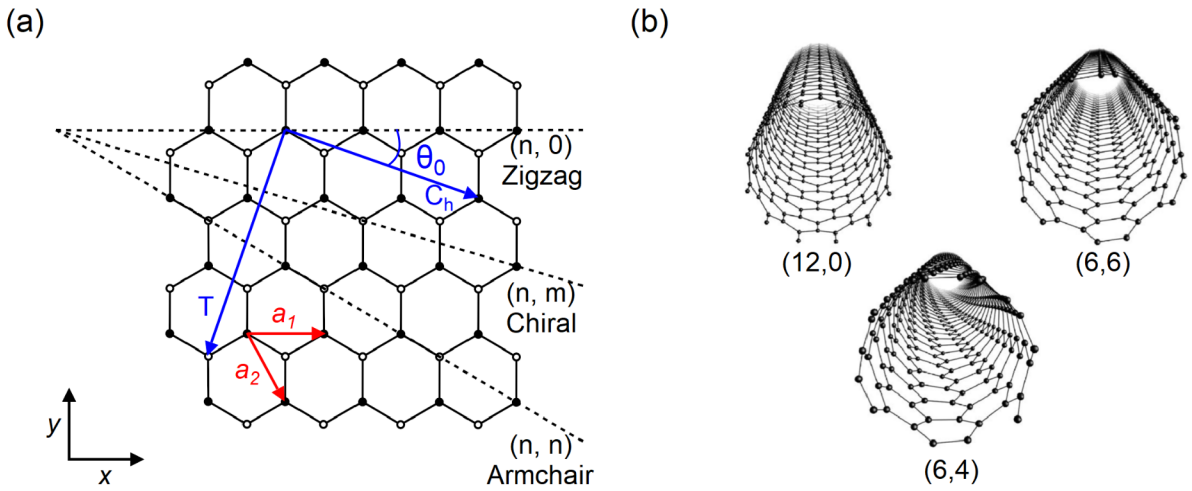

Figure 1.3: From monolayer graphene to SWCNTs. (a) The chiral vector $\boldsymbol{C}_h$ defines the wrapping direction of SWCNTs. (b) Images of zigzag (12,0), armchair (6,6) and chiral (6,4) SWCNTs. Figure adapted from [20, 25].

additional periodic boundary conditions along the circumference. I now discuss the way SWCNTs are rolled and how it influences the SWCNT electronic properties. In Fig. 1.3(a), the rolling direction is represented by the chiral vector $\boldsymbol{C}_h = (n\boldsymbol{a}_1, m\boldsymbol{a}_2)$, where n, m are integers. The translation vector $\boldsymbol{T}$ can be used to determine the unit cell area of SWCNTs. The angle between $\boldsymbol{C}_h$ and zigzag direction $(n, 0)$ is defined as the chiral angle θ_0. Figure 1.3(b) shows examples of three different types of SWCNTs based on their chirality (chiral angles): zigzag, chiral, and armchair. Chiral vectors are along $(n, 0)$ in zigzag SWCNTs, (n, n) in armchair ones, and (n, m) in chiral ones, where $n \neq m$.

The SWCNT band structure is determined by its chirality. Momentum along the circumference $k_\perp$ is quantized due to the periodic boundary conditions. This turns the Dirac cone into a set of discrete vertical planar cuts in the $k_\parallel$ direction (i.e. subbands) [25, 26]. If one of these cuts intersects a Dirac point, then the tube is metallic ($n = m$) or quasi-metallic ($n - m = 3I$, where I is an integer [27]) as there is no bandgap. Otherwise, the tube is semiconducting with a bandgap determined by the SWCNT diameter, d, such that [28]:

$$E_g = \frac{2|q|\gamma_0 a}{d\cos(\theta)} - \frac{q\gamma_0 a^2}{3d^2\cos^2(\theta)} \tag{1.12}$$

where $q = 0, \pm 1$ is the remainder of $n/3$, and $d\cos(\theta) = (2n + m)\sqrt{3}a/2\pi$. Note that this approximation is not accurate when the bandgap from curvature-induced strain is not negligible [29]. Figure 1.4 (a)-(b) show the band structure of metallic and semiconducting

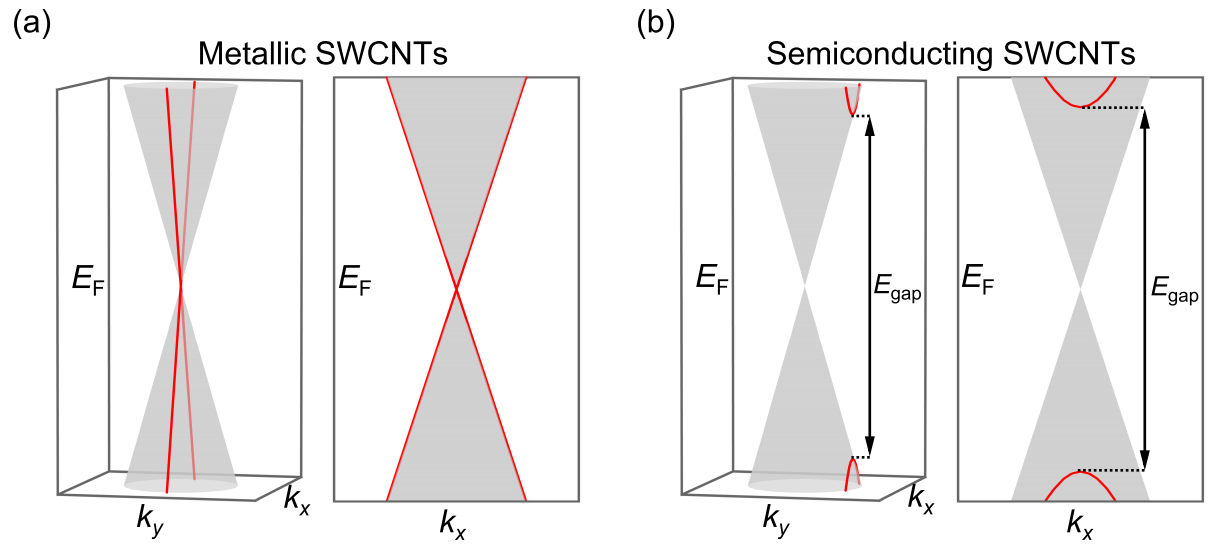

Figure 1.4: Band structure of SWCNTs. (a) In metallic SWCNTs, a subband crosses Dirac points, leading to a linear dispersion without a bandgap. (b) In semiconducting SWCNTs, no subband crosses Dirac points, leading to a parabolic dispersion with a bandgap.

SWCNTs respectively.

1.2 Recent Literature Results in SWCNT NEMS

With static strains in SWCNTs, it is possible to explore a wide range of quantum physics, such as electron-vibron couplings [3], Kondo effect [30], etc. Unfortunately, the experimental progress in this field has been slow mainly because of challenges to make strain-tunable SWCNT devices and the lack of instrumentation to apply a large, tunable, gate-independent strain, compatible with low-temperature transport measurements [31–33]. I mention here some of the best experimental work done so far to understand strain transport in SWCNT NEMS.

Tunable strains have been applied to nanotubes with atomic force microscopy (AFM) tips [34]. The inset of Fig. 1.5(a) shows an AFM tip pushing on a suspended SWCNT to induce local (non-uniform) strain. Main panel shows that with an increasing strain up to 2%, room-temperature conductance decreases. This indicates the opening of a bandgap in the tube. Substrate topography has been recently used to generate static strains in SWCNTs to realize charge fractionalization [32]. As shown in Fig. 1.5(b), by placing a wedge-shaped pillar under a suspended metallic tube, different strains could be created in different sections of the tube. An axial magnetic field was applied. At a certain range of field, fractionalized

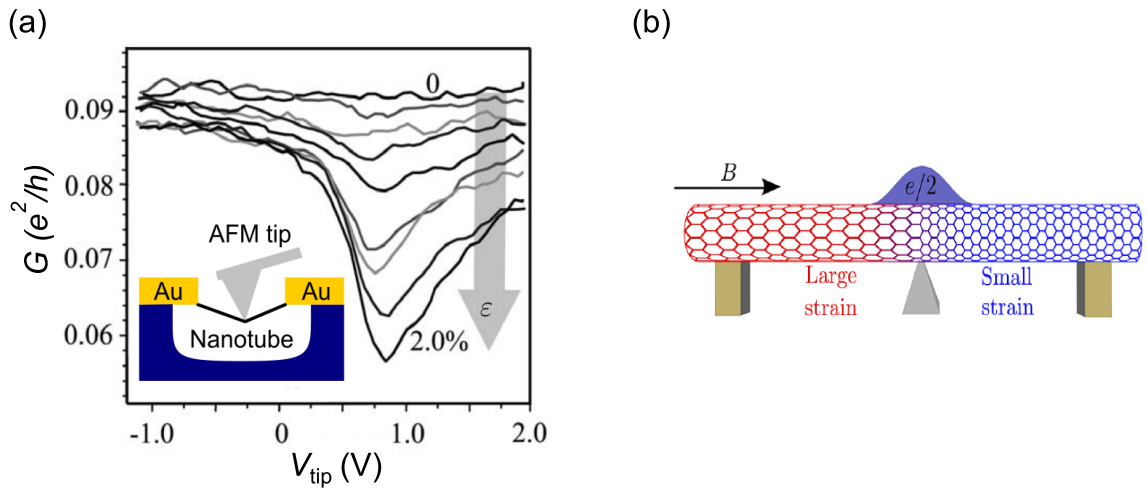

Figure 1.5: Recent results in CNT NEMS. (a) Local strain is applied on a suspended CNT device by increasing the tip voltage, leading to the conductance decrease. (b) Strains at the left and right sides of a CNT are different by placing a wedge-shaped pillar near the its middle. An axial magnetic field is applied to form a fractionalized charge in the middle region.

charge carriers were created at the strain interface. In another work, piezoresistive transport using strains $\lesssim 0.1$ % was studied by depositing SWCNTs on flexible sheets. These devices could be used as highly sensitive flexible strain sensors [35].

To understand quantitatively how strain affects transport behavior in SWCNTs, I must apply a uniform (disorder-free) strain to the whole SWCNT channel. However, AFM tips or substrate topography can only generate locally uniform mechanical strains. Moreover, it is not realistic to use either of these methods for extremely short SWCNT channels ($\sim$ 20 nm), where I aim to achieve large strains and explore quantum transport behavior. I will later present our custom experimental methods in chapter 2.

1.3 Organization of this Thesis

In this thesis, I present my two main results: first, the nanofabrication methods to create strain-tunable suspended SWCNT devices, and second, an applied theory to quantitatively describe quantum transport in strained SWCNT transistors. I led these two contributions, by fabricating the reported suspended SWCNT devices and extending a previously graphene-focused applied theory to adapt it in several ways to properly describe quantum transport in SWCNTs.

In chapter 2, I briefly introduce our QTSE experimental platform, which allows me to

apply a large, tunable, uniaxial mechanical strain on SWCNT transistors, inside a low-temperature cryostat. I then detail the nanofabrication steps to make strain-tunable suspended SWCNT transistors. Finally, I discuss the device preparation procedures that must be done right before making transport measurements: wire-bonding, and electromigration to create ultra-short SWCNT channels.

In chapter 3, I describe the effects of uniaxial strain on quantum transport behaviors in SWCNT devices theoretically. I first introduce the dominant strain effects on the Hamiltonian of SWCNT transistors, which can be described as scalar and vector potentials. I then explain how I calculate transmission probabilities, conductance, and capacitances in these transistors. Finally, I predict several strain transport signatures in different types of SWCNTs: valley polarization in metallic tubes, high on-off ratio quantum strain transistors in quasi-metallic ones, and vast electron-hole asymmetry in semiconducting ones.

In chapter 4, I summarize the main results presented in this thesis and discuss the outlook for future experiments.

Chapter 2

Fabrication of Strain-tunable Suspended SWCNT Transistors

Mechanical disorder or the lack of mechanical control in 1D or 2D carbon systems prevents the full exploration of quantum electronics, mechanics and optics. The first step could be to explore the strain effects in low-dimensional carbon systems. I aim to fabricate strain-tunable transistors which have potential applications in high frequency NEMS and quantum transistors. The experimental progress in this field has been slow due to the absence of an available platform to apply large, tunable and precise mechanical strain compatible with low temperature transport measurements.

Our group recently built such a platform, the first one to the best of our knowledge. This quantum transport strain engineering (QTSE) platform was built by our former group member Andrew McRae [36, 37]. So far, no one had made any strain-tunable suspended SWCNT devices compatible with this platform, and the fabrication of these devices is my main contribution to this chapter. In this chapter, I will first introduce our QTSE platform for studying quantum strain transport in low-dimensional materials. Then, I will detail the fabrication of strain-tunable SWCNT transistors. At the end, I will briefly discuss last fabrication steps which must be done inside a cryostat right before the data acquisition, which will be the focus of my PhD.

2.1 Introduction to the QTSE Platform

Our group built a custom instrumentation for quantum transport measurements in low-dimensional nano systems with large, tunable, and gate-independent mechanical strain. With our platform, I will apply uniaxial mechanical strain in SWCNT devices to study its effect on quantum transport in 1D systems. In this section, I will briefly present the design,

components, and capabilities of our QTSE platform. For more details about the design and construction of the instrumentation, see Ref. [20].

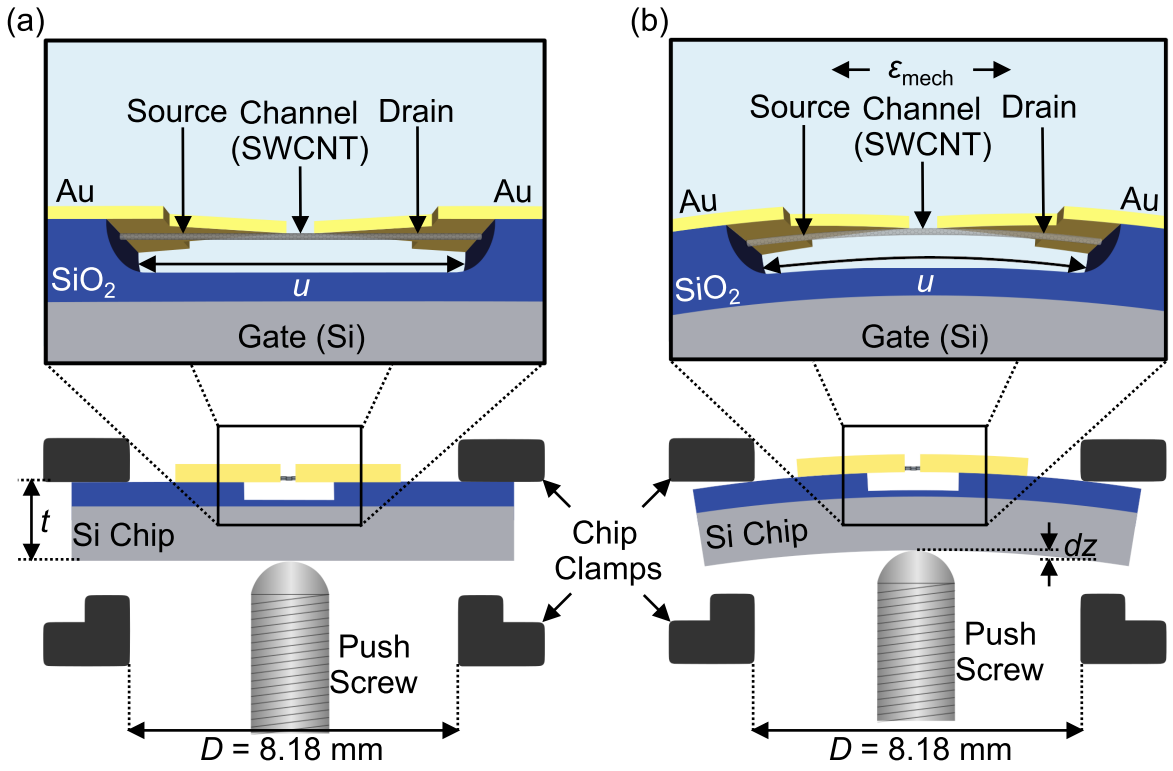

Figure 2.1: QTSE Platform. (a) Side view of the suspended SWCNT device and mechanical strain instrumentation. (b) Uniaxial mechanical strain $\varepsilon_{\text{mech}}$ is applied to the SWCNT channel by bending the thin Si chip. This assembly is located inside a 0.3 kelvin cryostat with a superconducting magnet (9T). Figure adapted from Ref. [20]

Figure 2.1 (a)-(b) show side view diagrams of the sample holder with an unstrained and strained SWCNT device respectively. Au contacts anchoring suspended SWCNT (as shown in insets) not only act as electrical leads to applying a bias voltage, but also as mechanical lever arms to amplify the uniaxial strain applied to the short naked SWCNT channel. Gate voltage is applied to the thin substrate (∼200 μm heavily doped Si) which is covered by SiO_2 (∼100 nm) to avoid the gate leakage short. A polished push screw bends the substrate which is held by the clamps creating the mechanical strain in the naked SWCNT channel. The theoretical in-plane stretching of the channel can be written as [38, 39]

$$dx = \frac{3ut}{D^2} dz. \tag{2.1}$$

where u is the suspended length of mechanical Au arms ($\approx 1\mu$m), t is the thickness of the substrate (200 μm), D is the distance between the clamps (8.18 mm), and dz is the vertical

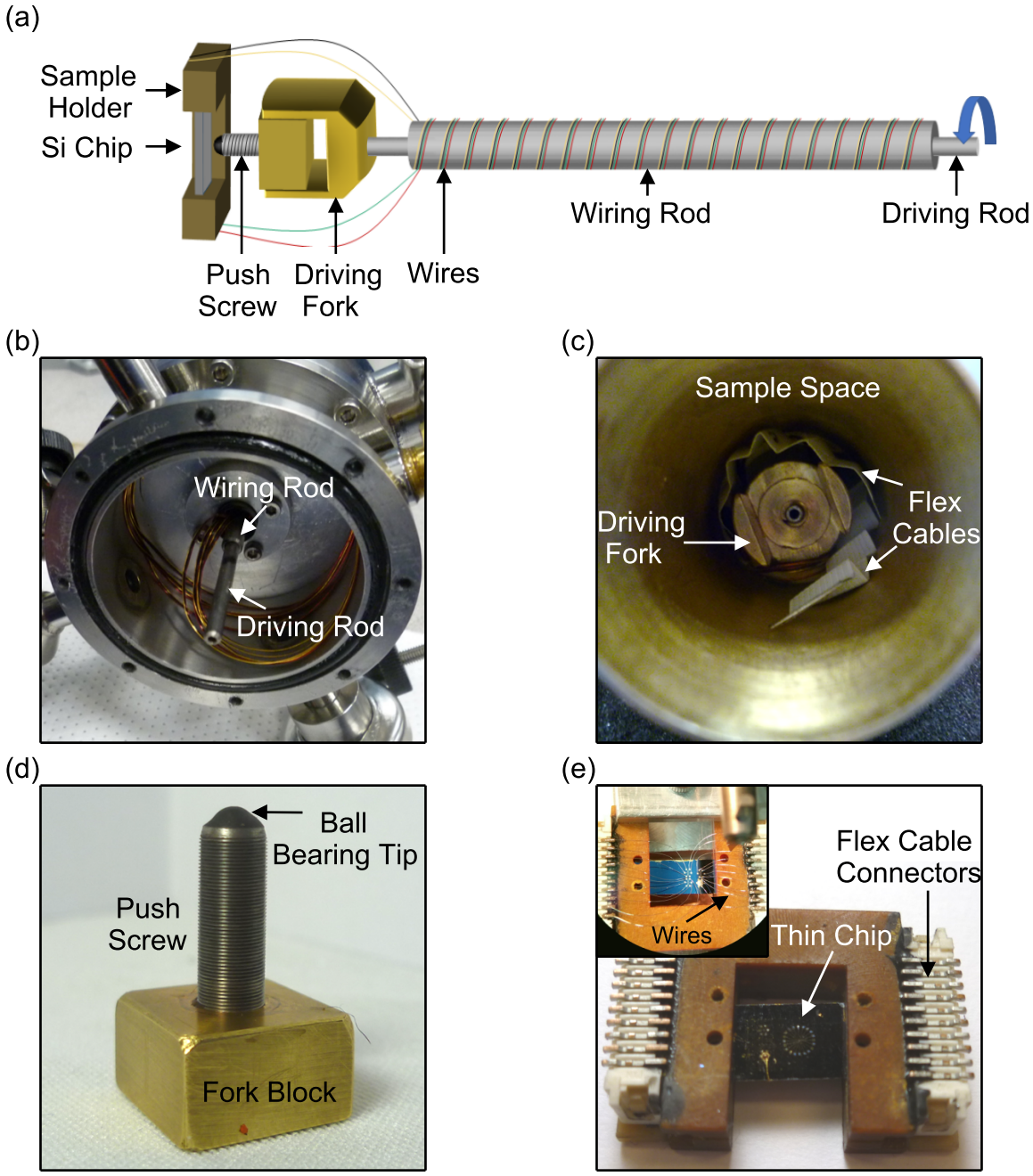

Figure 2.2: QTSE instrumentation. (a) The cryostat probe consists of two separate rods for mechanical and electrical control. Driving rod is rotated to turn the push screw which bends the Si thin chip that is held in the sample holder, while the wiring rod transmits electrical current for transport measurements at low temperature. (b) Image shows the driving rod passing through the wiring rod down to the bottom of the probe. (c) A driving fork is designed to apply torque to the push screw and the folded flex cables are used to connect electrically to the sample holder. (d) The push screw with ball bearing tip is epoxied into a fork block which is custom-built to fit the driving fork. (e) A thin chip is loaded into the sample holder with flex cable connectors for electrical connection. The inset shows a sample device bonded with aluminium wires to the connectors.

displacement of the push screw. From previous experiments [39], dz can reach up to ~ 300 μm causing a maximum lateral displacement ~ 2.7 nm. Our group has previously been able to create 20 nm naked SWCNT channels [40]. So the maximum theoretical uniaxial mechanical strain $\varepsilon_{\text{mech}}$ would be $\sim 13.5\%$. However, in previous work, we found that theoretical Eq. 2.1 leads to overestimated $\varepsilon_{\text{mech}}$, and I must avoid slippage of the SWCNT. Thus I aim to apply up to 5 % strain, which is much more than previous reported values ($\sim 1\%$) in strain-transport systems. Most importantly, the strain will be in-situ tunable, with high precision which was missing from previous low temperature work. Note that our QTSE platform could be modified to apply triaxial strains in 2D materials by changing the position of clamps [11].

We have already completed the QTSE platform. Figure 2.2 shows a few key pieces of the QTSE assembly. Panel (a) shows the cryostat probe design with separated driving and wiring rod for mechanical and electrical control respectively. With this probe, I can transmit mechanical rotation as well as electric current to push the screw which bends the substrate and perform electronic measurements at low temperature. Panel (b) is the view from the top of the probe showing the driving rod passing through the wiring rod down to the bottom of the probe. Panel (c) shows the driving fork at the bottom of the mechanical (driving) rod to apply torque to the push screw. The folded flex cables are used to electrically connect the sample holder. Panel (d) shows the stainless steel push screw with 100 threads-per-inch (TPI) (i.e. 254 μm advance for each full turn of screw). The ball bearing was coated with a polished Stycast insulating epoxy to avoid the electrical contact between the metal tip and the backside of the Si chip. Panel (e) shows the front view of the sample holder. It was designed to have a U shape so that the push screw can access the backside of the Si chip. The distance between two clamps D = 8.18 mm matters when converting the vertical displacement to lateral displacement as shown in Eq. 2.1. With flex cable connectors, I can apply electronic signals to sample devices on the chip after wire-bonding (shown in the inset).

We can calibrate the QTSE set-up with Au tunnel junctions. From our previous results, the tunnel electrical resistance R increases exponentially with the barrier thickness in a tunnel junction, as shown in Fig. 2.3 (a). The left and right insets show the Au tunnel junction changing thickness (electrode spacing). We measured the resistance of a Au tunnel junction at a fixed position (i.e. dz) over 15 hours. Figure 2.3 (b) shows the picometer stability of the tunnel junction over 15 hours demonstrating the absence of mechanical vibrations in the QTSE instrumentation.

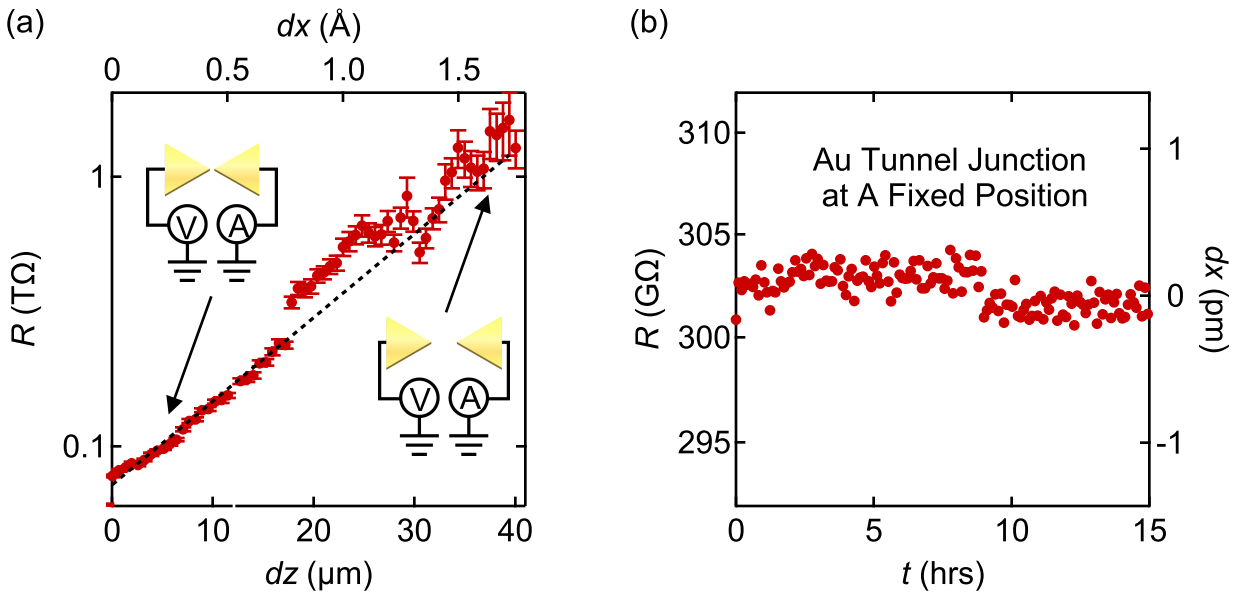

Figure 2.3: Calibration of QTSE instrumentation using gold tunnel junctions. (a) Resistance of the Au tunnel junction increases exponentially with the screw vertical displacement dz (bottom axis) and the break-junction lateral displacement dx (top axis). The black dashed line shows the exponential fit. (b) The tunnel junction shows pm stability over 15 hours. Figure adapted from Ref. [20].

We have constructed this instrumentation to apply large, tunable, and gate-independent uniaxial strain with an extremely good stability. This platform is ideal to explore quantum transport in 1D and 2D NEMS (e.g. SWCNT and graphene systems). Now fabricating suspended SWCNT devices compatible with the platform becomes the next major challenge.

2.2 Growing, Locating and Identifying SWCNTs

All CNTs are grown by our former group member Andrew McRae. Here, I briefly introduce this process. He starts the fabrication process with ultra-thin ($\sim$200 μm) double sided SiO_2-on-Si (doped) wafers, because they can be bent with the push screw. First, he remove the unwanted thermal SiO_2 from the backside of the wafers, so I can later make electrical contact to the Si wafer. He then uses reactive iron etching (RIE) to etch the backside oxide.

To grow CNTs, he first deposits a layer (6–8 Å) of Fe over a wafer with the grid pattern shown in Fig. 2.4 (a) using magneton sputtering. These L-shaped islands of Fe are heated (900°C) to form nanodroplets which will catalyze nanotube growth during chemical vapour deposition (CVD). By flowing the methane feedstock gas at 970°C, CNTs will be grown

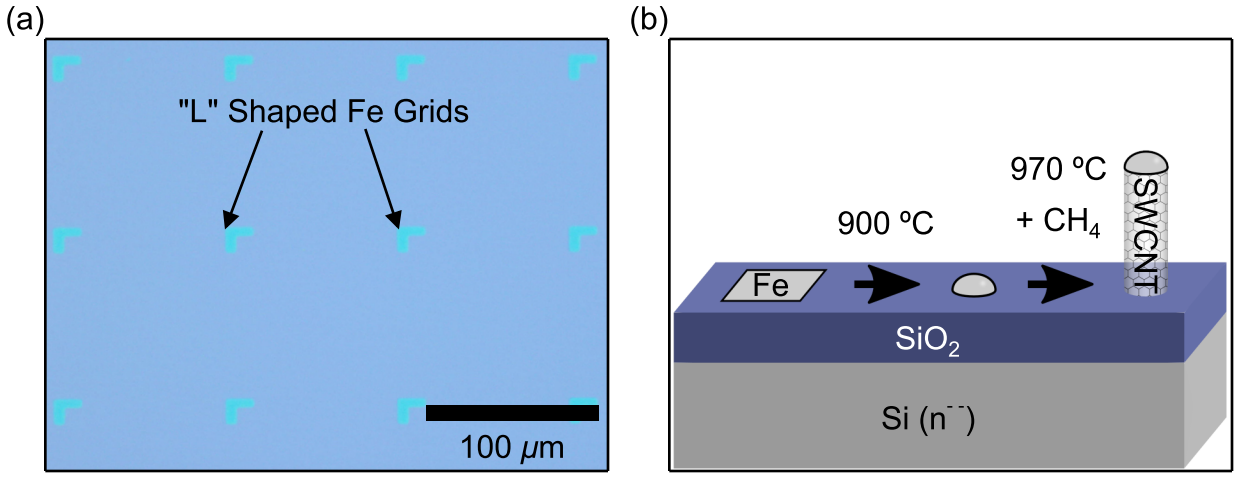

Figure 2.4: CVD growth of SWCNTs. (a) "L" shaped Fe islands are deposited on the Si wafer as a growth catalyst. (b) Fe islands form nanodroplets when heated at 900°C, and they catalyze the growth of SWCNTs when exposed to methane. Figure adapted from [20].

around those Fe nanoparticles. He then deposits gold grids with the same pattern on the wafer for alignment purpose. Detailed steps of the SWCNT growth are well described in Ref. [20]. I focus the rest of this section on fabrication steps where new developments are necessary to produce desired QTSE SWCNT devices.

It is important for the next steps to know the precise position of CNTs on the substrate to determine their diameter and to align Au electrodes on them. In this section, I show how to find CNTs using scanning electron microscopy (SEM) and how to select SWCNTs based on diameter measurements using atomic force microscopy (AFM). Note that all optical, AFM and SEM images were acquired by myself in the remained of this chapter except Fig. 2.13 in Sec. 2.5.

2.2.1 Finding CNTs - Scanning Electron Microscopy (SEM)

I image CNTs at low magnification with a SEM and record their positions based on Au markers deposited on the substrate (see Fig. 2.5). High-quality SEM images allow me to measure the accurate position and the precise shape of CNTs. During SEM imaging, a small amount of hydrocarbons are deposited on the imaged surface and cause contamination [41] which could contaminate CNTs. To minimize the carbon deposition per unit area during SEM imaging, I image at very low magnification (×620) and for short exposure times. Note that such low magnification and short exposure increase the challenge for precise

alignment of Au electrodes on top of CNTs during electron beam lithography (EBL), which will be discussed in the next section. Optimized SEM parameters are very important to find CNTs, especially SWCNTs at low magnification. I acquire images with the following parameters: accelerating voltage of 1.00 keV, current of 0.15 nA, and working distance of 6.0 mm. Figure 2.5 (a)-(b), (c)-(d) show SEM images of SWCNT and MWCNT respectively. I can see some L-shaped Au markers used for the alignment of lithography. In the zoom-in images (b), (d), I can clearly see the shape of the CNTs. From the experience, nanotubes with small ripples randomly walking along their length are very likely to be single-walled, due to their low structural rigidity [20]. Transport in single-wall carbon nanotubes is my main focus to understand quantum strain effects. To confirm that these candidate CNTs are single-wall, I will measure their diameters using AFM.

2.2.2 Selecting SWCNTs - Atomic Force Microscopy (AFM)

I image selected CNT candidates using AFM, and then select single-walled tubes based on their diameters. I use tapping mode AFM probes with the radii < 10 nm, resonant frequency ~ 300 Hz, and force constant ~ 40 N/m for my measurements. I first do a quick scan with dimensions of 10×10 μm to locate the desired CNT, and then I scan slowly across a small region (1×1 μm) crossed by the CNT to identify the locations where I will deposit the gold electrodes (break-junction). To obtain high-quality AFM images, I use a scan rate of 0.5 Hz (i.e. tip velocity of 1.0 μm/s) with 512 sample points per line. I am careful to optimize the AFM amplitude setpoint and feedback parameters to perform accurate measurements without damaging the nanotubes.

Figures 2.6 (a)-(b) show AFM images of the SWCNT and MWCNT shown in Fig. 2.5 (b) and (d) respectively. Note that the width of the nanotube in the images represent the width of the tip because it is much larger than the tube. I analyze multiple AFM line cuts across the tube to extract its height (diameter). To reduce the background noise from the SiO_2 surface roughness, I average the height curves from multiple line cuts and remove a linear background due to the tilt of the chip surface. By using this method to analyze the AFM data, the uncertainty of CNT diameters is decreased from $0.5 \sim 1.0$ nm to 0.2 nm comparing to the previous work in our group [20]. Figure 2.6 (c) and (d) show diameters of the SWCNT and MWCNT to be 1.4 ± 0.2 nm and 3.7 ± 0.2 nm respectively. Actual diameters can be slightly different because Van der Waals forces between the AFM tip and the CNT can modify the height measurements. I consider CNTs whose diameters are smaller than 2 nm to be single-walled based on the result from Ref. [42]. I now have thin bendable

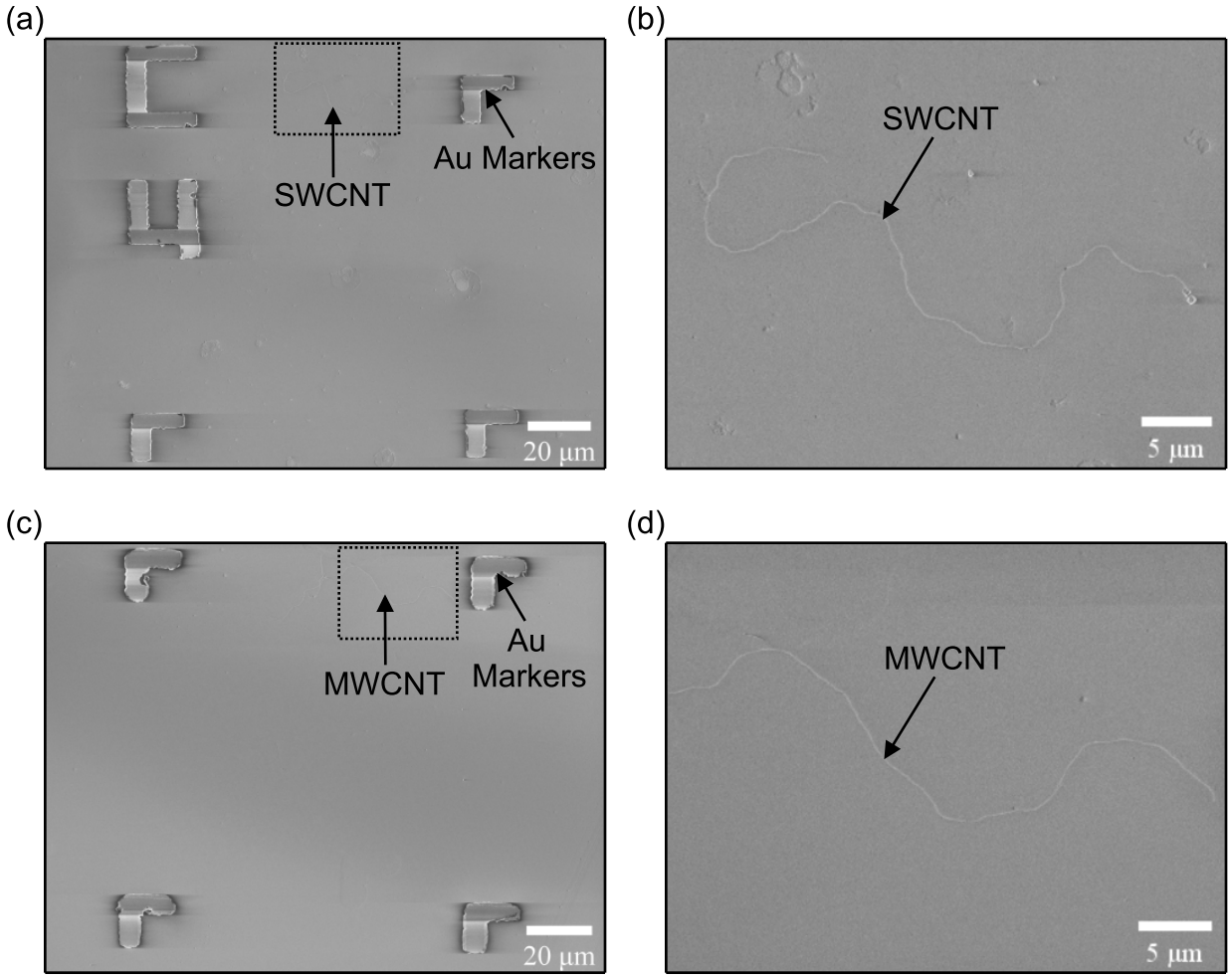

Figure 2.5: SEM images of candidate CNTs. (a) A SWCNT is located in the dashed rectangular area near Au markers. (b) Zoom-in of the dashed rectangular area shows clearly the shape of the SWCNT. (c)-(d) SEM images of a MWCNT

chips with precisely located SWCNTs.

2.3 Electrical Contacts to SWCNTs

Au electrodes play important roles in my suspended SWCNT devices. Micro-meter scale electrodes inject charge carriers in SWCNT sections acting as contact to the naked SWCNTs, also can apply bias voltage across the channel and mechanically clamp the tubes to avoid slippage. Moreover, the suspended gold contacts also act as lever arms to amplify the uniaxial strain from the bending motion of the Si chip (see Fig. 2.1 (b)). Because I cannot directly connect macroscopic wires to these micrometer metal electrodes, I also deposit 200 μm $\times$ 200

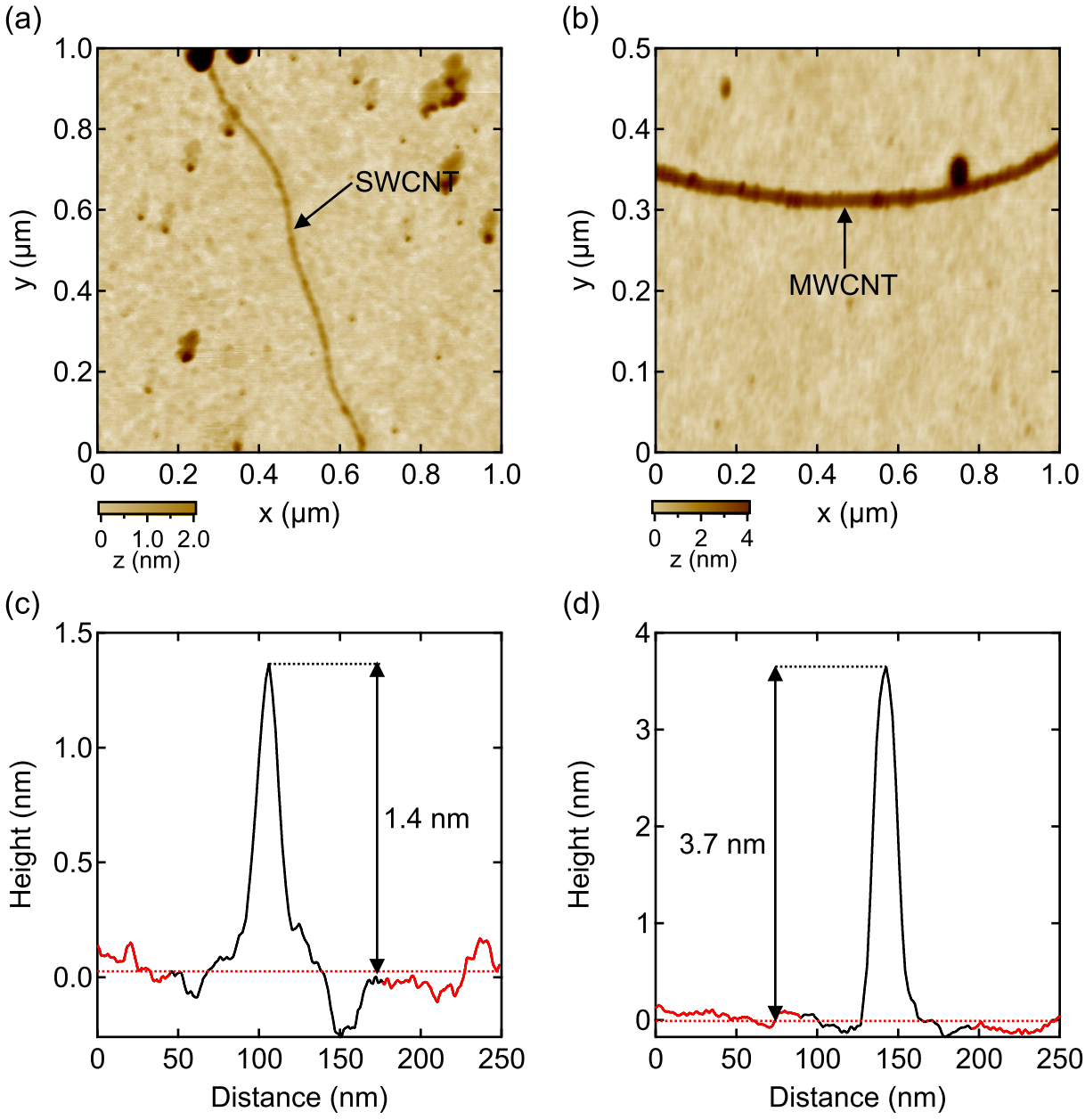

Figure 2.6: AFM images of CNTs. (a)-(b) AFM images of the SWCNT and MWCNT shown in Fig. 2.5 (b) and (d) respectively. (c)-(d) Average of six independent line cuts across the CNTs shown in (a) and (b), respectively. The red dashed lines show the average heights of the SiO_2 surface. The SWCNT has a diameter of 1.4 ± 0.2 nm, while the MWCNT has a diameter of 3.7 ± 0.2 nm.

μm Au pads for wire bonding. It is challenging to align the micrometer scale Au electrodes on top of the SWCNTs due to their few-nm diameters and the low magnification of the SEM images (to avoid contamination). In this section, I will explain how to deposit Au electrodes on SWCNTs using EBL, and then how to pattern large contact pads for wire bonding using photolithography.

2.3.1 Precise Alignment of Metal Depositions Using Electron Beam Lithography (EBL)

I use EBL to align micrometer scale circuits on SWCNTs and verify the alignment accuracy with SEM images. EBL uses a focused beam of electrons to draw custom patterns in electron-sensitive polymer films (e-beam resists) spun on a flat surface. The exposed polymer is then developed and a metal deposition followed by a solvent lift-off (remove unexposed resist) create Au electrodes on substrates.

The first step is to cover the chip surface with e-beam resists. I use a bilayer resist composed of 300 nm copolymer EL 9 (9% in Ethyl Lactate) followed by 200 nm PMMA A 4 (polymethyl methacrylate 4% in anisole). Such a double layer resist makes easier for a lift-off at the price of slightly decreasing the patterning resolution. To do so, I start by rinsing the chips with acetone and IPA to remove chemical residues, and dry them with N_2 gas. I then bake them at 120 °C for 10 mins to rid of any humidity. After cooling down the samples to the room temperature on the flat metal surface, I coat the chips with the copolymer EL 9 at the spinning rate of 3000 rotations per minute (rpm) for 1 minute, giving a 300 nm thickness and then bake them at 170 °C for 15 minutes. I follow the same fabrication steps with the same spin rate and time to coat PMMA A 4 with the thickness of 200 nm on top of EL 9.

While the above recipe works well in general, I find that very few chips covered with CNTs can be properly coated with either EL 9 or PMMA A 4. Figure 2.7 (a) shows an uneven resist coating on a CNT chip, where only small areas of the surface are coated. Figure 2.7 (b) shows a chip without CNTs where the whole surface is coated evenly. This is most likely because there are carbon residues over the whole chip surface after the CVD growth of CNTs. If I had plenty of chips with SWCNTs, I could play statistics and only use those chips that can be coated. However, I only have 4 chips with SWCNTs, and it is really time-consuming to grow CNTs, and locate SWCNTs. So I have to find another way to solve this e-beam resists coating problem.

From my experience, this adhesion issue cannot be solved by changing the spin coating parameters (e.g. spin rate, acceleration rate, spin time, baking temperature etc) or applying

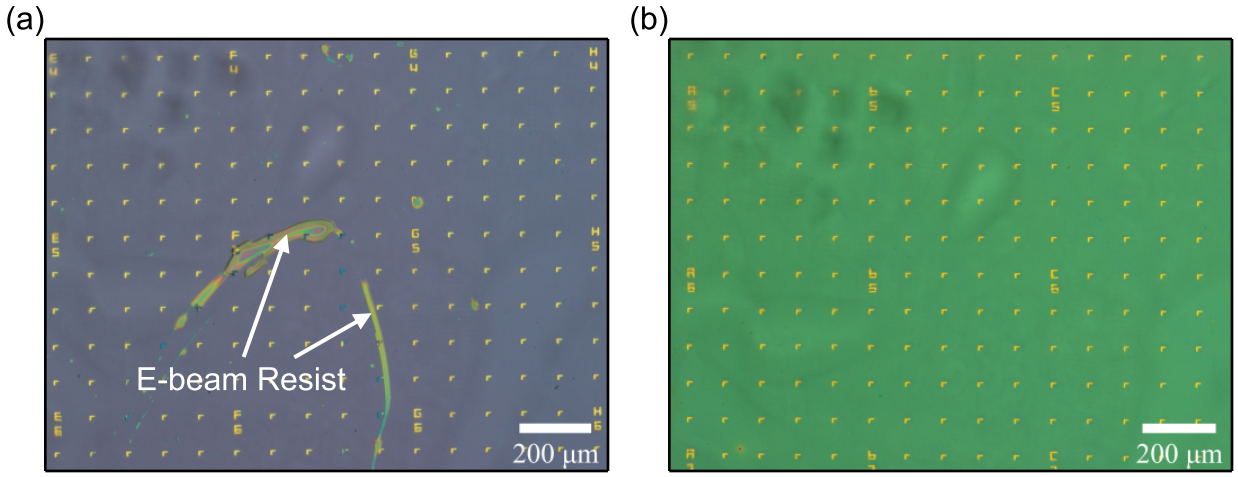

Figure 2.7: E-beam resist spinning. (a) For chips with coating problem, e-beam resist is unevenly coated on a small part of the chip surface. (b) For chips without coating problem, e-beam resist is evenly coated on the whole chip surface.

a layer of hexamethyldisilazane (HMDS) as an adhesion promoter. I thus resort to removing the problematic carbon residues without damaging CNTs. To do so, I use a mask made of a photoresist (AZ 5214) to protect those selected CNTs and then reactive iron etching to etch away the carbon residues on the chips. I cover the area of the SWCNT as shown in Fig. 2.8 (a). The chip surface is then etched with a reactive ion plasma, while SWCNTs are protected. During RIE, I use 20 SCCM O_2 at 200 mTorr with the power of 60 W for 10 seconds to avoid hard baking the photoresist for easier removal afterwards. Figure 2.8 (b) indicates that there is no resist residue on the chip surface after cleaning it with warm acetone optically. Even from the SEM images, I could not find any photoresist residue on the SWCNTs. The optical image in Fig. 2.8 (c) shows an uniform coating of e-beam resists on the SWCNT chip after being processed. Now all SWCNTs are ready to be exposed in the EBL system to define gold electrodes.

I load the resist-covered samples into the e-beam writer to expose the designed pattern. To achieve high resolution patterning, I use the acceleration voltage of 20 kV, working distance of 10 mm, aperture size of 20 μm, current of $\sim$ 0.13 nA, and a magnification of $\times$690, i.e. a 150 $\times$ 150 μm write-field. I carefully adjust the wobble and astigmation so that I can create a test exposures with diameters $\leq$ 20 nm. Note that the beam current should be measured right before the exposure.

I draw e-beam patterns with a computer aided design (CAD) software. I carefully align the rotation of the SEM image so that the reference L-grid is perfectly horizontal. With

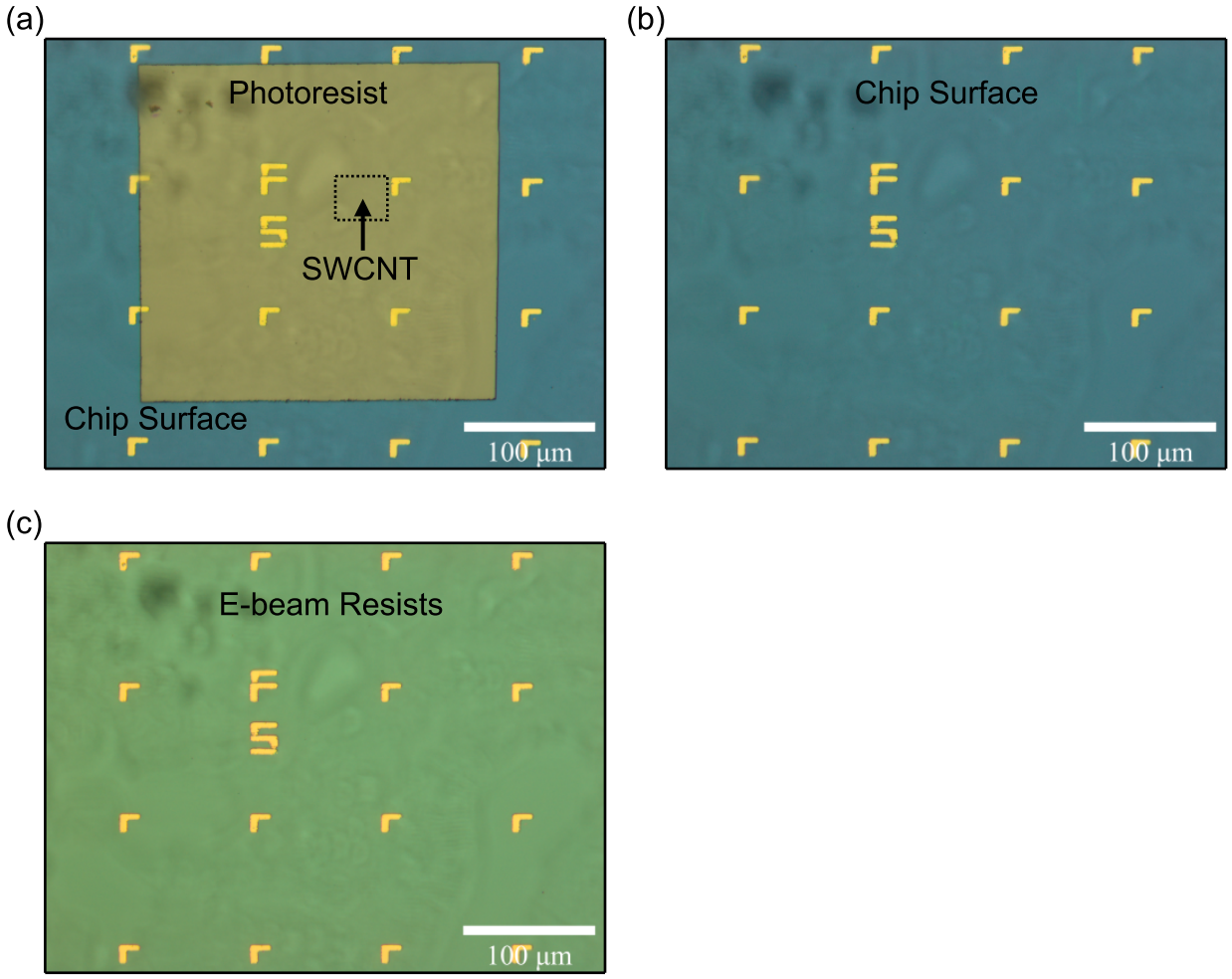

Figure 2.8: Solution to the e-beam resist adhesion issue on CNT-covered substrates. (a) A SWCNT located in the dashed rectangular area is covered by a photoresist mask. (b) I use RIE etching to remove carbon residue on the chip surface and then remove the photoresist mask with warm acetone. (c) E-beam resists can then be evenly coated on the chip surface.

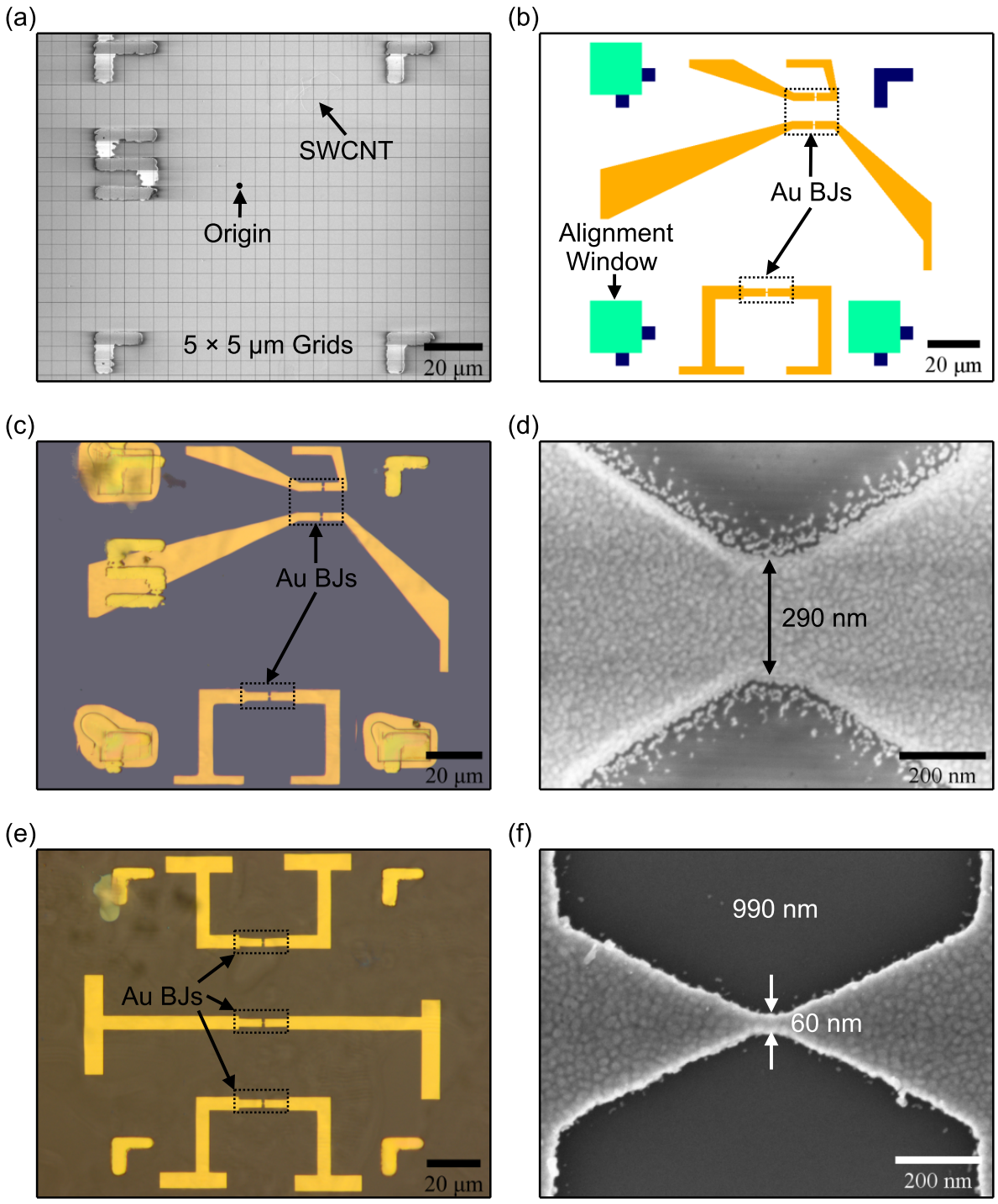

Figure 2.9: Lithography of electrical contacts on SWCNTs using EBL. (a) 5×5 μm mesh is drawn on a SEM image to create a coordinate system for CAD design. (b) E-beam patterns are designed to write Au BJs on top of SWCNTs. Square windows on 3 L-markers are used for alignment of the device with the CAD design. (c) Optical image showing Au electrodes pattern after metal deposition. (d) SEM image of the center of a break junction in (c) shows its width of 290 nm. (e) Optical image of three Au breakjunctions with widths of $\sim$ 60 nm used to create Au tunnel junctions. (f) Zoom-in on a device in (e).

the known distances between adjacent "L"s (100 μm), I create a CAD coordinate system to precisely locate the SWCNT with the help of a 5 $\mu m \times 5$ μm grid overlay as shown in Fig. 2.9 (a). I design breakjunctions which cover the horizontal (x-axis orientated) section of the SWCNTs, because the chips will be bent along the x-direction to create a uniaixal strain. Alignment windows shown in panel (b) are used for the manual alignment of the CAD designed "L-markers" on top of the physical L-markers on the chip.

After exposure, the exposed area are easily solved by a solution of 1:3 methyl isobutyl ketone:isopropyl alcohol (MIBK:IPA). I use the 1:3 proportion to achieve high resolution, but this requires being precise with the developing time. Samples are swirled slowly ($\sim$ 0.5 Hz) for 30 seconds in MIBK:IPA followed by 15 seconds in methanol to further develop the bottom e-beam resist EL 9 to create an undercut favoring metal lift-off later on. Finally, I rinse the chips in IPA for $\leq$ 1 minute to clean them and then blow them dry with N_2 gas.

After completing the development of the e-beam resist, I deposit a thin film of Au, 50 nm thick, using a thermal evaporator. The gold thickness is optimized to avoid the collapse of Au contacts after suspension, while being thin enough to permit controlled electromigration. I do not use any sticking layer under the Au to ensure pristine metal contacts to the SWCNTs. After evaporation, I lift off the undesired gold areas by placing the Si chips in warm acetone ($\sim 60\ ^{\circ}C$) for more than 40 minutes. Figure 2.9(c) shows an optical image after the liftoff.

To check the dimensions and shape of the Au electrodes, I acquire SEM images at very high magnification ($\times$70 k to $\times$100 k). I note that SWCNTs are now protected by the gold from any carbon contamination. Figure 2.9(d) shows a bowtie-shaped junction with its narrowest width of 290 nm. Particles around the edge will be removed during the suspension (SiO_2 etching).

As mentioned earlier, I will use gold tunnel junctions to calibrate our strain instrumentation. Figures 2.9 (e)-(f) show optical and SEM images of three Au tunnel junctions whose width is $\sim$ 60 nm, and suited for the electromigration of tunnel junctions. Note that for tunnel junctions I only use one layer of e-beam resist PMMA A 4 to achieve higher resolution.

To ensure that SWCNTs are correctly aligned under the Au junctions, I SEM image the devices with the same setting parameters used for finding CNTs in Section 2.2.2. The image in Fig. 2.9(a) is superimposed with the semitransparent SEM image of the SWCNT in Fig. 2.5(a). From this composite image, I can clearly see that the carbon nanotube goes through the Au junction. I have successfully deposited 9 out of 11 Au electrodes on top of SWCNTs leading to a yield $>$ 80 %. Most of these Au junctions have the width from 260 nm $\sim$ 400 nm while our previous reported SWCNT devices have the width from 390 nm $\sim$

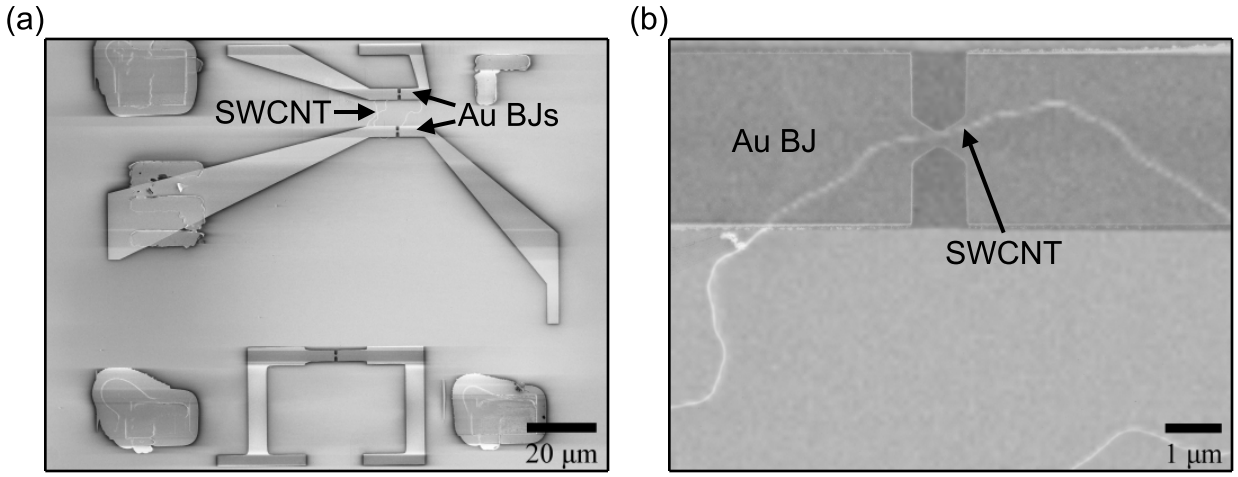

Figure 2.10: Alignment check of SWCNT break-junctions. (a) SEM image of Au break-junctions atop SWCNTs. (b) Semitransparent SEM image from Fig. 2.9(a) is superimposed at the image from (a) to check the alignment quality. It shows that the SWCNT goes through the junction.

480 nm [43]. The next step is to pattern large contact pads for wire-bonding.

2.3.2 Patterning Large Contact Pads - Photolithography

It would be very risky and not practical to contact the small EBL patterns directly with wires for the application of voltage and the transport measurements. To access the micrometer metal electrodes with macroscopic wires, I need to pattern 200 μm $\times$200 μm contact pads. Because they do not require high resolution or precise alignment, photolithography is the best suited method rather than EBL, as it is faster and more budget friendly.

I first clean the sample chip with acetone and IPA followed by N_2 drying. I then leave the chips on a hotplate at 120 °C for 10 minutes to get rid of any humidity. I place chips on the metal surface to thermalize them to room temperature rapidly. A one micron thick layer of photoresist OIR 674-11 is spin coated on the chips at a spin rate of 4000 rpm/s for 30 seconds, and acceleration rate of 456 rpm/s. A soft-bake is done at 90 °C for 1 minute. I align a photolithography mask pattern with six electrodes (see Fig. 2.11(a)) connecting to the small EBL pattern. Then I expose the resist for 4.1 seconds with a UV lamp power of 8.8 mW/cm^2 (i.e. a dose of 36 mJ/cm^2). I develop for 40 seconds using AZ726-MIF, amd rinse the chips with deionized water. The metal deposition consists of the thermal evaporation of 3 nm Cr as the sticking layer, and 100 nm of Au. Finally, I do the lift-off in warm acetone as previously. Because the six-point pattern is large and does not cover the SWCNTs, I use

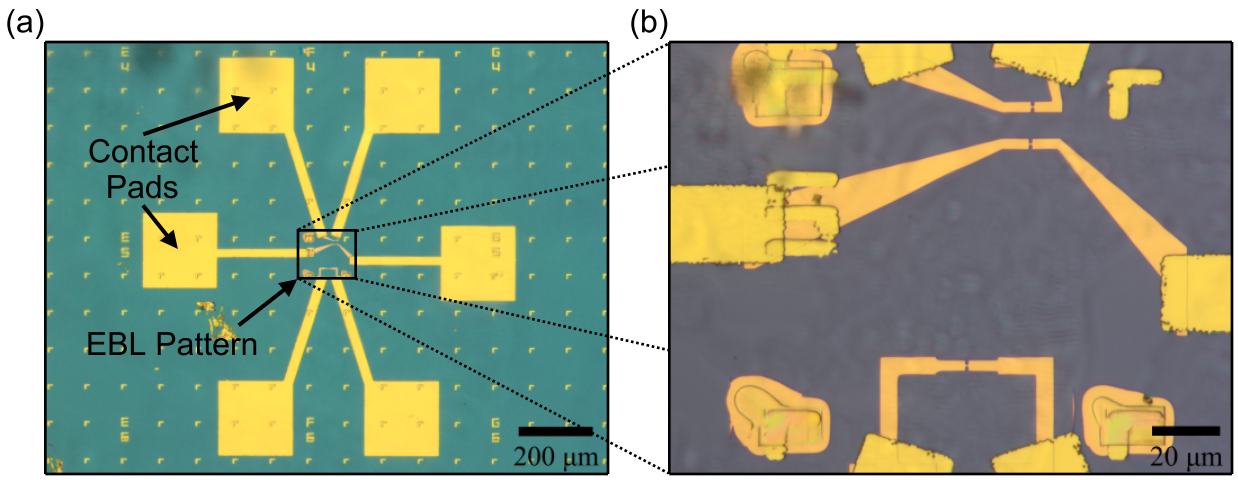

Figure 2.11: Depositing large pads to contact small EBL electrodes. (a) Optical image of six contact pads. (b) Zoom-in on the rectangular area in (a) shows that the large pads make good connections to the small electrodes.

Cr to ensure proper adhesion of the Au film.

Figure 2.11(a) shows six large contact pads for wire-bonding. Figure 2.11(b) is a zoom-in confirming that the small EBL pattern is well contacted by the six pads. Now I can move forward to the next fabrication stage: suspension of the break-junctions.

2.4 Suspending SWCNT Devices

To remove disorder and impurities from the substrate which could hinder quantum transport in the tubes, I suspend my devices by removing the supporting SiO_2. Another crucial reason is that suspended Au electrodes can act as cantilevers amplifying the uniaxial strain applied to the short naked SWCNT channel, which will be created after electromigration. To maximize the length of the cantilevers, I etch SiO_2 as much as possible using a wet buffer oxide etch (BOE), while avoiding the collapse of the Au electrodes. Tilted-SEM images of these suspended devices will be recorded to determine the suspension quality and dimensions.

Before I use a BOE to etch away the SiO_2 on the chips, I must remove sections of CNTs not covered by the Au electrodes to avoid gate leakage, and to remove any carbon or resist residues, which would act as a mask preventing the SiO_2 etch. An oxygen RIE is a good method to remove such residues. I place the chips in the RIE chamber and flow 20 SCCM of O_2, while remaining a pressure of 200 mTorr, and applying a plasma power of 200 W for 3 minutes. I then measure the SiO_2 thickness via reflectometry after RIE. Because water

would drastically affect the BOE etching speed, I bake chips on a hot plate at 120 °for 5 minutes.

I now place the chips in the BOE solution of 1:7 49% HF:NH_4F for 2 minutes and 30 seconds to etch $\sim$ 200 nm of SiO_2, i.e. a calibrated etch rate of 77 $\pm$ 2 nm/min. The chips are transferred into three successive deionized (DI) water for rinsing. I need to ensure that the chips are flat during the whole process to achieve an even etch and ensure that the break-junctions remain submerged in liquid (droplet on chips).

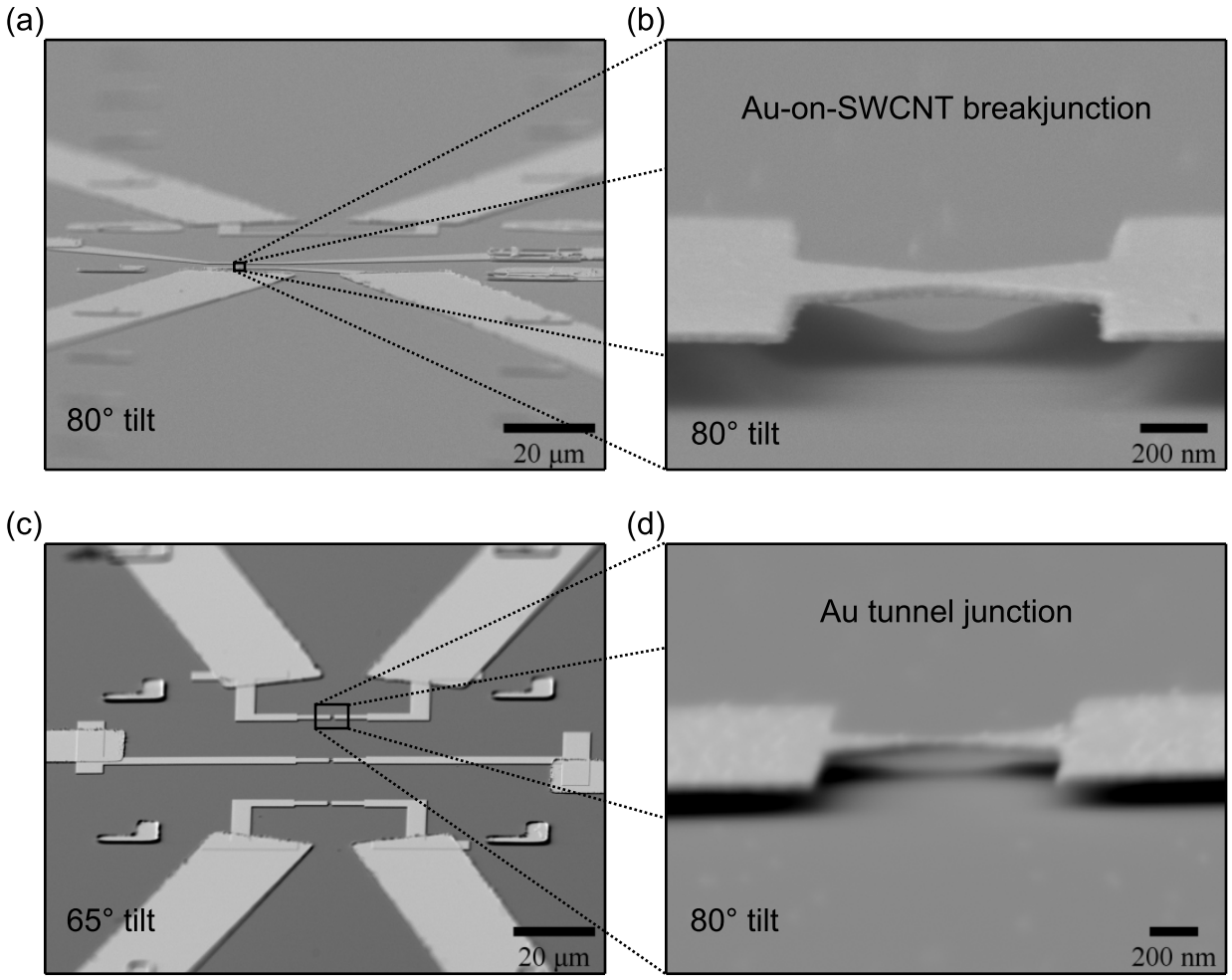

Figure 2.12: Suspended SWCNT breakjunctions and Au tunnel junctions. (a) Uniaxial strain causes a lateral shift of $G - V_G$ curves in a metallic SWCNT (11,11). (b) Tilted-SEM image (65°) of Au tunnel junctions from Fig. 2.9(e). (d) Zoom-in of one tunnel junction showing its suspension.

Because the strong liquid surface capillary forces during water evaporation would collapse the Au electrodes leading to the gate leakage and uncontrolled strain, I use a critical point

drying (CPD) procedure. I transfer chips from DI water to IPA, and then place them into an IPA-filled chamber for critical point drying. Again, chips should always be kept flat during the process. During critical point drying, liquid CO_2 displaces the IPA and enters the gaseous phase gradually without forming of a liquid-gas interface. The etched depth (suspension height) is then determined by measuring the remained SiO_2 thickness via reflectometry.

To determine the suspension quality and dimensions, I SEM image tilted devices at 80°. Figures 2.12 (a), (c) are tilted images of the suspended SWCNT break-junctions and Au tunnel junctions, respectively. In the zoom-in images (b), (d), I can clearly see that these junctions are completely suspended, and estimate the suspension length of the Au film for strain calculation (see Eq. 2.1). During my MSc, I have fabricated six high-quality suspended SWCNT devices on four thin Si chips, and they are ready for being wire-bonded, electromigrated and then measured.

2.5 Device Preparation for Low Temperature Strain Transport Measurements

After suspension, I will mount the Si chips on a sample holder with electrical contacts. I will then wire-bond the SWCNT devices to the sample holder pins, which will permit charge transport. Note that wire-bonding is very challenging for my devices, because these Si chips are only 200 μm thick, and they are moveable in this non-flat sample holder [20]. I will load the sample holder in our QTSE cryostat for the very final fabrication step: electromigration. Electromigration is a method used to create a nanogap in the bowtie-shaped junctions. The detailed electromigration procedure have been well described previously [43]. These steps must be done right before taking measurements. Since I plan to do the measurements in the future, these final fabrication steps are put off to my Ph.D. In this section, I give a brief introduction to the wire-bonding and electromigration process.

We first apply the conductive epoxy (EPO-TEK H20E) to both the front side and back side of thin chips, and contact them with Au wires for gating purpose. Thin chips are then carefully inserted into the middle of our U-shaped sample holder. Large contact pads are then connected to the grounded connectors with aluminum wires, which have a diameter of 25 μm (see Fig. 2.13 (a)). Tilted-SEM image ensures that wires are bonded firmly to those big pads without damaging the SiO_2, which could lead to a gate leakage short. Once the sample holder is loaded in our QTSE cryostat, we can start electromigrating the SWCNT devices

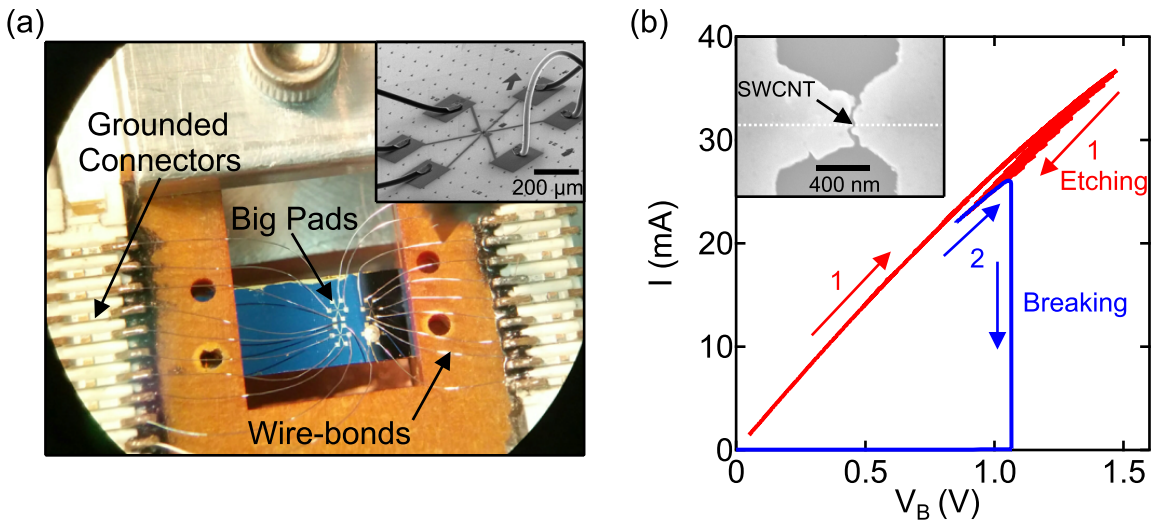

Figure 2.13: Wire bonding and Electromigration. (a) Macroscopic wires connect big pads and grounded connectors. Inset showing a tilted-SEM image of the wire bonds. (b) We narrow (red curve) and break (blue curve) Au junctions to create short naked SWCNT channels. Inset showing a SEM image of a device after electromigraion, which has a channel length of 14 ± 3 nm. Figure adapted from Ref. [20, 43, 44].

to create nanogaps in Au junctions. Figure 2.13(b) shows the collected electromigraion data for a SWCNT breakjunction at T = 4K. Feedback-mediated electromigraion narrows the junction with multiple feedback steps (red curve), and break it with a single feedback step (blue curve). Inset is the SEM image of a SWCNT device indicating a channel length of $\sim$ 14 nm. In this chapter, I mainly discuss our QTSE platform, fabrication process of suspended SWCNT transistors and the final preparation for transport measurements. In the next chapter, I will talk about how I developed an applied theory to guide my quantum strain transport measurements in these SWCNT devices.

Chapter 3

An Applied Theory for Quantum Transport in Strained SWCNTs

Although there are many proposals of quantum transport strain engineering (QTSE) in low-dimensional carbon systems [8, 10–14]. Progress has been very slow in realizing them experimentally, because there was no available QTSE platform suited for low temperature measurements and previous theoretical models too idealized to guide experiments [10,15–17].

With our custom-built QTSE platform, I can explore electronic transport behaviours in strained nanoscale graphene and SWCNT systems, see Fig. 3.1. Our group previously developed an applied theory for QTSE in graphene considering the dominant strain effects and realistic experimental parameters, and predicted graphene quantum strain transistors (GQSTs) [36]. In graphene, we minimized the impact from the crystal edge disorder by designing short and wide (aspect ratio ~ 10) channels. SWCNTs have zero edge defect due to their perfect periodic boundary conditions, and moreover would allow the study of 1D physics and quantum dot physics under strain, e.g. Kondo effect, excitons, polarons, NEMS. SWCNTs can be divided into 3 different types: metallic, quasi-metallic and semiconducting, based on their chirality (wrapping angle). Graphene, however, is always metallic, which prevents the confinement of electrons needed to enter the quantum dot regime.

I extended and modified the previous applied theory from graphene to describe SWCNT transistors. I modified the boundary conditions to calculate transmission probabilities of different modes, added quantum capacitances to consider the electronic structure of SWCNTs, and then systematically calculated strain-tunable transport signatures in SWCNT devices. In this chapter, I first introduce the dominant uniaxial strain effects on SWCNT Hamiltonian. By uniaxial, I mean that there is zero torsional strain. Then I derive the transmission probabilities and total capacitance in suspended SWCNT devices, to calculate conductance versus gate voltage or charge density. Finally, I show that the uniaxial strain can generate

valley polarization in metallic tubes, create outstanding quantum strain transistors in quasi-metallic tubes, and tune two vastly different behaviours for hole and electron charge carriers in semiconducting tubes.

3.1 Dominant Uniaxial Strain Effects on the SWCNT Hamiltonian

To calculate transmission probabilities across strained SWCNT channels, I first need to understand the impacts of the uniaxial strain on its Hamiltonian: the addition of a scalar potential and vector potentials. The first one arises from the change of next-nearest-neighbor (NNN) hopping energies under strain. This shifts the band structure downwards in energy [8, 24]. The latter one is induced by both the modulation of nearest-neighbor (NN) hopping energies and lattice constant [8, 16, 17], which results in displacements of the Dirac points in the first brillouin zone (FBZ) momentum space. We previously included similar strain-induced potentials in suspended graphene devices [36]. However, SWCNTs have discrete one-dimensional (1D) subbands, rather than two-dimensional (2D) bands, because of the periodic boundary condition along their circumferences. Moreover, the aspect ratio of SWCNT channels is much smaller than that of graphene channels, which dramatically decrease the number of available conducting modes. In this section, I explain how uniaxial strain changes the bandstructure in metallic (armchair) and semiconducting (chiral) SWCNTs.

3.1.1 Strain-induced scalar potential

When a uniaxial strain stretches short SWCNT channels, it modifies its charge carrier density (i.e. Fermi energy). I first describe the geometry of my fabricated and proposed SWCNT devices and then explain how a scalar potential can model the change in the low-energy bandstructure of SWCNT channels.

To enhance the electrical coupling between the SWCNT channel and back gate (Si substrate), I propose, in Fig. 3.1, realistic SWCNT devices with a 50-nm-thick suspension above the Si substrate. In my fabricated devices, so far, the vacuum is $\sim$ 200 nm and a layer of SiO_2 $\sim$ 100 nm covers a Si substrate. Other parameters such as the gold cantilever thickness, Si chip thickness, SWCNT channel length are identical in my theoretically proposed devices and the ones I have fabricated so far, see Chapter 2. Figure 3.1(a), (b) show a tilted cartoon of the proposed and fabricated SWCNT transistors. Gold cantilevers clamp the ultra short

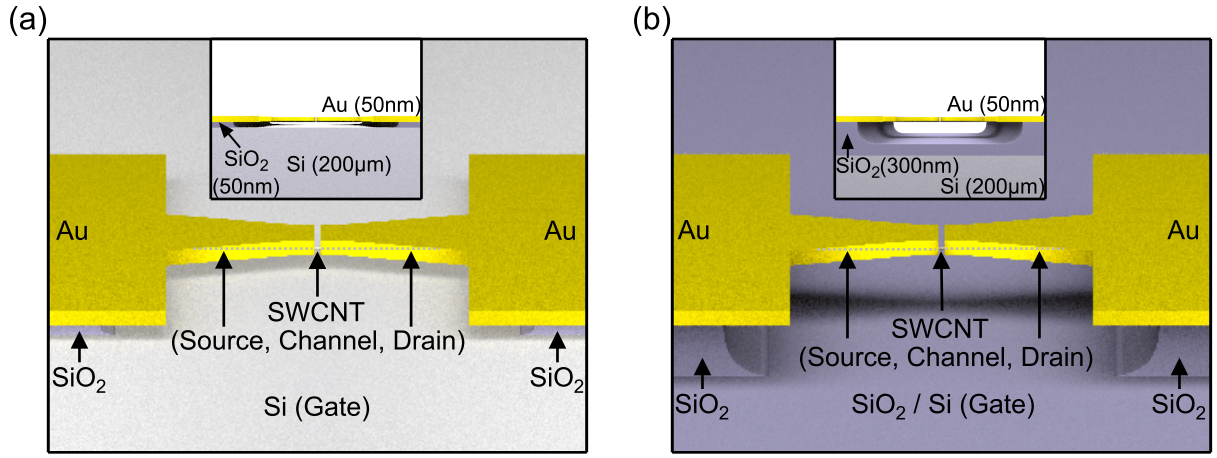

Figure 3.1: Geometry of proposed and fabricated SWCNT transistors. (a) Tilted-view of a proposed SWCNT transistor. The inset shows a side view. (b) Tilted-view of my fabricated SWCNT transistors. The inset shows a side view.

SWCNT channels (20 nm long), and are used to inject charge carriers into the nanotube sections, under the gold, acting as source/drain. The insets indicate the thickness of the different layers.

Equation 3.1 is the Hamiltonian in the K_i valley of a SWCNT under uniaxial strain, where the index $i = 1, 2, 3$ labels the three K valleys. Comparing to previously reported Hamiltonians [8, 15, 16, 45–47], it includes the relevant experimental parameters. To obtain the Hamiltonian in the K_i' valley, one can simply reverse the sign of the gauge vector potential A_i.

$$H_{K_i} = \hbar v_F \boldsymbol{\sigma} \cdot (\bar{\boldsymbol{I}} + (1-\beta)\bar{\boldsymbol{\varepsilon}})(\boldsymbol{k} - \boldsymbol{A}_i) + \Delta\mu_G + \Delta\mu_\varepsilon \tag{3.1}$$

where the Fermi velocity $v_F = (3/2)\gamma_0 a/\hbar \approx 8.8 \times 10^5$ m/s, with the unstrained hopping energy $\gamma_0 = -2.7$ eV [22], the nearest-neighbor spacing $a = 1.42$ Å, the electronic Grüneisen parameter $\beta \approx 2.5$ [8]. Pauli spin matrices form the pseudospin operator $\boldsymbol{\sigma} = (\sigma_x, \sigma_y)$, which acts on the two-component spinor wave function referring to two sublattices. $\boldsymbol{k} - \boldsymbol{A}_i$ is the generalized wavevector in the uniaxially strained channel. The matrices $\bar{\boldsymbol{I}}$ and $\bar{\boldsymbol{\varepsilon}}$ are the identity matrix and strain tensor respectively. Because I am interested in uniaxial strain, $\varepsilon_{xx} = \varepsilon_{\text{total}}$, $\varepsilon_{yy} = -\nu\varepsilon_{\text{total}}$ and $\varepsilon_{xy} = \varepsilon_{yx} = 0$, where $\nu = 0.165$ is the Poisson ratio [8,46]. The gate-induced electrostatic potential in the channel is represented by the term $\Delta\mu_{\text{G}}$, and in the source/drain SWCNT contacts, it is replaced by the doping energy $\Delta\mu_{\text{contact}}$ determined by the work function of gold. The last term $\Delta\mu_\varepsilon$ represents a scalar potential, in the channel only, and is strain dependent.

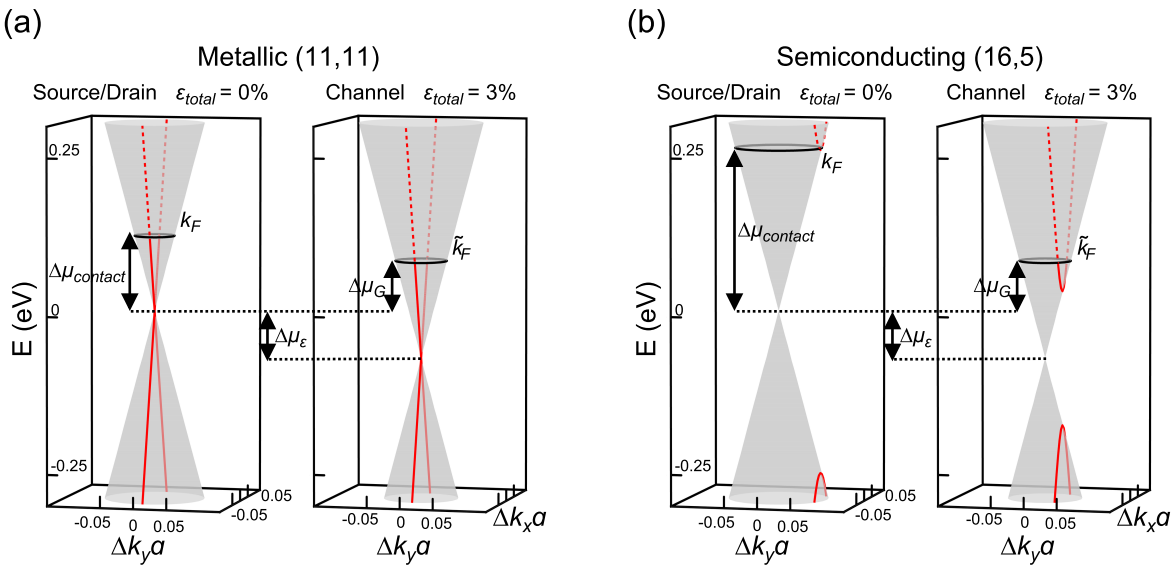

Figure 3.2: Tuning the band structure of SWCNTs via uniaxial strain. (a) $\Delta\mu_{\rm contact}$ determines k_F in the unstrained source/drain, while in the strained channel, $\tilde{k}_F$ is set by $\Delta\mu_\varepsilon$ and $\Delta\mu_{\rm G}$. One subband (red line) of a metallic SWCNT goes through the Dirac point showing a linear dispersion relation with/without the uniaixal strain, where the solid red line shows available electron states. (b) The uniaxial strain $\varepsilon_{\rm total}$ decreases the bandgap in a semiconducting SWCNT with the same diameter of the metallic one.

Figure 3.2 explains how the scalar potential can tune the band structure of SWCNTs. Red linecuts of the Dirac cone represent the allowed 1D subbands in SWCNTs. The Fermi level $\hbar k_F$ (black circle) in the unstrained SWCNT source/drain is determined by $\Delta\mu_{\rm contact}$, which depends on the work function difference between gold film and SWCNT. This doping energy can be tuned via Joule annealing of the gold [43]. $|\Delta\mu_{\rm contact}|$ can range from 0.05 to 0.25 eV [48, 49]. In metallic/quasi-metallic SWCNTs, I use the median value 0.12 eV, with hole doping [43], in calculations. In semiconducting SWCNTs, because the bandgap is ≈ 0.25 eV for a tube with a diameter of ≈ 1.5 nm (the average value of my SWCNTs), I use 0.26 eV to allow at least one energy subband available for transport in the source/drain. The strain-induced scalar potential $\Delta\mu_\varepsilon$ shifts downwards the low-energy dispersion relation, as shown in Fig. 3.2. It comes from the increase of the next-nearest-neighbour distances in the lattice structure, which then increases the workfunction of SWCNTs [45]. $\Delta\mu_\varepsilon = g_\varepsilon(1-\nu)\varepsilon_{\rm total}$ [50], where $g_\varepsilon \approx 3.0$ eV [51]. Figure 3.2(a) shows the band structure shift in a metallic SWCNT (11,11). The Fermi vector $\tilde{k}_F$ is set by $\Delta\mu_{\rm G}$ and $\Delta\mu_\varepsilon$. Solid parts of red lines represent occupied electron states, while dashed parts are not occupied. The subband passes through the Dirac point leading to a zero bandgap in metallic SWCNTs. Figure 3.2(b) shows the

decrease of a bandgap when applying a uniaxial strain to a semiconducting SWCNT with the same tube diameter. The lateral shift of the subband results from the gauge vector potentials, which will be discuss in the next subsection.

3.1.2 Strain-induced vector potentials

Uniaxial strain modifies the SWCNT lattice structure in real space leading to movements in reciprocal space. These lateral shifts are represented by vector potentials A_i, which can vary in different valleys. In this subsection, I explain how to obtain vector potentials and illustrate Dirac points shifts in different types of SWCNTs with the same diameter ($\approx$ 1.5 nm).

In uniaxially strained SWCNTs, the nearest-neighbour distances $\boldsymbol{\delta}_n$ are modified by a factor of $\bar{\boldsymbol{I}} + \bar{\boldsymbol{\varepsilon}}$, which then affects the Hamiltonian [16, 17]. These changes are represented by $\boldsymbol{A}_{\mathrm{lat},i} = -\bar{\boldsymbol{\varepsilon}} \cdot \boldsymbol{K_i}$. Another main modification of the Hamiltonian is via the change to the hopping energy between nearest-neighbour carbon atoms [8]: $\gamma_0 \to \gamma_0 \exp[-\beta((|(\bar{\boldsymbol{I}} + \bar{\boldsymbol{\varepsilon}}) \cdot \boldsymbol{\delta}_n|/a) - 1)]$, which can also be represented with a gauge vector potential $\boldsymbol{A}_{\mathrm{hop}} = (\beta/2a)(\varepsilon_{xx} - \varepsilon_{yy}, -2\varepsilon_{xy})$. I can obtain the total vector potentials by summing up these two terms $\boldsymbol{A}_i = \boldsymbol{A}_{\mathrm{lat},i} + \boldsymbol{A}_{\mathrm{hop}}$. To calculate them in the K_i' valleys, I can simply reverse the sign, as these two components are opposite in the K_i and K_i' valleys. I define the angle between the zigzag direction in SWCNTs and the x-axis (along the nanotube) as the crystal orientation $\theta = \frac{\pi}{2} - \theta_0$, where θ_0 is the chiral angle. I can then write the vector potentials in the K valleys [36]:

$$\boldsymbol{A}_{\mathrm{hop}} = \frac{\beta\varepsilon(1+\nu)}{2a} \begin{pmatrix} \cos 3\theta \\ \sin 3\theta \end{pmatrix} \tag{3.2a}$$

$$\boldsymbol{A}_{\mathrm{lat},1} = \frac{4\pi\varepsilon}{3\sqrt{3}a} \begin{pmatrix} -\cos\theta \\ \nu \sin\theta \end{pmatrix} \tag{3.2b}$$

$$\boldsymbol{A}_{\mathrm{lat},2} = \frac{2\pi\varepsilon}{3a} \begin{pmatrix} \frac{1}{\sqrt{3}}\cos\theta + \sin\theta \\ -\frac{1}{\sqrt{3}}\nu \sin\theta + \nu\cos\theta \end{pmatrix} \tag{3.2c}$$

$$\boldsymbol{A}_{\mathrm{lat},3} = \frac{2\pi\varepsilon}{3a} \begin{pmatrix} \frac{1}{\sqrt{3}}\cos\theta - \sin\theta \\ -\frac{1}{\sqrt{3}}\nu \sin\theta - \nu\cos\theta \end{pmatrix} \tag{3.2d}$$

These vector potentials represent the displacements from the original unstrained Dirac points to the strained ones. Figure 3.3 (a)-(b) show these displacements in an armchair SWCNT (11,11). Note that I exaggerate the uniaxial strain to 15 % for better visualization.

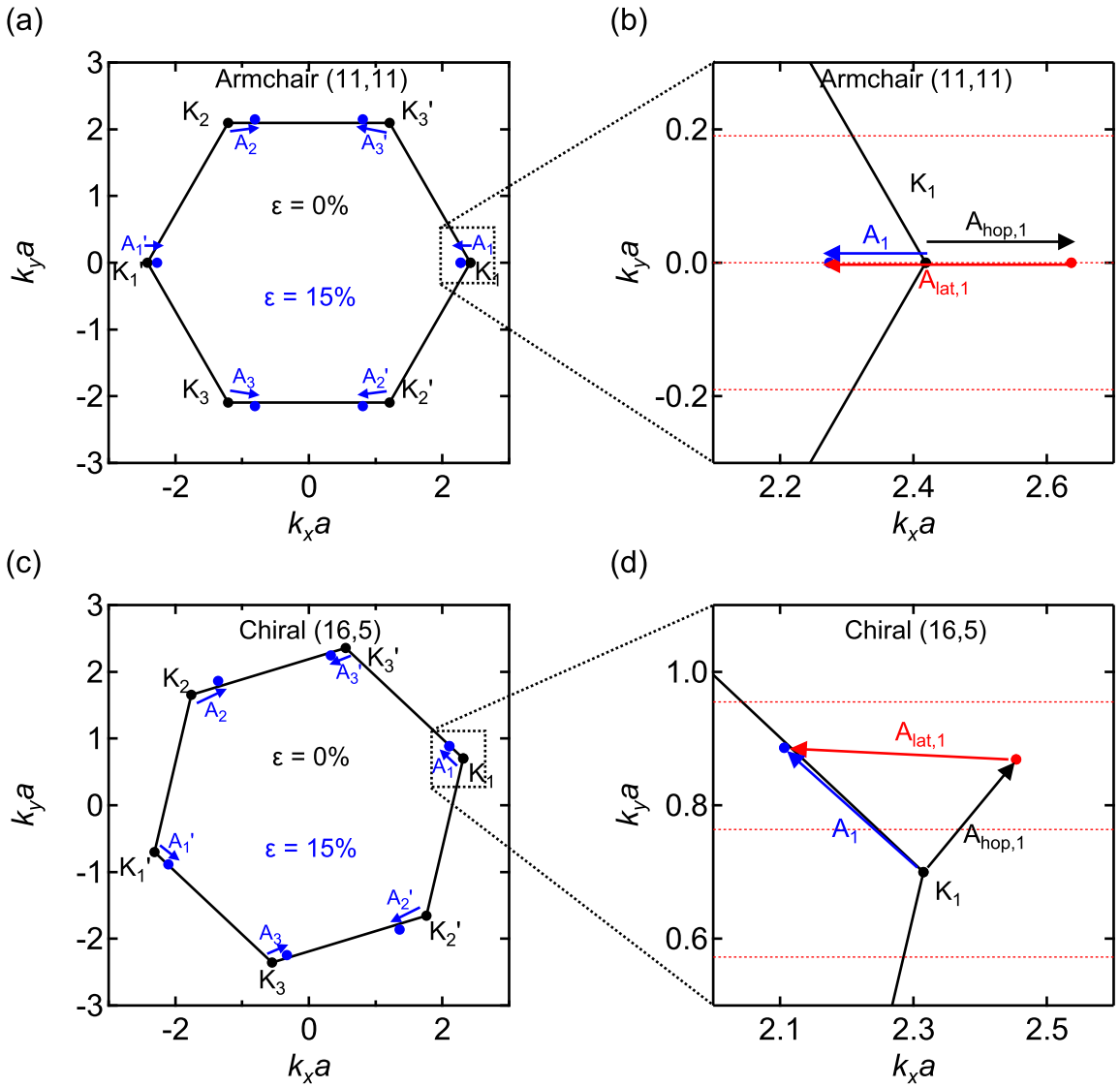

Figure 3.3: Shifting Dirac points via uniaxial strain. (a) Uniaxial strain shifts Dirac points in six valleys differently breaking the valley symmetry. $\varepsilon_{\text{total}}$ is exaggerated to 15 % for better visualization. (b) Zoom-in on K_1 valley shows that the vector potential $\boldsymbol{A}_i$ consists of the hopping part $\boldsymbol{A}_{\text{hop}}$ and the lattice part $\boldsymbol{A}_{\text{lat},i}$. Quantized momentum along circumference $k_y a$ (red dashed lines) passes the Dirac point in both unstrained and strained metallic SWCNT (11,11). (c)-(d) Dirac points shift in strained semiconducting SWCNT (16,5). Zoom-in on K_1 valley shows that the Dirac point crosses one quantized y momentum $k_y a$ (i.e. subband) leading to the increase followed by the decrease of the band gap.

In my experiments, I will only apply up to ≈ 5 % strain to SWCNT channels. Because $\boldsymbol{A}_{\mathrm{lat},1}$ does not have a y-component, i.e. Dirac points are shifted only along x-axis in momentum space, the subband (red dashed lines) still passes through the Dirac point, preserving a linear dispersion relation in the low-energy regime, as shown in Fig. 3.2(a). This is why nanotubes with armchair chirality are called metallic SWCNTs. A zoom-in on the K_1 valley (Fig. 3.3(b)) shows the hopping term $A_{\mathrm{hop},1}$ and the lattice term $A_{\mathrm{lat},1}$. In a chiral SWCNT (16,5), I get a different result (see Fig. 3.3(c)-(d)): with an increasing uniaxial strain, the Dirac points cross one subband leading to an increase followed by a decrease of its band gap.

The lattice term $A_{\mathrm{lat,i}}$ was often omitted in previous work, because it has a zero curl, i.e. zero pseudomagnetic field $\boldsymbol{B}_{\mathrm{sp}} = \nabla \times \boldsymbol{A}$ [11, 31]. However, when it comes to an Aharonov-Bohm-like experiment such as ours, this has to be considered, as it is comparable to the hopping term $A_{\mathrm{hop,i}}$ and significantly affects the Hamiltonian. Now that I understand these two dominant contributions from the uniaxial strain, I can move forward to build a transmission model for strained SWCNT transistors.

3.2 Transmission Model in Strained SWCNT Transistors

The SWCNT sections covered by gold are under no strain, and they act as source/drain contacts for the SWCNT channel. To obtain the conductance across the suspended SWCNT channel, I calculate the transmission probabilities of different modes at the strained/unstrained interfaces. Our group previously developed a transmission model for ballistic charge carriers in strained graphene [36], where the uniaxial strain alters the propagation angle of carriers and Klein transmission probability. The periodic boundary condition around a tube quantizes the corresponding transverse momentum, resulting in discrete subbands. The smaller the tube diameter is, the more discrete are those subbands. Thus, there are much fewer available modes in SWCNT source/drain than in graphene devices. In quasi-metallic and semiconducting SWCNTs, a uniaxial strain can open and modify energy band gaps, on the other hand, in graphene and metallic SWCNTs, the conduction and valence bands always touch at Dirac points. I modified the graphene transmission model to describe suspended SWCNT devices. I will detail how a uniaxial strain changes the transmission probability in the different valleys of SWCNTs with different chiralities.

To obtain the Klein transmission probability at the strained/unstrained SWCNT interfaces, where there is an electrostatic barrier due to $\Delta\mu_{\mathrm{contact}}$, $\Delta\mu_{\varepsilon}$, $\Delta\mu_{\mathrm{G}}$, I combine Eq. 3.1

and the boundary condition along the x-axis. I assume that the electrostatic potential and the strain field change abruptly at the interfaces (i.e. $\sim$ few nm wide barriers) [43, 52]. I solve for the transmission probability $T_{\xi,i,n}$ of each conduction mode (subband) n and valley $\xi = \pm 1$, $i = 1, 2, 3$:

$$T_{\xi,i,n} = \frac{(v_x k\tilde{k})^2}{(v_x k\tilde{k})^2 \cos^2[\tilde{k}L] + (k_F\tilde{k}_F - v_y q_n(q_n - \xi A_{i,y}))^2 \sin^2[\tilde{k}L]}, \tag{3.3}$$

where $k = (k_F^2 - k_{F,y}^2)^{1/2}$, $\tilde{k} = v_x^{-1}[v_F^2\tilde{k}_F^2 - v_y^2(k_{F,y} - \xi A_{i,y})^2]^{1/2}$, $v_x = v_{F,xx}/v_F = (1 + (1 - \beta)\varepsilon_{\text{total}})$, and $v_y = v_{F,yy}/v_F = (1 - (1 - \beta)\nu\varepsilon_{\text{total}})$. The SWCNT boundary conditions, $k_{F,y} = \frac{\pi}{W}(n + \alpha)$, define the quantized transversal momentum for the mode (subband) n, where α depends on the chirality of CNTs: $\alpha = 0$ for metallic/quasi-metallic ones, $\alpha = \frac{1}{3}$ for semiconducting ones [53]. By summing over all six Dirac cones of the FBZ and conduction modes, I find the charge conductance of SWCNT devices:

$$G = \frac{L}{W}\frac{2e^2}{h}\frac{1}{3}\sum_{\xi}\sum_{i}^{3}\sum_{n}^{N} T_{\xi,i,n}, \tag{3.4}$$

where $N = \text{Int}(k_F W/\pi - \alpha + 1)$ are the number of allowed modes, which is determined by the contact doping. The prefactor 1/3 in Eq. 3.4 accounts for the three-fold valley degeneracy in SWCNTs. In Eq. 3.2, 3.3, 3.4, I included the important experimentally relevant parameters $\Delta\mu_{\text{contact}}$, $\Delta\mu_{\varepsilon}$, θ, and $A_{\text{lat},i}$, which were not considered collectively in previous works [10, 15, 45].

I now discuss the strain-controlled transmission probabilities in SWCNT transistors. In Fig. 3.4(a), I show Fermi circles (k_{F} and $\tilde{k}_{\text{F}}$) in the source/drain and channel graphene sections. However, in a metallic SWCNT (11,11), only one subband (red solid line) has allowed electron states at energies below the Fermi level in the source/drain. Throughout the whole device, the boundary condition along the nanotube circumference remains the same, which leads to y-momentum conservation [10], i.e. $\tilde{k}_{F,y} = k_{F,y} - A_{i,y}$. The condition $|\tilde{k}_{F,y}| \leqslant \tilde{k}_F$ is drawn as dashed black lines in Fig. 3.4. The subband (red solid line) has to locate within these black dashed lines. I only consider the positive k_x states as electrons move from the source to the drain (from left to right) in my devices. From Eq. 3.3, the transmission probability (blue dashed line) $T = 1$, where the outer circle = 1, and origin = 0. Figure 3.4(b) shows that the Fermi circle in the channel is not shifted, because $A_{1,y} = 0$ in a strained metallic tube. This results in the same transmission probability $T = 1$ in the K_1 valley of a SWCNT (11,11) transistor. In an unstrained semiconducting SWCNT (16,5) transistor, see Fig. 3.4(c), the subband does not meet the y-momentum conservation

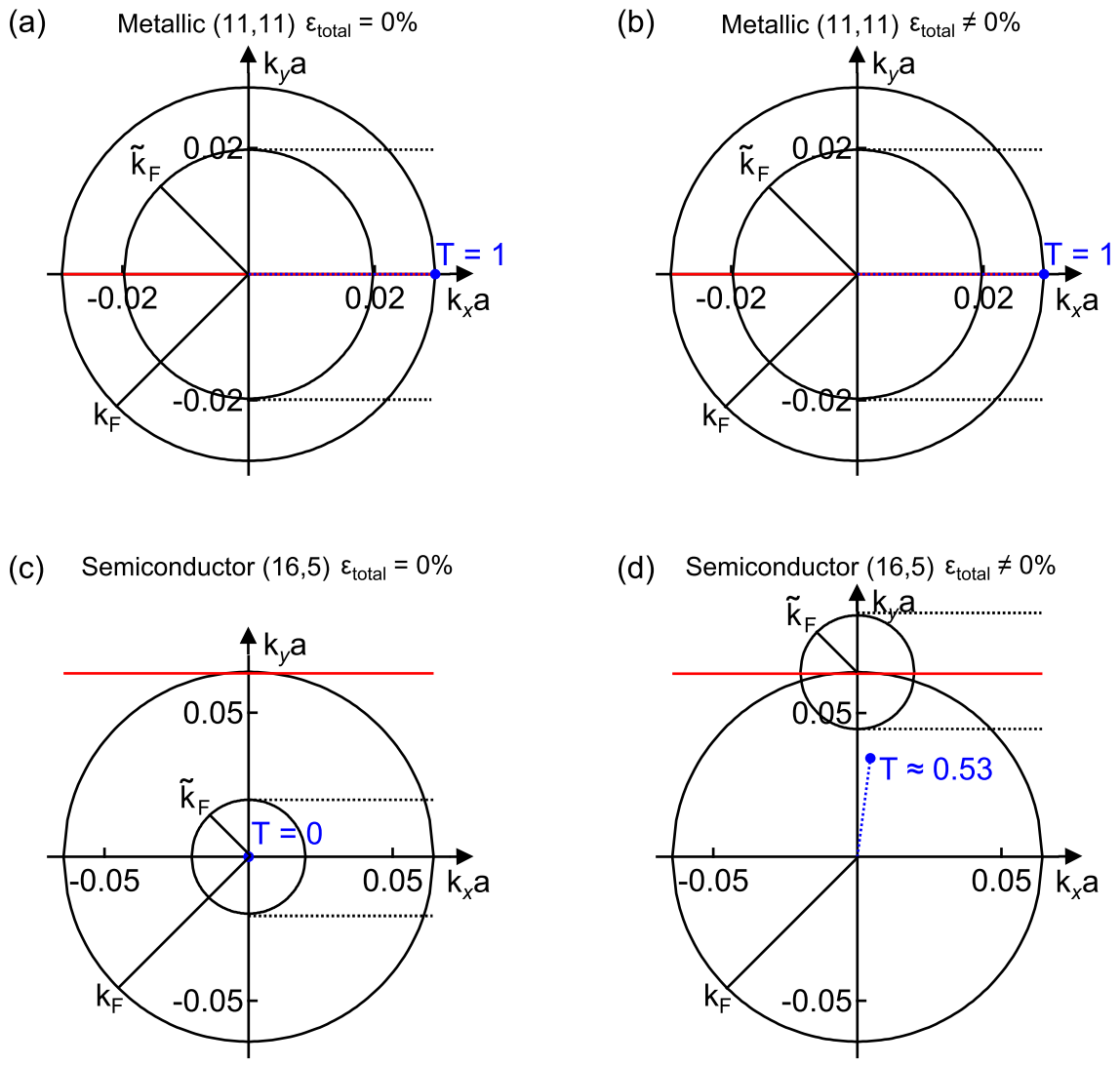

Figure 3.4: Matching energy and momentum between SWCNT contacts and SWCNT channel. (a) In the K_1 valley of a (11,11) SWCNT. Outer and inner circles are Fermi circles in the source/drain and channel (k_F and $\tilde{k}_F$). The subband (red solid line) meets the y-momentum conservation condition (black dashed lines) and has $T = 1$ (blue dashed line). (b) Fermi circle in the strained channel is not shifted and $T = 1$. (c)-(d) Fermi circles, y-momentum conservation conditions, transmission probabilities in a semiconducting (16,5) SWCNT transistor with $\varepsilon_{total} = 0$ and $\varepsilon_{total} \neq 0$, respectively.

condition leading to $T = 0$. When $A_{1,y} = k_{\mathrm{F}}$, the Fermi circle is shifted upwards to create available electron states in the channel. From Eq. 3.3, I find $T \approx 0.53$.

With this transmission model for strained SWCNT devices, I can study how the conductance depends on uniaxial strain. However, as the conductance (i.e. current) is experimentally measured as a function of the gate voltage, V_{G}, instead of the Fermi energy, I have to find the conversion factor between them.

3.3 Electronic Capacitances in SWCNT Devices

The electronic capacitance contains some of the ground state information of a SWCNT device [54], and can convert the Fermi energy to a gate voltage to guide experimental measurements. The total capacitance consists of a classical geometric capacitance (C_{g}) and a quantum capacitance (C_{q}) [55]. The geometric term only depends on the geometry of the suspended transistor. For graphene, it is a parallel plate capacitor geometry. For SWCNTs, it is a wire over a plane geometry. In our previous graphene model, we omitted the quantum capacitance because it affects the total capacitance negligibly. But in SWCNTs with bandgaps, it can modify the total capacitance significantly. To guide experimental transport measurements in strained SWCNTs, I calculated the geometric capacitance and added the quantum capacitance to our previous transmission model. In this section, I discuss how to obtain the classical geometric and quantum capacitance, and to determine gate voltage from Fermi energy in uniaxially strained SWCNT channels.

3.3.1 Classical Geometric Capacitance from Electrostatics

When capacitors are charged, electrons move around to minimize their electrostatic energy, leading to a geometric capacitance which is determined entirely by the device's geometry.

I use a wire over a plane model to find the geometric capacitance of my back-gated SWCNT devices [40, 43]:

$$\frac{C_G}{L_G} = \frac{2\pi\varepsilon}{\cosh^{-1}(\frac{t}{r})} \tag{3.5}$$

where $L_G = 20$ nm is the length of the SWCNT channel, $r \approx 0.75$ nm is the radius of the SWCNT, ε and t are the permittivity and thickness of the insulator respectively. There are two films forming the insulator in my fabricated devices: vacuum and SiO_2. In the proposed devices, there is only a film of 50 nm vacuum as the insulator. The geometric gate

capacitance can be obtained from:

$$\frac{C_{\mathrm{G}}}{L_{\mathrm{G}}} = \frac{2\pi\varepsilon_{\mathrm{ox}}}{\frac{\varepsilon_{\mathrm{ox}}}{\varepsilon_{\mathrm{vac}}}\cosh^{-1}(\frac{t_{\mathrm{vac}}}{r}) + \cosh^{-1}(\frac{t_{\mathrm{vac}}+t_{\mathrm{ox}}}{r+t_{\mathrm{vac}}})} \tag{3.6}$$

where $\varepsilon_{\mathrm{ox}}$, $\varepsilon_{\mathrm{vac}}$ are the permittivity, t_{ox}, t_{vac} are the thickness of the SiO_2 and vacuum respectively. From the Eq. 3.6, the geometric capacitances of SWCNTs with the same diameter are the same and do not change with Fermi energy, as shown in Fig. 3.5 (a)-(b) (black horizontal lines).

3.3.2 Quantum Capacitance from the Electronic Structure of SWCNTs

When it comes to the quantum regime, I have to consider the electronic structure of SWCNTs. Adding electrons requires finite kinetic energy, which leads to the quantum capacitance. It reduces the capacitance of the device ($C_{\mathrm{tot}} < C_{\mathrm{g}}$), because the geometric and quantum capacitances add in series [55]:

$$C_{\mathrm{tot}}^{-1} = C_{\mathrm{g}}^{-1} + C_{\mathrm{q}}^{-1} \tag{3.7}$$

where the quantum capacitance depends on the density of states in SWCNTs. It can be calculated as follows at a given Fermi energy, E_{F}, and temperature, T [55]:

$$C_{\mathrm{q}}(E_{\mathrm{F}}, T) = \int f'(\frac{E_{\mathrm{F}} - E'_{\mathrm{F}}}{k_{\mathrm{B}}T}) C_q^0 \sum_j (1 - (E_j/E'_{\mathrm{F}})^2)^{-1/2} \mathrm{d}E'_{\mathrm{F}} \tag{3.8}$$

where $k_{\mathrm{B}} = 1.38 \times 10^{-23}\,\mathrm{J}\cdot\mathrm{K}^{-1}$ is the Boltzmann constant, $E_j = \hbar v_{\mathrm{F}} * |(2/3d)(3j - (n - m)) - A_{i,y}|$ is half of the band gap of j subband in the K_i valley [55, 56], $d \approx 1.5$ nm is the SWCNT diameter, n, m are the chiral indices, $C_q^0 = 4e^2/(\pi\hbar v_{\mathrm{F}})$ is a constant value, f' is the derivative of the Fermi function. Because my interests lie in the low-energy regime, I only consider the first three subbands, i.e. subbands with the top three smallest bandgaps. Electrical currents are measured at very low temperature ($T \lesssim 1.3$ K), Equation 3.8 can then be simplified to:

$$C_{\mathrm{q}}(E_{\mathrm{F}}, T) = C_q^0 \sum_j (1 - (E_j/E_{\mathrm{F}})^2)^{-1/2} = e^2\, g(E_{\mathrm{F}}) \tag{3.9}$$

where $g(E_{\mathrm{F}}) = 4/(\pi\hbar v_{\mathrm{F}}) * \sum_j (1 - (E_j/E_{\mathrm{F}})^2)^{-1/2}$ is the density of states in SWCNTs [57]. Because of this density dependence, measurements of quantum capacitances can be used to probe the fundamental properties of the quantum ground state. I can convert the Fermi energy to a gate voltage using [55]:

$$\frac{\mathrm{d}E_{\mathrm{F}}}{\mathrm{d}(eV_{\mathrm{g}})} = \frac{C_{\mathrm{tot}}}{C_{\mathrm{q}}} \tag{3.10}$$

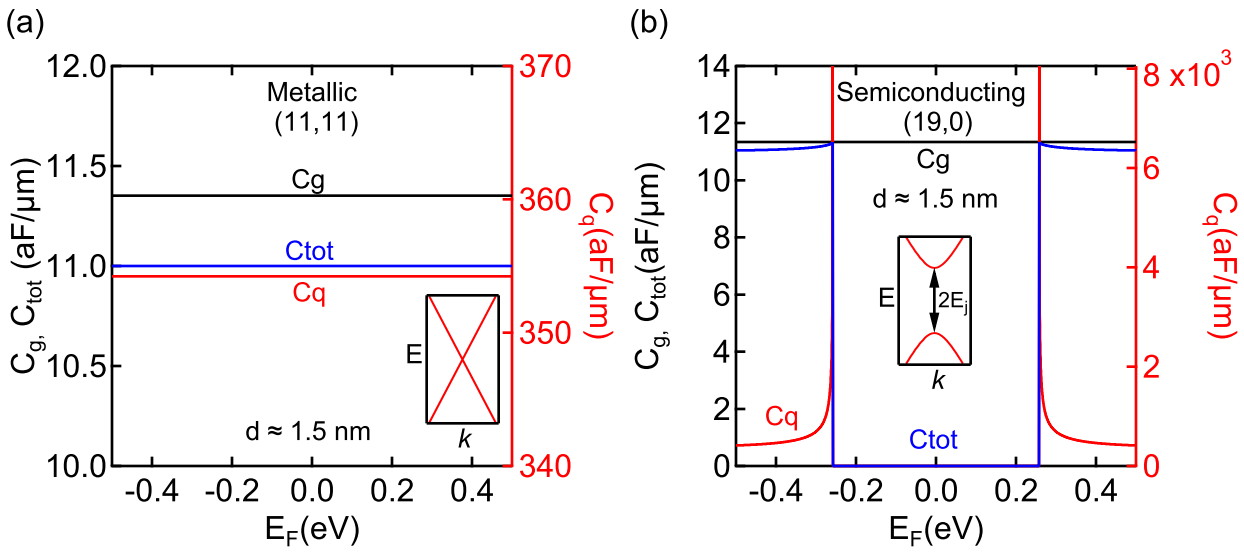

Figure 3.5: Capacitances in unstrained SWCNT devices. (a) Quantum capacitance (red) in an armchair metallic SWCNT (11,11), the geometric capacitance (black), and the total capacitance (blue). The inset shows the linear dispersion relation in metallic SWCNTs. (b) Quantum capacitance in a semiconducting SWCNT (19,0) sets the total capacitance to zero within the bandgap. The inset shows the parabolic dispersion relation in semiconducting SWCNTs.

Figure 3.5(a)-(b) show the capacitances in metallic and semiconducting SWCNT transistors, respectively. In the metallic tube, C_q is constant due to the constant density of states associated with a linear dispersion in 1D. C_q is about 30 times larger (right axis) than C_g. Thus, the total capacitance is only slightly shifted downwards with respect to C_g. In the semiconducting tube (19,0), shown in Fig. 3.5(b), C_q is zero within the bandgap, and shows 1D van Hove singularities at the band edges. This sets C_{tot} to zero within the bandgap, and decreases C_{tot} slightly outside the bandgap.

Figure 3.6 shows the capacitances in strained metallic and semiconducting SWCNT transistors and how they determine E_F to V_G conversion. In the metallic tube, uniaxial strain does not create a bandgap in the K_1 and K_1' valleys, but it does so in the other four valleys, as stated in the Subsection 3.1.2. Therefore, the total capacitance decreases to a non-zero constant value when a uniaxial strain is applied. With increasing strain, the bandgaps in the K_2, K_2', K_3, K_3' valleys become larger and lead to a wider minimum in C_{tot} in Fig. 3.6(a). In Fig. 3.6(c), the E_F vs $(V_G - V_D)$ relation changes slope around the Dirac point when $\varepsilon_{total} \neq 0$. This region becomes wider with larger uniaxial strain. In the semiconducting SWCNT (19,0), the bandgap first increases and then decreases with increasing uniaxial strain, as shown in

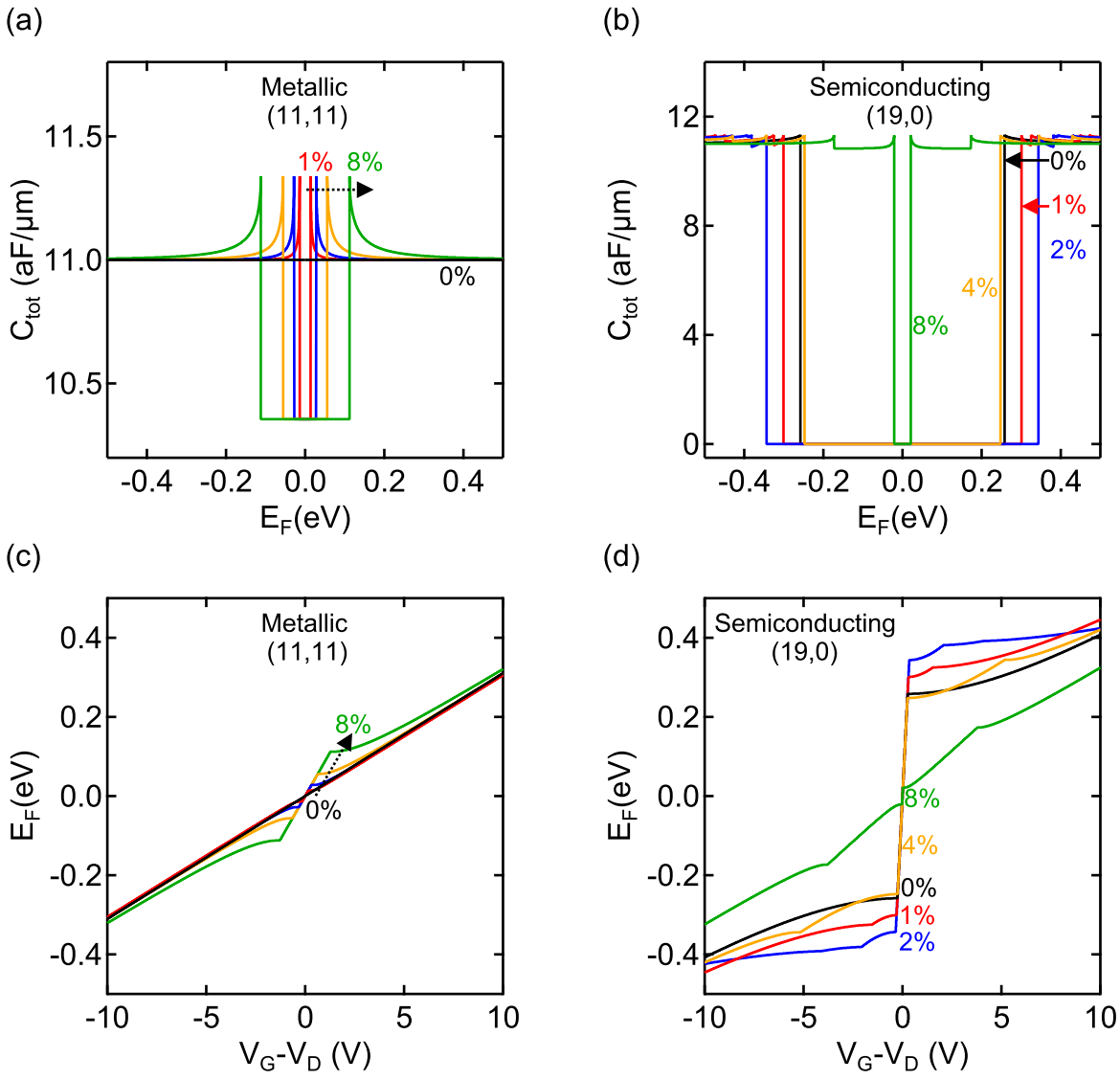

Figure 3.6: Capacitances in strained SWCNT devices. (a) In a metallic SWCNT (11,11), the total capacitance C_{tot} decreases to a constant non-zero value around the Dirac point due to the uniaxial strain. This non-zero region expands with the increasing strain. (b) In a semiconducting SWCNT (19,0), the total capacitance C_{tot} decreases to zero via the uniaxial strain indicating the creation of the bandgap. (c)-(d) From the calculated capacitances, one can obtain the dependence of Fermi energy on the gate voltage in different types of SWCNTs, which can be used to guide the experimental measurements.

Fig. 3.6(b). Within the bandgap, $C_{\text{tot}} = C_{\text{dos}} = 0$.

Now I am ready to calculate G from Eq. 3.4 considering the dominant contributions from the uniaxial strain in SWCNT channels and realistic experimentally parameters. By plotting G-V_{G} data, I study strain-tunable transport signatures in different types of SWCNTs in the next section.

3.4 Strain-tunable Transport Signatures in SWCNT Transistors

I map out the behaviour of conductance, from Eq. 3.4 in uniaxially strained SWCNT transistors, to explore the quantum transport in 1D NEMS as well as their potential technological applications. In this section, I first describe the gate position shift of the Dirac point arising from the strain-induced scalar potential and I then show how uniaxial strain in different types of SWCNT transistors leads to potential applications in valleytronics, strain sensors and logic circuits [58–61].

3.4.1 Strain-controlled Shift of the Dirac Point in $G - V_{\text{G}}$ Data

I recall that strain adds two types of potentials to the Hamiltonian: a scalar potential and vector potentials. In this subsection, I discuss the experimentally expected signature of the scalar potential in SWCNT transport.

Figure 3.7(a) shows $G - V_{\text{G}}$ curves in strained metallic tube (11,11), while excluding the scalar potential. I can clearly see a significant conductance suppression with increasing strain due to the vector potentials. I remark that this not the case in graphene devices with the same crystal orientation (zigzag direction) [36]. I will describe this effect in the next subsection, and for now focus on the influence of the scalar potential on conductance curves. Panel (b) shows the $G - V_{\text{G}}$ curves when the scalar potential is correctly included. The data are shifted left with increasing strain. The black arrows indicates the lateral shift of the V_{G} location of the Dirac point at 8% strain. By laterally shifting the curves in panel (a), I get exactly the same ones as in panel (b), proving that this lateral shift only results from $\Delta\mu_{\varepsilon}$.

In graphene, this Dirac point shift, V_{D}, depends quadratically on the total strain $\varepsilon_{\text{total}}$, and has nothing to do with the crystal orientation [36]. In SWCNTs, the chirality changes significantly V_{D}. In Figure 3.7(c)-(d), all tubes have similar diameters ≈ 1.5 nm. I see a linear relationship between V_{D} and $\varepsilon_{\text{total}}$ in metallic SWCNTs. With an increase in the chiral angle θ_0 (from zigzag to armchair), the $V_{\text{D}} - \varepsilon_{\text{total}}$ slope becomes steeper. For semiconducting

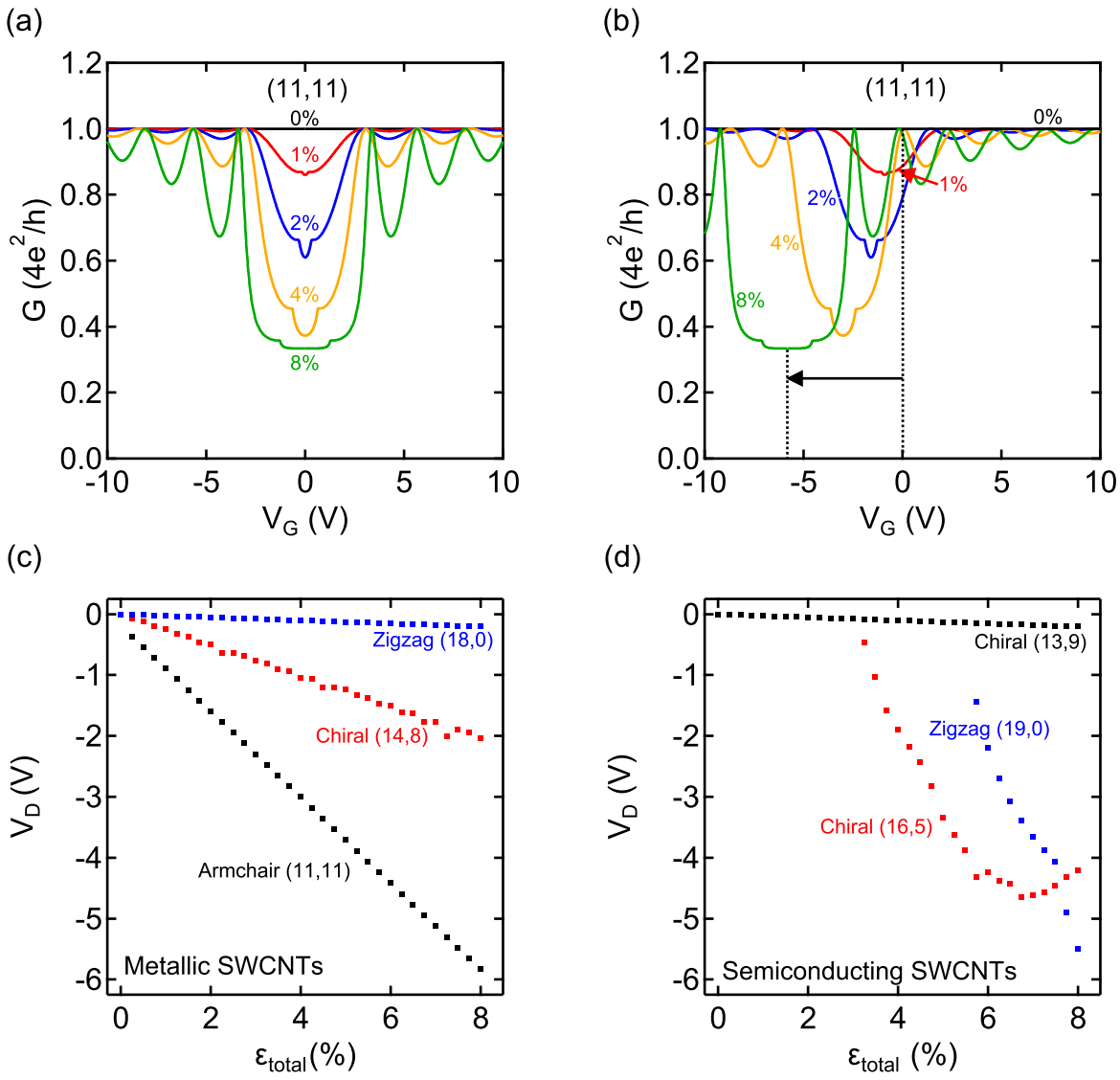

Figure 3.7: Strain-induced scalar potential shifts $G - V_G$ curves. (a)-(b) Uniaxial strain causes a lateral shift of $G - V_G$ curves in a metallic SWCNT (11,11). (c)-(d) In metallic and semiconducting SWCNTs, the dependence of the Dirac point shift on the uniaxial strain varies with chirality.

SWCNTs (see Fig. 3.7(d)), there is no simple dependence on the nanotube chirality. I obtain a similar curve for the chiral SWCNT (13,9) as that for the zigzag (18,0) in panel (c). The SWCNT bandstructure depends on chirality and it can be tuned with uniaxial strain. The same uniaxial strain produces different Dirac point shifts, because the quantum capacitance depends on the bandstructure.

3.4.2 Metallic SWCNTs: Strain-generated Valley Polarization

Metallic SWCNTs are those with armchair (n, n) chiral direction, see Fig. 1.3. Because of their special chirality, the uniaxial strain does not create bandgaps in the K_1 and K_1' valleys as stated in subsection 3.1.2. This allows me to generate valley-polarized currents, where current only flows in two valleys, encoding an additional quantum number (valley) in the current.

In Fig. 3.8-3.10, I plot G as a function of $V_{\mathrm{D}} - V_{\mathrm{G}}$ to remove the lateral shifts caused by strain-induced scalar potentials. Thus, all transport signatures obtained in Fig. 3.8-3.10 results from the strain-induced vector potentials. Figure 3.8(a) shows the conductance suppression from 1 to 1/3 of $4e^2/h$ versus $\varepsilon_{\mathrm{total}}$. To understand this non-zero constant value, I plot the conductance curves in K_1 & K_1', K_2 & K_2', K_3 & K_3' valleys in 3.8 (b), (c), (d) respectively. Because the subbands in the K_1 and K_1' valleys still go through the Dirac point under strain (see the inset of panel (b)), the linear dispersion relation at low energy remains the same. Transmission probability is thus always 1 leading to $G_{\mathrm{K}} = 1/3 * 4e^2/h$, as there is only one mode (subband) available. In K_2, K_3 and K_2', K_3' valleys, the uniaxial strain creates the bandgap as $A_{i,\mathrm{y}} \neq 0$, which leads to the zero conductance as shown in panels (c) and (d). By summing over all six valleys, I obtain the G vs $(V_{\mathrm{G}} - V_{\mathrm{D}})$ in Fig. 3.8(a). So, when $\varepsilon_{\mathrm{total}} = 8\,\%$ and $|V_{\mathrm{G}} - V_{\mathrm{D}}| \leqslant 1$ V, all charge carriers have the same valley quantum number, K_1, and are therefore valley-polarized. Because this transport result arises from the armchair chirality, this is true in all metallic SWCNTs. With uniaxial strain, I predict valley-polarized currents in metallic SWCNTs, with potential application in valleytronics [60], a sub-field of spintronics.

3.4.3 Quasi-metallic SWCNTs: Outstanding Quantum Strain Transistors

Unlike in truly metallic SWCNTs, strain can create energy bandgaps in quasi-metallic ($n - m = 3I$) SWCNTs, see Fig. 1.3. In this subsection, I discuss how the uniaxial strain tunes their conductance to zero, and discuss some figures of merit for these quantum strain

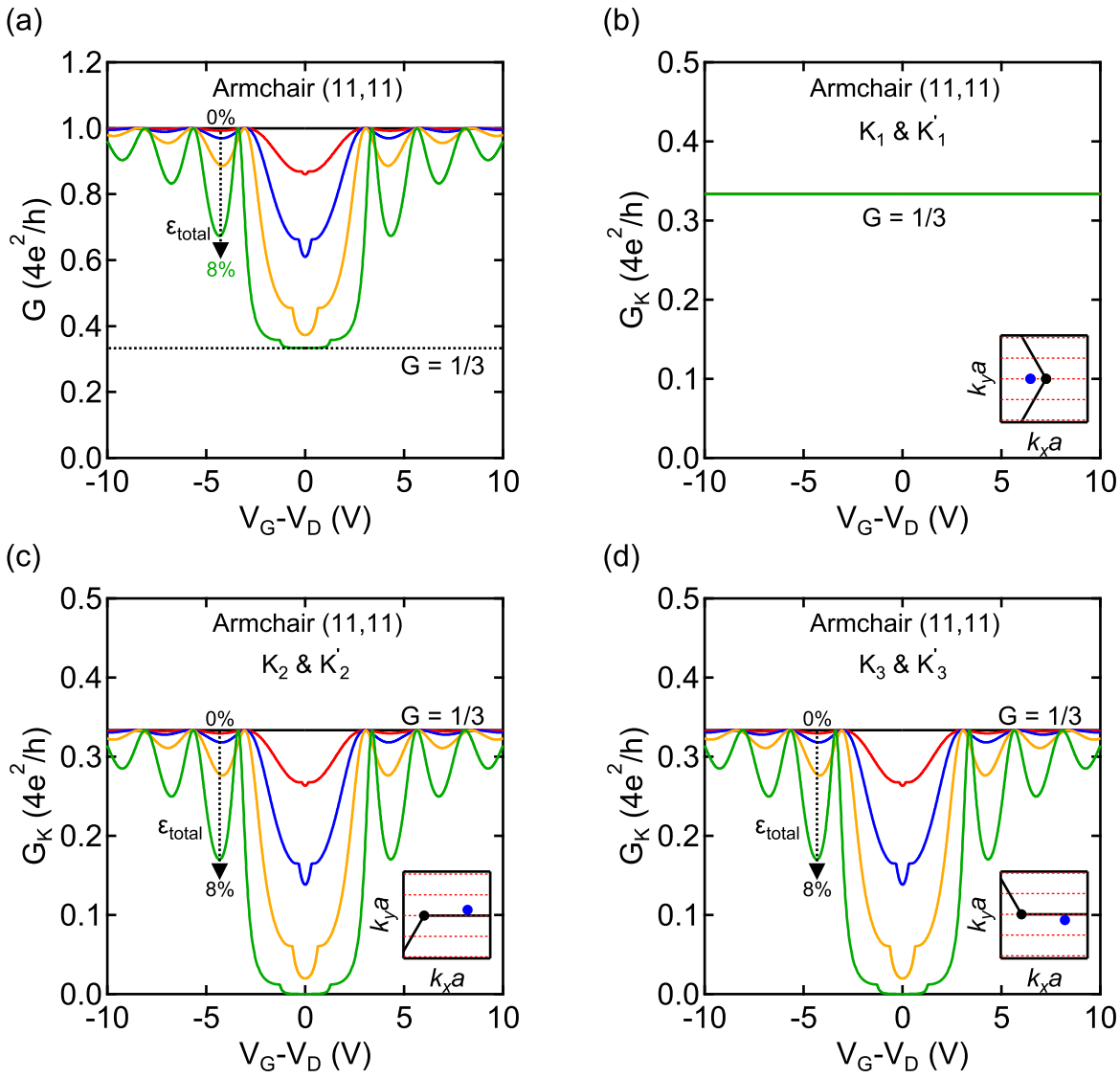

Figure 3.8: Tuning conductance via uniaxial strain in a metallic SWCNT (11,11). (a) G vs $(V_{\rm G} - V_{\rm D})$ in the FBZ at $\varepsilon_{\rm total} = 0\,\%$ (black), $1\,\%$ (red), $2\,\%$ (blue), $4\,\%$ (gold), $8\,\%$ (green). (b) G_K in the $\rm K_1$ and $\rm K_1'$ valleys at different strain. The inset shows a zero y-component of the vector potential. (c) G_K in the $\rm K_2$ and $\rm K_2'$ valleys at different strain. The inset shows a non-zero y-component of the vector potential. (d) G_K vs $(V_{\rm G} - V_{\rm D})$ in the $\rm K_3$ and $\rm K_3'$ valleys at different strain. The inset shows a non-zero y-component of the vector potential.

transistors.

Figures 3.9(a)-(b) show G - $(V_{\rm D} - V_{\rm G})$ curves in quasi-metallic SWCNTs with different chiralities. I can clearly see that with the increase of the uniaxial strain, the conductance is strongly suppressed in a zigzag SWCNT (18,0). This comes from both the generated bandgap and the modified propagation angle of charge carriers in the channel from the strain. The conductance suppression is obviously stronger in the zigzag tube than that in the (15,6) tube. Note that in graphene devices, I also found maximum conductance suppression when the zigzag direction is along x-axis. I plot the same G curves on a log scale (Fig. 3.9 (c)-(d)) to find the subthreshold slopes in these two SWCNT strain transistors under a total strain of 5 %. They both achieve a subthreshold slope of ≈ 30 mV/dec, which beats the thermionic (classical) limit 60 mV/dec. I can only access the linear subthreshold region with small $V_{\rm G}$'s change ($\lesssim 0.2$ V in panel (c) and $\lesssim 0.1$ V in (d)). The suppression due to the a change in the carrier propagation angle at higher $(V_{\rm D} - V_{\rm G})$, gives a slope of 270 mV/dec in the zigzag SWCNT, and was 240 mv/dec in a graphene device with the same crystal orientation [36].

3.4.4 Semiconducting SWCNTs: Vast Electron-hole Transport Asymmetry

It is possible to engineer a giant electron-hole transport asymmetry in semiconducting SWCNT transistors, because the contact-channel tunnel barriers are asymmetric when p-doping or n-doping the channel [43]. In this subsection, I demonstrate the tunability of this electron-hole device asymmetry using strain.

When $V_{\rm G} - V_{\rm D} > 0$, the SWCNT channel is n-doped and charge carriers are electrons. Otherwise, the SWCNT channel is p-doped and its charge carriers are holes. Figure 3.10(a) shows the conductance of an unstrained semiconducting SWCNT (19,0). Because the source and drain (SWCNT sections covered by gold electrodes) are p-doped in my model, i.e. $\Delta\mu_{\rm contact} < 0$, there is no tunnel barrier for the hole transport [43]. Thus, I observe ballistic transport signatures when $V_{\rm G} - V_{\rm D} < 0$. However, there is a barrier for electron transport, and I see quantum dot behaviours when $V_{\rm G} - V_{\rm D} > 0$. To illustrate this asymmetry more quantitatively, I define a relative electron-hole asymmetry as $\eta = 2(G_h - G_e)/(G_h + G_e)$. I extract the conductance G_h and G_e at $V_{\rm G} - V_{\rm D} = \pm$ 5 V as shown in Fig. 3.10(a). η has a maximum value of 2 when $G_{\rm e} = 0$, and a minimum value of -2 when $G_{\rm h} = 0$. The transport of electrons and holes becomes symmetric when $\eta = 0$. When I apply a 4% strain, see Fig. 3.10(b), I switch the electron transport from quantum dot (QD) to ballistic (Fabry-Perot cavity). The asymmetry depends on the chirality of the SWCNT. I

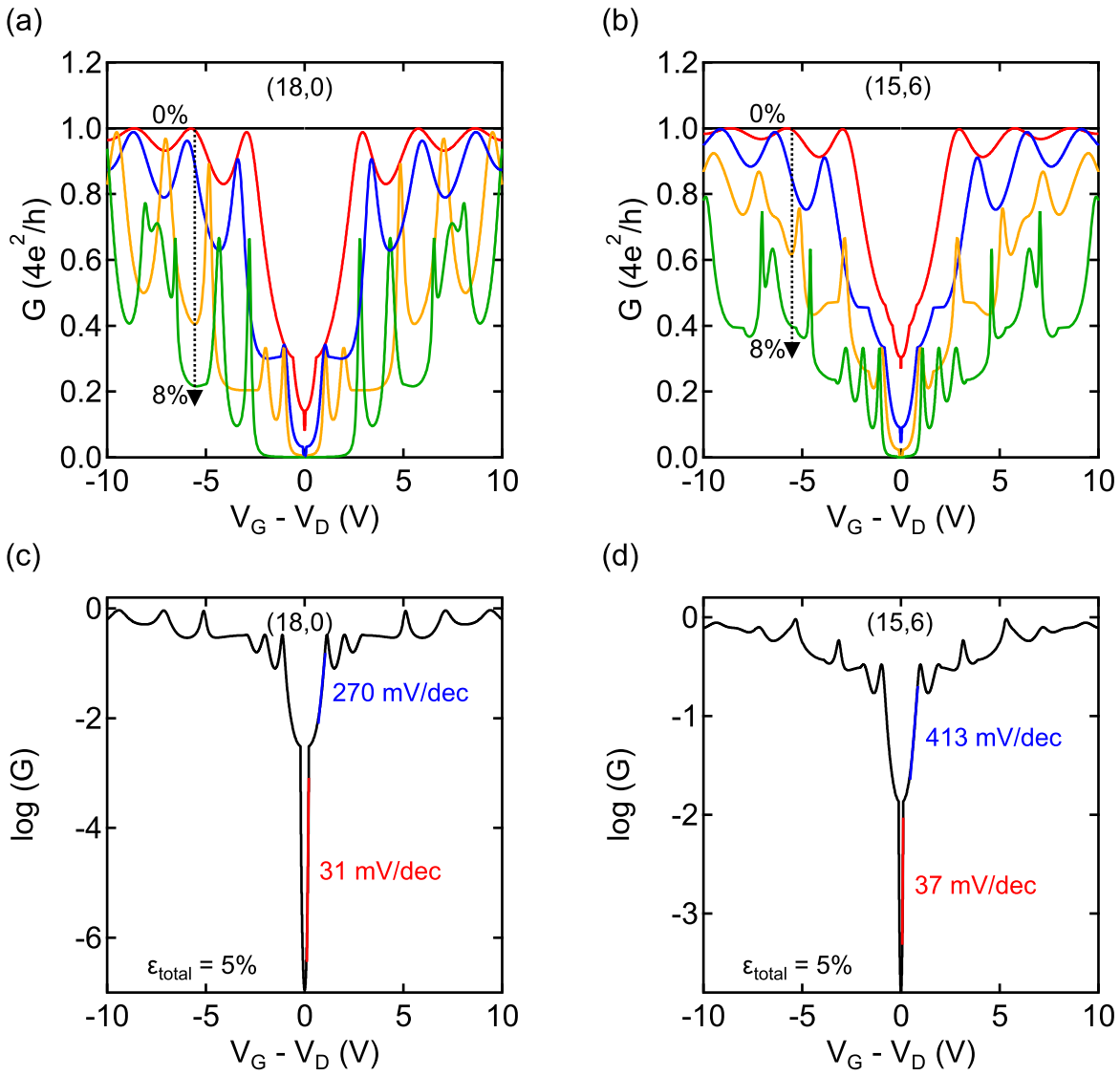

Figure 3.9: Tuning conductance via uniaxial strain in quasi-metallic ($n-m=3I$) SWCNTs. (a)-(b) G vs $(V_{\rm G}-V_{\rm D})$ at $\varepsilon_{\rm total}=0\,\%$ (black), $1\,\%$ (red), $2\,\%$ (blue), $4\,\%$ (gold), $8\,\%$ (green) in a (18,0) and (15,6) SWCNT respectively. (c)-(d) $\log(G)$ vs $(V_{\rm G}-V_{\rm D})$ at $\varepsilon_{\rm total}=5\,\%$ in the above SWCNTs, blue and red lines show the linear subthreshold regions with the corresponding slopes.

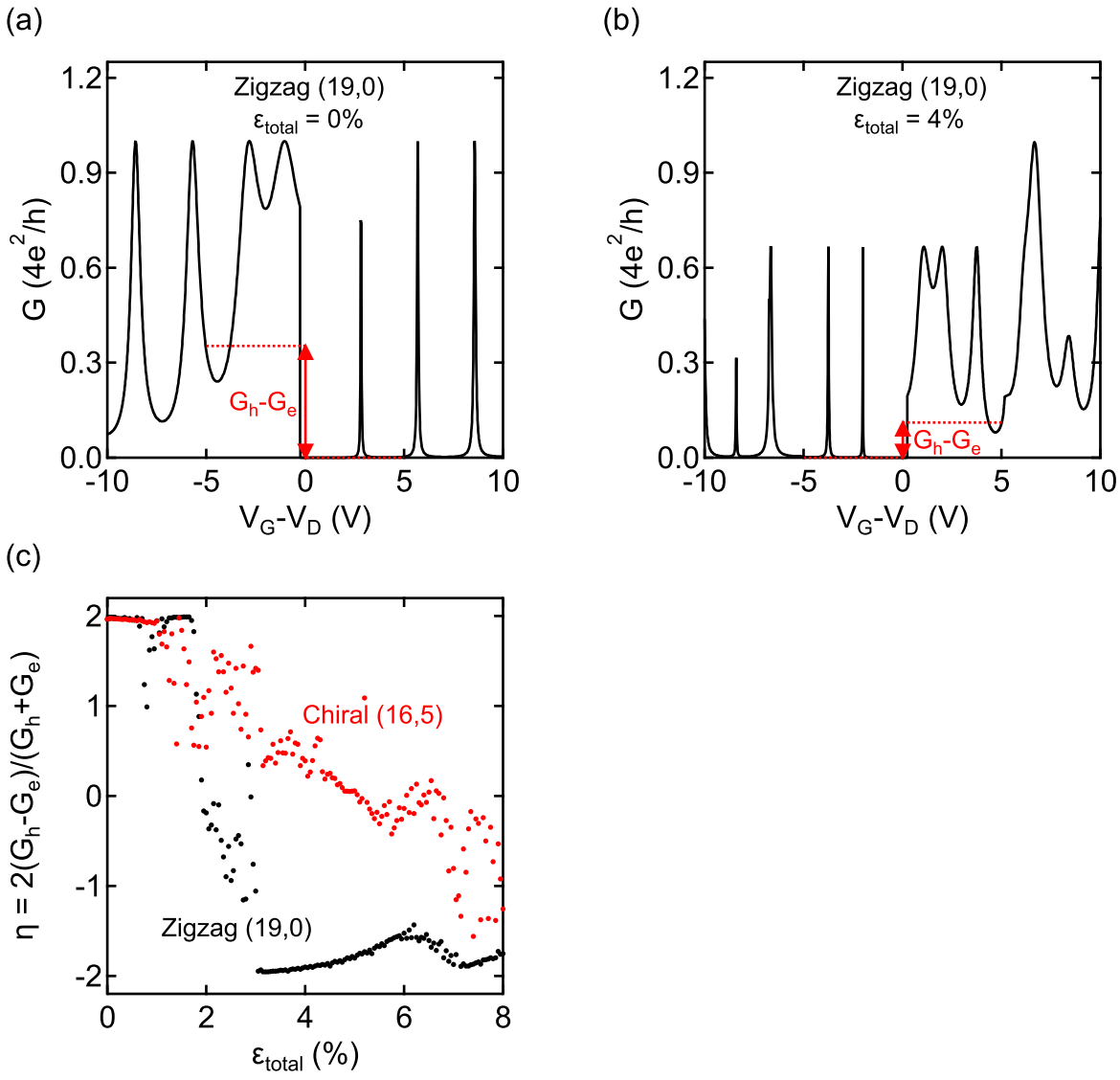

Figure 3.10: Tuning the e-h asymmetry in ultra-short semiconducting SWCNT transistors. (a) G vs $(V_{\mathrm{G}} - V_{\mathrm{D}})$ at $\varepsilon_{\mathrm{total}} = 0$ % in a (19,0) SWCNT. (b) G vs $(V_{\mathrm{G}} - V_{\mathrm{D}})$ at $\varepsilon_{\mathrm{total}} = 4$ % in a (19,0) SWCNT. (c) The relative e-h asymmetry η vs $\varepsilon_{\mathrm{total}}$ for zigzag (19,0) and chiral (16,5) SWCNTs.

plot $\eta - \varepsilon_{\text{total}}$ for two semiconducting SWCNTs with the same diameter in Fig. 3.10(c). It shows that the tunability of the e-h asymmetry is stronger in a zigzag tube (19,0) than in a chiral one (16,5), because η decreases from $+2$ to -2 only within ≈ 2 % strain in the zigzag one, while it requires ≈ 7 % in the chiral one. In summary, using uniaxial strain, I can switch a SWCNT transistor between acting as a zero-dimensional QDs and a one-dimensional waveguide without changing gate voltage. This dual functionality could be used to create re-programmable logic circuits [61].

In this chapter, I detailed the development of the applied theory for quantum transport in strained SWCNT devices. I described strain-induced scalar and vector potentials, the periodic transverse boundary conditions and quantum capacitance in SWCNT transistors. With my transmission model, I predicted that strain can generate valley polarization in metallic SWCNT transistors, lead to subthreshold slope down to ≈ 30 mV/dec with quasi-metallic SWCNTs, and tune the electron-hole transport asymmetry drastically in semiconducting SWCNT transistors.

Chapter 4

Conclusions and Outlook

I have reported the fabrication of strain-tunable suspended SWCNT devices, which combined with our custom-built quantum transport strain engineering (QTSE) platform, will allow me to tune transport in SWCNTs. I developed a detailed applied theoretical model to engineer the quantum Hamiltonian of SWCNT transistors with a uniaxial strain. This will allow me to explore quantum transport (e.g. electron-vibron coupling [3]) in SWCNT nanoelectromechanical systems (NEMS). In this chapter, I first briefly summarize the main results presented previously. I then briefly discuss my plans for future experiments with my fabricated devices and the outlook for strain engineering in SWCNT NEMS.

4.1 Main Results

In Chapter 2, I described our custom instrumentation for electron transport at low temperature in carbon systems under large and tunable mechanical strain. I also reported the optimized fabrication methods for ultra-short suspended SWCNT NEMS. Figure 4.1(a) shows the schematic diagram of our QTSE instrumentation. By bending the substrate with a precision push-screw assembly, a uniaxial strain (theoretically $\sim 1-10\%$) is applied to ultra-short SWCNT channels ($\sim$ 20 nm), thanks to suspended gold cantilever arms. I detailed the fabrication steps to produce clean, high-quality, and strain-tunable suspended SWCNT transistors. I used thin Si wafers with the thickness of $\sim 200\mu m$, which are flexible enough for moderate bending. I suspended the devices by etching the SiO_2 beneath the gold-on-SWCNT breakjunctions. Figure 4.1(b) shows an example of a fabricated device. Finally, I described briefly the wire-bonding and electromigraion procedures needed to create nm-long naked SWCNT channels by creating gaps in the gold junctions.

In Chapter 3, I developed an applied theory for quantum transport in strained SWCNT transistors, including experimental considerations and strain-induced lattice distortions. It

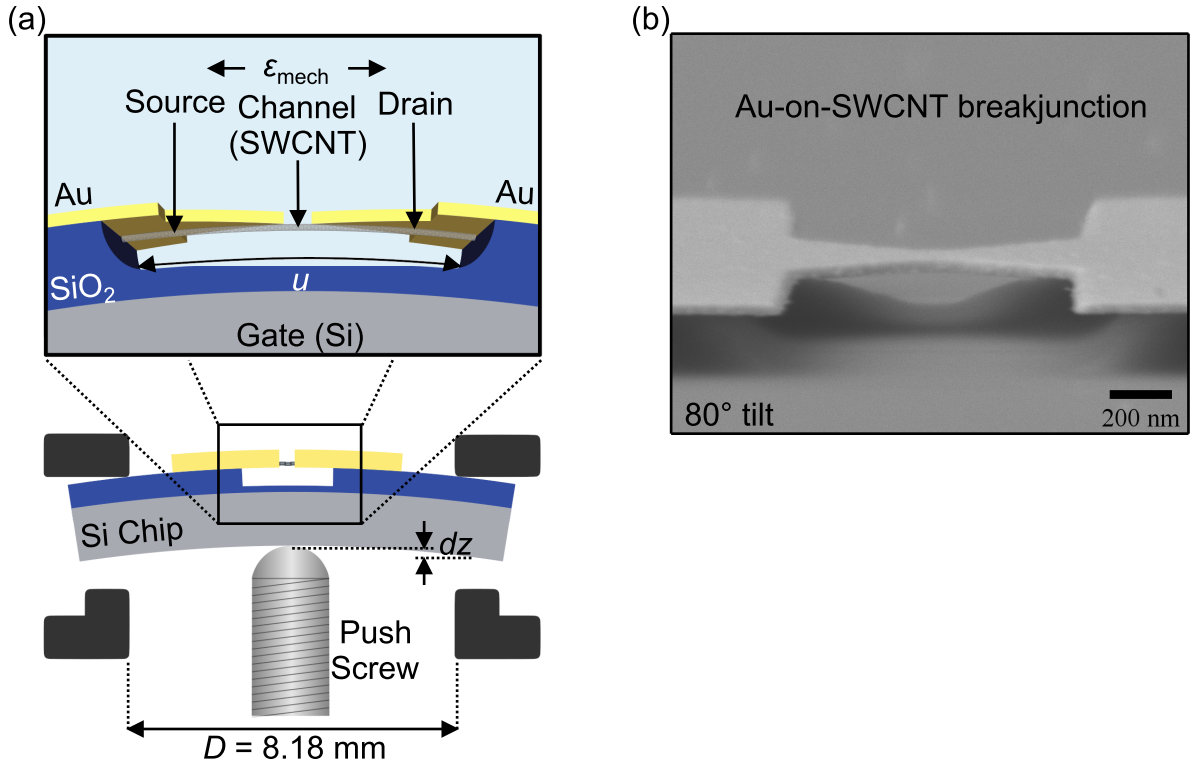

Figure 4.1: Custom-built QTSE instrumentation and suspended SWCNT devices. (a) Side view of the suspended SWCNT device and mechanical strain instrumentation. Figure adapted from Ref. [20]. (b) Tilted-SEM image of a suspended Au-on-SWCNT breakjunction at 80°.

allows me to explore the effects of a scalar and vector potentials arising from the uniaxial strain in SWCNTs. I used this applied theory to predict several quantum transport signatures. I summarize these findings in Fig. 4.2. As stated previously, I will apply the uniaxial strain up to $\sim$ 5% in my experiments. In my theoretical model, I calculated transport signatures for strains up to 8%. I calculated conductance as a function of V_{G} and $\varepsilon_{\mathrm{total}}$ in different types of SWCNTs. I found four major transport signatures: a V_{G} shift of the Dirac point, V_{D}, from the strain-induced scalar potential, a strain-generated valley polarization in metallic SWCNTs, $\sim$ 30 mv/dec sub-threshold transistors in quasi-metallic SWCNTs and a widely tunable electron-hole transport asymmetry in semiconducting SWCNT transistors. Figure 4.2(a) shows the lateral gate position shift of the Dirac point in an armchair SWCNT due to the scalar potential. The minimum conductance in a strained armchair SWCNT is precisely quantized at $G = 1/3 * 4e^2/h$, as shown in Fig. 4.2(b). This is because charge carriers can only pass through K_1 and K_1' valleys. Figure 4.2(c) shows that the strain can set the conductance in quasi-metallic SWCNT devices to zero. These quantum strain transistors

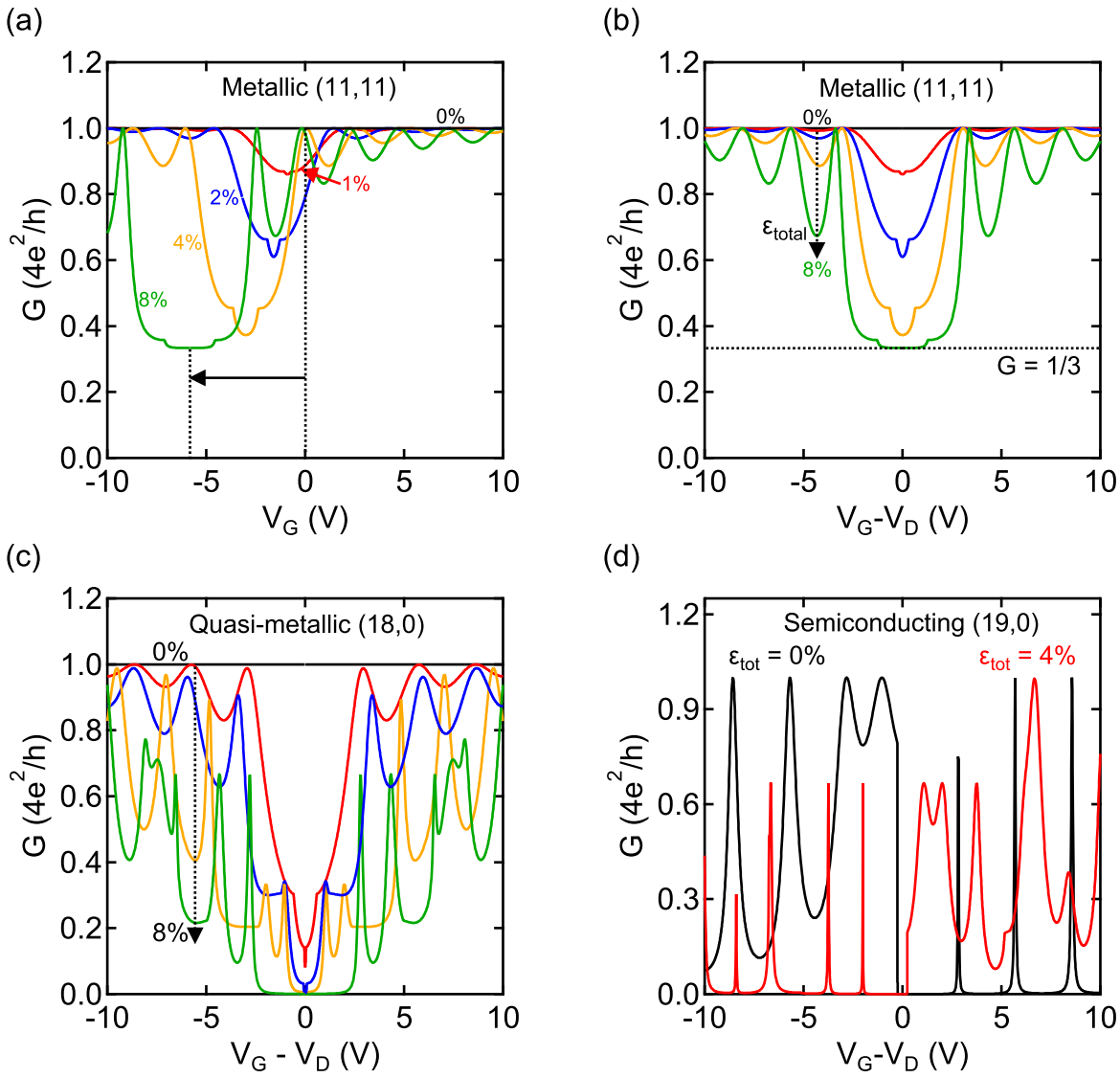

Figure 4.2: Strain-tunable transport signatures in SWCNT transistors. (a) Strain-induced scalar potential shifts the Dirac point in energy. (b) Minimum conductance of $G = 1/3{*}4e^2/h$ is reached in metallic SWCNTs under uniaxial strain, where only charge carriers in K_1 and K_1' valleys contribute to G. (c) In quasi-metallic SWCNTs, I can turn off the transistor completely with the uniaxial strain. (d) In semiconducting SWCNTs, the uniaxial strain can tune the electron-hole transport asymmetry dramatically.

have the subthreshold slope of ~ 30 mV/dec exceeding the thermionic limit 60 mV/dec, as shown in Fig. 3.9 (c)-(d). Figure 4.2(d) indicates the strong tunability of electron-hole transport asymmetry in semiconducting SWCNT transistors using uniaxial strain.

4.2 Outlook for Strain Engineering in SWCNT NEMS

I have shown that I can tune transport behaviors in SWCNT transistors with our QTSE platform and devices, to explore the physics of quantum transport in SWCNTs. In this section, I briefly describe several quantum transport measurements that I am planing with my fabricated devices.

First, I will wire-bond my existing devices and create ultra-short SWCNT channels by etching away gold films via electromigration inside the cryostat. After finishing this sample preparation, I will carry out experiments in a He-3 cryostat ($0.3\ \mathrm{K} - 70\ \mathrm{K}$) with in-situ strain control and magnetic fields up to 9T. The exact chirality of the SWCNT in my devices can be determined by studying their quantum dot excitation spectrum in our dilution cryostat equipped with a 3D-XYZ magnet. I will then analyze these complete data sets using the applied theoretical model described in Chapter 3.

There is a minimum subthreshold slope in conventional transistors, known as the thermionic limit. In quasi-metallic SWCNTs, the uniaxial strain can open bandgaps, i.e. like a phase transition between metallic and semiconducting states. I can thus achieve extremely high on/off ratio quantum strain transistors exceeding this limit, see subsection 3.4.3. My first experimental goal will be to obtain the data demonstrating this. With uniaxial strain, I expect valley-polarized currents in metallic SWCNTs, which has potential applications in valleytronics [60]. Note that it is less likely to find a metallic SWCNT in my devices, because the armchair chirality is less common than semiconducting. The strain-tunable bandgap in semiconducting SWCNTs changes the heights of the Schottky barriers at the interfaces of Au-covered (source/drain) and naked (channel) SWCNT sections. This leads to the strain tunability of electron-hole transport asymmetry, i.e. two-in-one quantum transistors, as discussed in subsection 3.4.4. I aim to demonstrate the tunability (programming) of these two-in-one quantum NEMS.

Most interestingly, I expect to explore electron-vibron couplings [3] and the Kondo effect [30] with mechanically tuning of the quantum dot Hamiltonian. With the 3D-vector magnet and millikelvin temperature, I aim to understand some of the effects of mechanical strain on spin-orbit and electron-electron interactions in SWCNT quantum dots.

A separate project involves applying AC gate voltages on the back-gate (heavily doped Si

substrate) to generate mechanical vibrations in SWCNT resonators. Previously, few-hundred GHz frequencies were found in such SWCNT devices in our group [40]. Now with the ability of applying a large and tunable strains, I can increase this frequency up to terahertz (THz) regime and explore (tune) the NEMS' energy dissipation mechanisms [40].

Appendices

Appendix A

Details of SWCNT Quantum Strain Transport Calculations

This appendix presents the MATHEMATICA code used to calculate conductance in SWCNT transistors as a function of Fermi energy (i.e. gate voltage), and applied uniaxial strain. The code consists of three sections: the first calculates transmission probabilities in strained graphene strips, following Refs. [45, 46]. The second includes the momentum quantization caused by the periodic boundary condition in SWCNTs. The third calculates the conductance in SWCNT transistors considering experimental variables and then outputs the data.

In[1]:=
```
(****************************************** First Section ******************************************)
(* clear all variables and symbols *)
ClearAll["Global`*"]

(* Pauli Spin Matrices *)
σx = {{0, 1}, {1, 0}};
MatrixForm[%];
σy = {{0, -I}, {I, 0}};
MatrixForm[%];

(* Momentum Operators *)
px[Ψ_] := -I*ħ*D[Ψ, x];
py[Ψ_] := -I*ħ*D[Ψ, y];

(*Plane Wave Test Solution, transversal momentum can be positive or negative,
but we only worried about positive x (right moving) solutions*)
Ψ[k_, x_, SGN_] := E^I*(k*x) E^I*SGN*(q*y);

(*Strained Hamiltonian in graphene*)
(*Note:  To preserve time reversal symmetry, when q changes sign, so does A*)
H[Ψ_, SGN_] :=
  v_F*{{σx*(px[Ψ] - ħ*Ax*Ψ) + σy*(py[Ψ] - SGN*ħ*Ay*Ψ), 0}, {0, σx*(px[Ψ] - ħ*Ax*Ψ) - σy*(py[Ψ] - SGN*ħ*Ay*Ψ)}};

(*Determine complete matrix to be diagonalized for positive q*)
Print["Final form of matrix for q>0:\r"];
MATp[k_, x_] = MatrixForm[ArrayFlatten[H[Ψ[k, x, 1], 1]] + (e*V + γ1)*IdentityMatrix[4]*Ψ[k, x, 1]];
MatrixForm[FullSimplify[%]]

(*Calculate Eigenvectors for positive q*)
EVp = Eigenvectors[%];

(*Determine complete matrix to be diagonalized for negative q*)
Print["\rFinal form of matrix for q<0:\r"];
MATn[k_, x_] = MatrixForm[ArrayFlatten[H[Ψ[k, x, -1], -1]] + (e*V + γ1)*IdentityMatrix[4]*Ψ[k, x, -1]];
MatrixForm[FullSimplify[%]]

(*Calculate Eigenvectors for negative q*)
EVn = Eigenvectors[%];

(*Isolates a useful quantity, z (from Tworzydlo), for simplification*)
zz = Factor[FullSimplify[PowerExpand[EVn[[2]][[1]]]]];
Print["\rForm of z:\r"];
Print["z=", zz]

(*Simplify q>0 eigenvectors and put in terms of z like Tworzydlo*)
Refine[FullSimplify[PowerExpand[EVp]]];

(*2 of 4 vecors have a 1/z term instead of simply a  z term, so we multiply
 both components by z so all eigenvectors are the same length (normalization), and put solutions in terms of z*)
EVpz = Refine[FullSimplify[PowerExpand[EVp]]];
EVpz[[2]] = FullSimplify[EVpz[[2]]*zz];
EVpz[[4]] = FullSimplify[EVpz[[4]]*-zz];
EVpz = EVpz /. FullSimplify[PowerExpand[zz]] :> z /. FullSimplify[PowerExpand[1/zz]] :> 1/z /.
    FullSimplify[PowerExpand[-1/zz]] :> -1/z /. FullSimplify[PowerExpand[-zz]] :> -z;
Print["\rEigenvectors for q>0:\r"];
Print[MatrixForm[EVpz[[1]]], "  ", MatrixForm[EVpz[[2]]], "  ", MatrixForm[EVpz[[3]]], "  ", MatrixForm[EVpz[[4]]]]

(*Simplify q<0 eigenvectors and put in terms of z*)
FullSimplify[PowerExpand[EVn]];
```

```
(*2 of 4 vecors have a 1/z term instead of simply a  z term, so we multiply
 both components by z so all eigenvectors are the same length (normalization), and put solutions in terms of z*)
EVnz = FullSimplify[PowerExpand[EVn]];
EVnz[[1]] = FullSimplify[EVnz[[1]] * zz];
EVnz[[3]] = FullSimplify[EVnz[[3]] * -zz];
EVnz = EVnz /. FullSimplify[PowerExpand[zz]] :> z /. FullSimplify[PowerExpand[1 / zz]] :> 1 / z /.
    FullSimplify[PowerExpand[-1 / zz]] :> -1 / z /. FullSimplify[PowerExpand[-zz]] :> -z;
Print["\rEigenvectors for q<0:\r"];
Print[MatrixForm[EVnz[[1]]], "  ", MatrixForm[EVnz[[2]]], "  ", MatrixForm[EVnz[[3]]], "  ", MatrixForm[EVnz[[4]]]]

(* Therefore, plane wave solutions are: (taking z to be either positive or negative)*)
ΨΨ =
  E^I*(k*x) * (a*MatrixForm[EVpz[[4]]] * E^I*(q*y) + ap*MatrixForm[EVpz[[3]]] * E^I*(q*y) +
     b*MatrixForm[EVnz[[2]]] * E^-I*(q*y) + bp*MatrixForm[EVnz[[1]]] * E^-I*(q*y));
Print["\rPlane wave solutions to the Hamiltonian Equation A2:\r\r ΨΨ =", ΨΨ, "\r"]

(*Note:  There are four 4x1 eigenvectors, but we can make the system of of equations
 with just one of them, as they will be equivalent. (As they do in Tworzydlo).  We proceed using
 the more general form of k's and q's rather than z's*)

(*System of equations vector from the eigenvector*)
SYS[k_, q_, Ax_, Ay_] := Evaluate[FullSimplify[PowerExpand[Delete[Delete[EVn[[2]], 4], 3]]]]

(*System of equations: This is eq.A8-A13 from Tworzydlo
    4 expressions that match up the left and right moving waves in the graphene channel and in the contacts*)
(*Have to change sign of Ax when we change sign of k, cause they go together*)
(*Need to include Ax in exponentials in the channel (α,β)*)
ex1 = FullSimplify[SYS[k1, q1, 0, 0][[1]] * Ψ[k1, 0, 1] + r * SYS[-k1, q1, 0, 0][[1]] * Ψ[-k1, 0, 1] ==
     (α * SYS[k2 * vxx, q2 * vyy, Ax * vxx, Ay * vyy][[1]] * Ψ[(k2 - Ax), 0, 1] +
       β * SYS[-k2 * vxx, q2 * vyy, -Ax * vxx, Ay * vyy][[1]] * Ψ[(-k2 + Ax), 0, 1])];
ex2 = FullSimplify[SYS[k1, q1, 0, 0][[2]] * Ψ[k1, 0, 1] + r * SYS[-k1, q1, 0, 0][[2]] * Ψ[-k1, 0, 1] ==
     (α * SYS[k2 * vxx, q2 * vyy, Ax * vxx, Ay * vyy][[2]] * Ψ[(k2 - Ax), 0, 1] +
       β * SYS[-k2 * vxx, q2 * vyy, -Ax * vxx, Ay * vyy][[2]] * Ψ[(-k2 + Ax), 0, 1])];
ex3 = FullSimplify[t * SYS[k1, q1, 0, 0][[1]] * Ψ[k1, L - L, 1] ==
     (α * SYS[k2 * vxx, q2 * vyy, Ax * vxx, Ay * vyy][[1]] * Ψ[(k2 - Ax), L, 1] +
       β * SYS[-k2 * vxx, q2 * vyy, -Ax * vxx, Ay * vyy][[1]] * Ψ[(-k2 + Ax), L, 1])];
ex4 = FullSimplify[t * SYS[k1, q1, 0, 0][[2]] * Ψ[k1, L - L, 1] ==
     (α * SYS[k2 * vxx, q2 * vyy, Ax * vxx, Ay * vyy][[2]] * Ψ[(k2 - Ax), L, 1] +
       β * SYS[-k2 * vxx, q2 * vyy, -Ax * vxx, Ay * vyy][[2]] * Ψ[(-k2 + Ax), L, 1])];

(*Solve the system of equations for t*)
tt = FullSimplify[Solve[{ex1, ex2, ex3, ex4}, {r, t, α, β}]][[1]][[2]][[2]]

(*Take modulus for total transmission,and substitute to put evertthing in terms of k's and q's*)
TG =
  FullSimplify[
   Abs[tt /. q1 :> q /. q2 :> q /. Sqrt[k1^2 + q^2] :> kF1 /. Sqrt[vxx^2 * (Ax - k2)^2 + vyy^2 * (Ay - q)^2] :> kF2 /. k1 :> Sqrt[kF1^2 - q^2] /.
      k2 :> vxx^-1 * Sqrt[kF2^2 - vyy^2 * (q - Ay)^2] + Ax]^2];
Print["\rGeneral Graphene transmission: \r", FullSimplify[%]]


Final form of matrix for q>0:
```

Out[12]//MatrixForm=

$$\begin{pmatrix} e^{i(kx+qy)}(eV+\gamma 1) & e^{i(kx+qy)}(-Ax+iAy+k-iq)\hbar v_F & 0 & 0 \\ e^{i(kx+qy)}(-Ax-iAy+k+iq)\hbar v_F & e^{i(kx+qy)}(eV+\gamma 1) & 0 & 0 \\ 0 & 0 & e^{i(kx+qy)}(eV+\gamma 1) & e^{i(kx+qy)}(-Ax-iAy+k+iq)\hbar v_F \\ 0 & 0 & e^{i(kx+qy)}(-Ax+iAy+k-iq)\hbar v_F & e^{i(kx+qy)}(eV+\gamma 1) \end{pmatrix}$$

Final form of matrix for q<0:

Out[16]//MatrixForm=

$$\begin{pmatrix} e^{i(kx-qy)}(eV+\gamma 1) & e^{i(kx-qy)}(-Ax-iAy+k+iq)\hbar v_F & 0 & 0 \\ e^{i(kx-qy)}(-Ax+iAy+k-iq)\hbar v_F & e^{i(kx-qy)}(eV+\gamma 1) & 0 & 0 \\ 0 & 0 & e^{i(kx-qy)}(eV+\gamma 1) & e^{i(kx-qy)}(-Ax+iAy+k-iq)\hbar v_F \\ 0 & 0 & e^{i(kx-qy)}(-Ax-iAy+k+iq)\hbar v_F & e^{i(kx-qy)}(eV+\gamma 1) \end{pmatrix}$$

Form of z:

$$z=\frac{Ax+iAy-k-iq}{\sqrt{(Ax-k)^2+(Ay-q)^2}}$$

Eigenvectors for q>0:

$$\begin{pmatrix}0\\0\\z\\1\end{pmatrix}\quad\begin{pmatrix}1\\z\\0\\0\end{pmatrix}\quad\begin{pmatrix}0\\0\\-z\\1\end{pmatrix}\quad\begin{pmatrix}1\\-z\\0\\0\end{pmatrix}$$

Eigenvectors for q<0:

$$\begin{pmatrix}0\\0\\1\\z\end{pmatrix}\quad\begin{pmatrix}z\\1\\0\\0\end{pmatrix}\quad\begin{pmatrix}0\\0\\1\\-z\end{pmatrix}\quad\begin{pmatrix}-z\\1\\0\\0\end{pmatrix}$$

Plane wave solutions to the Hamiltonian Equation A2:

$$\Psi\Psi = e^{ikx}\left(bp\,e^{-iqy}\begin{pmatrix}0\\0\\1\\z\end{pmatrix}+ap\,e^{iqy}\begin{pmatrix}0\\0\\-z\\1\end{pmatrix}+a\,e^{iqy}\begin{pmatrix}1\\-z\\0\\0\end{pmatrix}+b\,e^{-iqy}\begin{pmatrix}z\\1\\0\\0\end{pmatrix}\right)$$

Out[42]=

$$\frac{k1\,(Ax-k2)\,vxx}{k1\,(Ax-k2)\,vxx\,\text{Cos}\left[(Ax-k2)\,L\right]-i\left(q1\,(Ay-q2)\,vyy+\sqrt{k1^2+q1^2}\,\sqrt{(Ax-k2)^2\,vxx^2+(Ay-q2)^2\,vyy^2}\right)\text{Sin}\left[(Ax-k2)\,L\right]}$$

General Graphene transmission:

$$\text{Abs}\left[\frac{(kF1-q)\,(kF1+q)\left(kF2^2-(Ay-q)^2\,vyy^2\right)}{\left(\sqrt{(kF1-q)\,(kF1+q)}\,\sqrt{kF2^2-(Ay-q)^2\,vyy^2}\,\text{Cos}\left[\frac{L\sqrt{kF2^2-(Ay-q)^2\,vyy^2}}{vxx}\right]-i\,(kF1\,kF2+(Ay-q)\,q\,vyy)\,\text{Sin}\left[\frac{L\sqrt{kF2^2-(Ay-q)^2\,vyy^2}}{vxx}\right]\right)^2}\right]$$

In[45]:=

```
(****************************************** Second Section ******************************************)
(* clear all variables and symbols *)
ClearAll["Global`*"]
(* Quantization of y components of fermi wavevectors in SWCNT channels *)
```

```
q[N_, W_, α_] := 2 π / W * (N + α);
(* Shortcut to final results for T *)
Tϕ[kF1_, kF2_, q_, L_, Ay_] :=
  Abs[ ((kF1 - q) (kF1 + q) (kF2^2 - (Ay - q)^2 vyy^2)) /
    (√((kF1 - q) (kF1 + q)) √(kF2^2 - (Ay - q)^2 vyy^2) Cos[ (L √(kF2^2 - (Ay - q)^2 vyy^2)) / vxx ] -
      i (kF1 kF2 + (Ay - q) q vyy) Sin[ (L √(kF2^2 - (Ay - q)^2 vyy^2)) / vxx ])^2 ];
Tn[μL_, μc_, Nq_, L_, W_, Ay_, α_] := Tϕ[μL / (ħ * vF), μc / (ħ * vF), q[Nq, W, α], L, Ay];

(****************************************** Third Section ******************************************)
(* Constants *)
kB = 1.4×10^(-23); (* Boltzman Constant  J/K *)
e = 1.6*10^-19; (* Elementary Charge in C *)
ħ = 1.05*10^(-34); (* Planck's constant /2π J.s *)
hbar = ħ;
h = 6.63* 10^(-34); (* J.s *)
t0 = 2.7*e;
a = 1.42*^-10; (* C-C bond length in m *)
β = 2.5; (* Dimensionless electron-phonon coupling parameter *)
vF = 3 / 2 * a * t0 / hbar; (* Fermi Velocity in CNT *)
Kb = 1.38*10^-23; (* Boltzmann constant in J/K *)

(* Parameters *)
(* Coordinate system: a1 = (3/2, √3/2)a, a2 = (3/2, -√3/2)a; Ch = n*a1 + m*a2, n > 0, -(n/2) < m ≤ n, Laird_2015 *)
n = 16; m = 5; (* SWCNT Chiral Vector Indices *)
If[Mod[(n - m), 3] == 0, α = 0, α = 1 / 3]; (* Value of α, Kolomeisky12 *)
(*Δϕ=-0.12*e;(* Contact doping in J *)*)
Δϕ = -0.26 * e;(* Contact doping in J *)
L = 20.0 * 10^(-9); (* Device Length in m *)
W = √3 * a * √(n^2 + n * m + m^2); (* Tube circumference in m *)
d = W / Pi; (* Tube diameter in m *)
r = d / 2; (* Tube radius in m *)
T = 0; (* Temperature *)

Θ0 = ArcTan[ (√3 * m) / (2 n + m) ];     (* SWCNT Chiral Angle, -(π/6) < Θ0 ≤ π/6 *)
Θ = π / 6 - Θ0; (* Angle of SWCNT (rel. to zigzag direction) when 0 ≤ Θ0 ≤ π/6 *)
δL = 0.0*10^(-9); (* Built in  Stretch, use for electrostatic gating model *)
minε = 0.0 / 100.0; (* Minimum Applied Strain *)
maxε = 8.0 / 100.0; (* Maximum Applied Strain *)
Nεstep = 8; (* Number of strain steps *)
εStep = (maxε - minε) / Nεstep; (* Size of stain steps *)
ε0 = 0*2.6 / 100.0; (* Built in strain *)
ν = 0.165;(* Poisson Ratio in Graphene *)
(*ν=0.20;(* Poisson Ratio in Yang2000 *)*)
EorH = -1; (* 1:μc increases, -1:μc decreases *)

(*++++++++++++++++++++++++++++++++++++++++++++++++++++++++++++++++++++++++++++++++++++++++++++++++++++++++*)
dair = 50.0*10^(-9);     (* Thicknes of Air (m) *)
dsio2 = 0.0*10^(-9);   (* Thicknes of SiO2 (m) *)
∈air = 8.85*10^(-12); (* Permittivity of Vacuum in F/m *)
∈sio2 = 3.9*8.85*10^(-12); (* Permittivity of SiO2 in F/m *)
∈ = 4*π*∈air;(* 4π Vacuum Permittivity in F/m *)

μcMax = 0.5*e; (* Fermi energy range: -μcMax → μcMax*)
Nstep = 2000; (* Number of Fermi energy steps *)
μcStep = μcMax / Nstep; (* Size of Fermi energy steps *)

Rc = 0*800.0; (*Contact Resistance (0 if want to take into acct later) in Ohms*)
(*gε=3.0*e; (*change in workfunction per % strain (choi2010),
```

```
set to 0 to focus on the impact of vector potentials *)*)
gε = 0 * 3.0 * e; (*change in workfunction per % strain (choi2010),
set to 0 to focus on the impact of vector potentials *)
f[μc_] = 1 / (1 + E ^ (EorH * (μ1 - μc) / (Kb * T))); (* Fermi function *)
ex0 = D[f[μc], μc]; (* Partial derivative of the Fermi function*)
(*++++++++++++++++++++++++++++++++++++++++++++++++++++++++++++++++++++++++++++++++++++++++++*)
Cg = If[dsio2 == 0, (2 * Pi * ϵair) / ArcCosh[dair / r],
   (2 * Pi * ϵsio2) / ((ϵsio2 / ϵair) * ArcCosh[dair / r] + ArcCosh[(dair + dsio2) / (r + dair)])];
(*Geometric Capacitance in F/m. McRae17*)

Nmax[EF_] := IntegerPart[(Abs[EF] / (ℏ * vF)) * (W / (2 * π)) - α + 1];
(* Fermi vector in leads should be larger than the transverse wavevector *)
(*++++++++++++++++++++++++++++++++++++++++++++++++++++++++++++++++++++++++++++++++++++++++++*)
(* Create arrays to store data *)
Array[VVg, (Nstep + 1) * (Nεstep + 1) - 1];
Array[εε, (Nstep + 1) * (Nεstep + 1) - 1];

Array[AAy1, (Nstep + 1) * (Nεstep + 1) - 1];
Array[AAy2, (Nstep + 1) * (Nεstep + 1) - 1];
Array[AAy3, (Nstep + 1) * (Nεstep + 1) - 1];
Array[AAy4, (Nstep + 1) * (Nεstep + 1) - 1];
Array[AAy5, (Nstep + 1) * (Nεstep + 1) - 1];
Array[AAy6, (Nstep + 1) * (Nεstep + 1) - 1];
Array[EEg1, (Nstep + 1) * (Nεstep + 1) - 1];
Array[EEg2, (Nstep + 1) * (Nεstep + 1) - 1];
Array[EEg3, (Nstep + 1) * (Nεstep + 1) - 1];
Array[EEg4, (Nstep + 1) * (Nεstep + 1) - 1];
Array[EEg5, (Nstep + 1) * (Nεstep + 1) - 1];
Array[EEg6, (Nstep + 1) * (Nεstep + 1) - 1];

Array[DDos, (Nstep + 1) * (Nεstep + 1) - 1];
Array[CCdos, (Nstep + 1) * (Nεstep + 1) - 1];
Array[CCtot, (Nstep + 1) * (Nεstep + 1) - 1];
Array[μμ, (Nstep + 1) * (Nεstep + 1) - 1];
Array[nn, (Nstep + 1) * (Nεstep + 1) - 1];
Array[GG1, (Nstep + 1) * (Nεstep + 1) - 1] ;
Array[GG2, (Nstep + 1) * (Nεstep + 1) - 1] ;
Array[GG3, (Nstep + 1) * (Nεstep + 1) - 1] ;
Array[GG4, (Nstep + 1) * (Nεstep + 1) - 1] ;
Array[GG5, (Nstep + 1) * (Nεstep + 1) - 1] ;
Array[GG6, (Nstep + 1) * (Nεstep + 1) - 1] ;
Array[GG, (Nstep + 1) * (Nεstep + 1) - 1] ;
Array[Fanonum, (Nstep + 1) * (Nεstep + 1) - 1] ;

(* For loop to increase strain *)
For[SStep = 0, SStep ≤ (Nεstep), SStep += 1,

 (* Increment strain *)
 ε = (minε + (SStep) * εStep);

 (* Change Fermi velocity anisotropy *)
 vxx = 1 - (β - 1) * (ε + ε0);
 vyy = 1 + (β - 1) * ν * (ε + ε0);

 (*Scalar potential*)
 Δμε[εtotal_] := gε * (1 - ν) * (εtotal);

 (* Vector potentials in K1, K2, K3 valleys *)
 Ay1[θ_] := (8 × √3 π (ε + ε0) ν Sin[θ] + 9 β (ε + ε0) (1 + ν) Sin[3 * θ]) / (18 a);
 Ay2[θ_] := ((ε + ε0) (12 π ν Cos[θ] - 4 × √3 π ν Sin[θ] + 9 β (1 + ν) Sin[3 * θ])) / (18 a);
```

```
Ay3[Θ_] := ((ε + ε0) (-12 π ν Cos[Θ] - 4 √3 π ν Sin[Θ] + 9 β (1 + ν) Sin[3 * Θ])) / (18 a);

(* Calculate band gaps of first 3 subbands in 6 valleys; Yang2000 *)
En1[j_] := hbar * vF * Abs[(2 / (3 * d)) * (3 * j - (n - m)) - Ay1[Θ]];
EnList1 = SortBy[Range[Round[(n - m) / 3] - 4, Round[(n - m) / 3] + 4], En1];
(* Altenative: MinimalBy[Range[Round[n/3]-4,Round[n/3]+4],g,9] *)

En2[j_] := hbar * vF * Abs[(2 / (3 * d)) * (3 * j - (n - m)) - Ay2[Θ]];
EnList2 = SortBy[Range[Round[(n - m) / 3] - 4, Round[(n - m) / 3] + 4], En2];
(* Altenative: MinimalBy[Range[Round[n/3]-4,Round[n/3]+4],g,9] *)

En3[j_] := hbar * vF * Abs[(2 / (3 * d)) * (3 * j - (n - m)) - Ay3[Θ]];
EnList3 = SortBy[Range[Round[(n - m) / 3] - 4, Round[(n - m) / 3] + 4], En3];
(* Altenative: MinimalBy[Range[Round[n/3]-4,Round[n/3]+4],g,9] *)

En4[j_] := hbar * vF * Abs[-(2 / (3 * d)) * (3 * j - (n - m)) - (-Ay1[Θ])];
EnList4 = SortBy[Range[Round[(n - m) / 3] - 4, Round[(n - m) / 3] + 4], En4];
(* Altenative: MinimalBy[Range[Round[n/3]-4,Round[n/3]+4],g,9] *)

En5[j_] := hbar * vF * Abs[-(2 / (3 * d)) * (3 * j - (n - m)) - (-Ay2[Θ])];
EnList5 = SortBy[Range[Round[(n - m) / 3] - 4, Round[(n - m) / 3] + 4], En5];
(* Altenative: MinimalBy[Range[Round[n/3]-4,Round[n/3]+4],g,9] *)

En6[j_] := hbar * vF * Abs[-(2 / (3 * d)) * (3 * j - (n - m)) - (-Ay3[Θ])];
EnList6 = SortBy[Range[Round[(n - m) / 3] - 4, Round[(n - m) / 3] + 4], En6];
(* Altenative: MinimalBy[Range[Round[n/3]-4,Round[n/3]+4],g,9] *)

(* For loop to increase the Fermi energy *)
For[Step = 0, Step ≤ Nstep, Step += 1,

 (* Start with zero Fermi energy, then calculate Vg (Ilani06) *)
 If[Δμε[(ε + ε0)] == 0,
  μc = EorH * Step * μcStep;
  If[Step == 0, Vgate = 0, Vgate += EorH * μcStep * If[T == 0.0 && Dos == 0.0, 1, Cdos / Ctot]],];

 (* Same sample points' distance around the fermi level for symmetry *)
 If[Δμε[(ε + ε0)] ≠ 0,
  If[Step == 0, μc = Δμε[(ε + ε0)], If[EorH > 0, μc = EorH * (Step - 1) * μcStep + Ceiling[Δμε[(ε + ε0)] / μcStep] * μcStep,
    μc = EorH * (Step - 1) * μcStep + Floor[Δμε[(ε + ε0)] / μcStep] * μcStep]];
  If[Step == 0, Vgate = 0,
   If[Step == 1,
    Vgate += EorH * If[EorH > 0, Abs[Ceiling[Δμε[(ε + ε0)] / μcStep] * μcStep - Δμε[(ε + ε0)]],
       Abs[Floor[Δμε[(ε + ε0)] / μcStep] * μcStep - Δμε[(ε + ε0)]]] * If[T == 0.0 && Dos == 0.0, 1, Cdos / Ctot],
    Vgate += EorH * μcStep * If[T == 0.0 && Dos == 0.0, 1, Cdos / Ctot]]],];

 (* Calculate density of states, quantum capacitance, total capacitance, Biercuk08*)
 Dos1 =
  4 / (Pi * hbar * vF) * (If[En1[EnList1[[1]]] == 0, 1, Re[1 / √(1 - (En1[EnList1[[1]]] / μc)^2)]] +
     Re[1 / √(1 - (En1[EnList1[[2]]] / μc)^2)] + Re[1 / √(1 - (En1[EnList1[[3]]] / μc)^2)]);
 Dos2 =
  4 / (Pi * hbar * vF) * (If[En2[EnList2[[1]]] == 0, 1, Re[1 / √(1 - (En2[EnList2[[1]]] / μc)^2)]] +
     Re[1 / √(1 - (En2[EnList2[[2]]] / μc)^2)] + Re[1 / √(1 - (En2[EnList2[[3]]] / μc)^2)]);
 Dos3 =
  4 / (Pi * hbar * vF) * (If[En3[EnList3[[1]]] == 0, 1, Re[1 / √(1 - (En3[EnList3[[1]]] / μc)^2)]] +
     Re[1 / √(1 - (En3[EnList3[[2]]] / μc)^2)] + Re[1 / √(1 - (En3[EnList3[[3]]] / μc)^2)]);
 Dos4 =
  4 / (Pi * hbar * vF) * (If[En4[EnList4[[1]]] == 0, 1, Re[1 / √(1 - (En4[EnList4[[1]]] / μc)^2)]] +
     Re[1 / √(1 - (En4[EnList4[[2]]] / μc)^2)] + Re[1 / √(1 - (En4[EnList4[[3]]] / μc)^2)]);
 Dos5 =
```

```
 4 / (Pi * hbar * vF) * (If[En5[EnList5[[1]]] == 0, 1, Re[1/√(1 - (En5[EnList5[[1]]] / μc)^2)]] +
    Re[1/√(1 - (En5[EnList5[[2]]] / μc)^2)] + Re[1/√(1 - (En5[EnList5[[3]]] / μc)^2)]);
Dos6 =
 4 / (Pi * hbar * vF) * (If[En6[EnList6[[1]]] == 0, 1, Re[1/√(1 - (En6[EnList6[[1]]] / μc)^2)]] +
    Re[1/√(1 - (En6[EnList6[[2]]] / μc)^2)] + Re[1/√(1 - (En6[EnList6[[3]]] / μc)^2)]);
Dos = (Dos1 + Dos2 + Dos3 + Dos4 + Dos5 + Dos6) / 6;

(* Calculate Quantume Capacitance,
Note that the numerical integration will not work when T is very low (~1K or even higher) & CNT
 Diameter is small (<2nm) *)
Intlimit = EorH*0.7*e;
If[T == 0.0, Cdos = e^2 * Dos, If[EorH > 0,
  Cdos = NIntegrate[4*e^2 / (Pi*hbar*vF) * (Re[1/√(1 - (En[1] / μ1)^2)] + Re[1/√(1 - (En[2] / μ1)^2)]) * ex0,
    {μ1, 0, Intlimit}],
  Cdos = NIntegrate[4*e^2 / (Pi*hbar*vF) * (Re[1/√(1 - (En[-1] / μ1)^2)] + Re[1/√(1 - (En[-2] / μ1)^2)]) * ex0,
    {μ1, Intlimit, 0}]]];

Ctot = 1 / (1 / Cg + 1 / Cdos); (* Total capacitance *)
ntot = Ctot * (Vgate); (* Carrier density *)
VVg[Step + (SStep) * (Nstep + 1)] = Vgate / e; (* Gate voltage needed to achieve such Fermi energy *)
εε[Step + (SStep) * (Nstep + 1)] = ε; (* Store total strain *)

(* Store relevant results *)
AAy1[Step + (SStep) * (Nstep + 1)] = Ay1[Θ];
AAy2[Step + (SStep) * (Nstep + 1)] = Ay2[Θ];
AAy3[Step + (SStep) * (Nstep + 1)] = Ay3[Θ];
AAy4[Step + (SStep) * (Nstep + 1)] = -Ay1[Θ];
AAy5[Step + (SStep) * (Nstep + 1)] = -Ay2[Θ];
AAy6[Step + (SStep) * (Nstep + 1)] = -Ay3[Θ];
EEg1[Step + (SStep) * (Nstep + 1)] = 2 * En1[EnList1[[1]]] / e;
EEg2[Step + (SStep) * (Nstep + 1)] = 2 * En2[EnList2[[1]]] / e;
EEg3[Step + (SStep) * (Nstep + 1)] = 2 * En3[EnList3[[1]]] / e;
EEg4[Step + (SStep) * (Nstep + 1)] = 2 * En4[EnList4[[1]]] / e;
EEg5[Step + (SStep) * (Nstep + 1)] = 2 * En5[EnList5[[1]]] / e;
EEg6[Step + (SStep) * (Nstep + 1)] = 2 * En6[EnList6[[1]]] / e;

DDos[Step + (SStep) * (Nstep + 1)] = Dos;
CCdos[Step + (SStep) * (Nstep + 1)] = Cdos;
CCtot[Step + (SStep) * (Nstep + 1)] = Ctot;
μμ[Step + (SStep) * (Nstep + 1)] = μc / e ;
nn[Step + (SStep) * (Nstep + 1)] = ntot;

(* Initialize conductance arrays *)
GG1[Step + (SStep) * (Nstep + 1)] = 0;
GG2[Step + (SStep) * (Nstep + 1)] = 0;
GG3[Step + (SStep) * (Nstep + 1)] = 0;
GG4[Step + (SStep) * (Nstep + 1)] = 0;
GG5[Step + (SStep) * (Nstep + 1)] = 0;
GG6[Step + (SStep) * (Nstep + 1)] = 0;
GG[Step + (SStep) * (Nstep + 1)] = 0;
Fanonum[Step + (SStep) * (Nstep + 1)] = 0;

μ1 = Δϕ; (* Set the condition for the energy of the leads *)
(*Nmodes=Nmax[μ1];*)
Nmodes = 3;

(* Total conductance array *)
Array[TnA, Nmodes];
```

```
(* Loop for different modes *)
For[Nq = 0, Nq < (Nmodes), Nq += 1,

 (* Transmission probabilities in different K valleys *)
 Sgn = Sign[3*Round[(n - m)/3] - (n - m)];
 Tn1[Nq] = If[Nq == 0, Tn[μl, μc, Sgn*Nq, L, W, Ay1[Θ], Sgn*α],
   Tn[μl, μc, Sgn*(Nq - Nq), L, W, If[Ay1[Θ] ≠ 0, (-1)^Nq*Sign[Ay1[Θ]]*(2*Pi/W + (-1)^Nq*Abs[Ay1[Θ]]),
     If[Sgn == 0, (-1)^(Nq-1)*2*Pi/W, (-1)^(Nq-1)*Sgn*2*Pi/W]], Sgn*α]];
 Tn2[Nq] = If[Nq == 0, Tn[μl, μc, Sgn*Nq, L, W, Ay2[Θ], Sgn*α],
   Tn[μl, μc, Sgn*(Nq - Nq), L, W, If[Ay2[Θ] ≠ 0, (-1)^Nq*Sign[Ay2[Θ]]*(2*Pi/W + (-1)^Nq*Abs[Ay2[Θ]]),
     If[Sgn == 0, (-1)^(Nq-1)*2*Pi/W, (-1)^(Nq-1)*Sgn*2*Pi/W]], Sgn*α]];
 Tn3[Nq] = If[Nq == 0, Tn[μl, μc, Sgn*Nq, L, W, Ay3[Θ], Sgn*α],
   Tn[μl, μc, Sgn*(Nq - Nq), L, W, If[Ay3[Θ] ≠ 0, (-1)^Nq*Sign[Ay3[Θ]]*(2*Pi/W + (-1)^Nq*Abs[Ay3[Θ]]),
     If[Sgn == 0, (-1)^(Nq-1)*2*Pi/W, (-1)^(Nq-1)*Sgn*2*Pi/W]], Sgn*α]];
 Tn4[Nq] = If[Nq == 0, Tn[μl, μc, -Sgn*Nq, L, W, -Ay1[Θ], -Sgn*α],
   Tn[μl, μc, -Sgn*(Nq - Nq), L, W, If[-Ay1[Θ] ≠ 0, (-1)^Nq*Sign[-Ay1[Θ]]*(2*Pi/W + (-1)^Nq*Abs[-Ay1[Θ]]),
     -If[Sgn == 0, (-1)^(Nq-1)*2*Pi/W, (-1)^(Nq-1)*Sgn*2*Pi/W]], -Sgn*α]];
 Tn5[Nq] = If[Nq == 0, Tn[μl, μc, -Sgn*Nq, L, W, -Ay2[Θ], -Sgn*α],
   Tn[μl, μc, -Sgn*(Nq - Nq), L, W, If[-Ay2[Θ] ≠ 0, (-1)^Nq*Sign[-Ay2[Θ]]*(2*Pi/W + (-1)^Nq*Abs[-Ay2[Θ]]),
     -If[Sgn == 0, (-1)^(Nq-1)*2*Pi/W, (-1)^(Nq-1)*Sgn*2*Pi/W]], -Sgn*α]];
 Tn6[Nq] = If[Nq == 0, Tn[μl, μc, -Sgn*Nq, L, W, -Ay3[Θ], -Sgn*α],
   Tn[μl, μc, -Sgn*(Nq - Nq), L, W, If[-Ay3[Θ] ≠ 0, (-1)^Nq*Sign[-Ay3[Θ]]*(2*Pi/W + (-1)^Nq*Abs[-Ay3[Θ]]),
     -If[Sgn == 0, (-1)^(Nq-1)*2*Pi/W, (-1)^(Nq-1)*Sgn*2*Pi/W]], -Sgn*α]];

 (* Average transmission for all K valleys *)
 TnA[Nq] = (Tn1[Nq] + Tn2[Nq] + Tn3[Nq] + Tn4[Nq] + Tn5[Nq] + Tn6[Nq])/6;

 (* The fano factor *)
 Fanonum[Step + (SStep)*(Nstep + 1)] += ((4*e^2)/(Pi*h))^(-1)*((4*e^2)/h)*TnA[Nq]*(1 - TnA[Nq]);

 (* Store the conductance data *)
 GG[Step + (SStep)*(Nstep + 1)] += ((4*e^2)/(Pi*h))^(-1)*((4*e^2)/h)* TnA[Nq];
 GG1[Step + (SStep)*(Nstep + 1)] += ((4*e^2)/(Pi*h))^(-1)*((4*e^2)/h)* Tn1[Nq]/6;
 GG2[Step + (SStep)*(Nstep + 1)] += ((4*e^2)/(Pi*h))^(-1)*((4*e^2)/h)* Tn2[Nq]/6;
 GG3[Step + (SStep)*(Nstep + 1)] += ((4*e^2)/(Pi*h))^(-1)*((4*e^2)/h)* Tn3[Nq]/6;
 GG4[Step + (SStep)*(Nstep + 1)] += ((4*e^2)/(Pi*h))^(-1)*((4*e^2)/h)* Tn4[Nq]/6;
 GG5[Step + (SStep)*(Nstep + 1)] += ((4*e^2)/(Pi*h))^(-1)*((4*e^2)/h)* Tn5[Nq]/6;
 GG6[Step + (SStep)*(Nstep + 1)] += ((4*e^2)/(Pi*h))^(-1)*((4*e^2)/h)* Tn6[Nq]/6;

]
]
]

AddRc[Rc_, Q_] := (((Q*((4*e^2)/(Pi*h)))^(-1) + Rc)^(-1))/((4*e^2)/(h));

(* Export data to desired directory *)
TB1 = Table[{VVg[n], εε[n], AAy1[n], AAy2[n], AAy3[n], AAy4[n], AAy5[n], AAy6[n], EEg1[n], EEg2[n],
    EEg3[n], EEg4[n], EEg5[n], EEg6[n], DDos[n], CCdos[n], CCtot[n], μμ[n], nn[n], AddRc[Rc, Re[GG1[n]]],
    AddRc[Rc, Re[GG2[n]]], AddRc[Rc, Re[GG3[n]]], AddRc[Rc, Re[GG4[n]]], AddRc[Rc, Re[GG5[n]]],
```

```
    AddRc[Rc, Re[GG6[n]]], AddRc[Rc, Re[GG[n]]], Re[Fanonum[n] / GG[n]]}, {n, 0, (Nstep + 1) * (Nεstep + 1) - 1, 1}];
TB2 = Prepend[TB1, {"Vg", "Str", "Ay1", "Ay2", "Ay3", "Ay1p", "Ay2p", "Ay3p", "Eg1", "Eg2", "Eg3", "Eg1p",
    "Eg2p", "Eg3p", "Dos", "Cdos", "Ctot", "EF", "n", "G1", "G2", "G3", "G1p", "G2p", "G3p", "G", "Fano"}];
SetDirectory[
 "D:\\Study\\Concordia University\\Champagne Group\\MSc Thesis\\Linxiang's Thesis\\Figures\\5. Appendices"]
Export["SWCNT_20210102_V01.dat", TB2, "Table"]
```

Out[122]= D:\Study\Concordia University\Champagne Group\MSc Thesis\Linxiang's Thesis\Figures\5. Appendices

Out[123]= SWCNT_20210102_V01.dat

Bibliography

[1] A. Bertoni, P. Bordone, R. Brunetti, C. Jacoboni, and S. Reggiani, *Quantum Logic Gates based on Coherent Electron Transport in Quantum Wires*, Phys. Rev. Lett. **84**, 5912 (2000).

[2] Y. Meir, N. S. Wingreen, and P. A. Lee, *Low-temperature transport through a quantum dot: The Anderson model out of equilibrium*, Phys. Rev. Lett. **70**, 2601 (1993).

[3] E. Mariani and F. von Oppen, *Electron-vibron coupling in suspended carbon nanotube quantum dots*, Phys. Rev. B **80**, 155411 (2009).

[4] D. Akinwande et al., *A review on mechanics and mechanical properties of 2D materials—Graphene and beyond*, Extreme Mech. Lett. **13**, 42 (2017).

[5] M.-F. Yu et al., *Strength and Breaking Mechanism of Multiwalled Carbon Nanotubes Under Tensile Load*, Science **287**, 637 (2000).

[6] R. Zhang, Y. Zhang, and F. Wei, *Controlled Synthesis of Ultralong Carbon Nanotubes with Perfect Structures and Extraordinary Properties*, Acc. Chem. Res. **50**, 179 (2017).

[7] R. Leturcq et al., *Franck–Condon blockade in suspended carbon nanotube quantum dots*, Nat. Phys. **5**, 327 (2009).

[8] G. G. Naumis, S. Barraza-Lopez, M. Oliva-Leyva, and H. Terrones, *Electronic and optical properties of strained graphene and other strained 2D materials: a review*, Rep. Prog. Phys. **80**, 096501 (2017).

[9] L. Banszerus et al., *Ballistic Transport Exceeding 28 μm in CVD Grown Graphene*, Nano Lett. **16**, 1387 (2016).

[10] M. M. Fogler, F. Guinea, and M. I. Katsnelson, *Pseudomagnetic Fields and Ballistic Transport in a Suspended Graphene Sheet*, Phys. Rev. Lett. **101**, 226804 (2008).

[11] F. Guinea, M. I. Katsnelson, and A. K. Geim, *Energy gaps and a zero-field quantum Hall effect in graphene by strain engineering*, Nat. Phys. **6**, 30 (2010).

[12] B. Amorim et al., *Novel effects of strains in graphene and other two dimensional materials*, Phys. Rep. **617**, 1 (2016).

[13] M. Settnes, J. H. Garcia, and S. Roche, *Valley-polarized quantum transport generated by gauge fields in graphene*, 2D Mat. **4**, 031006 (2017).

[14] Y.-H. Wu, T. Shi, G. J. Sreejith, and Z.-X. Liu, *Fermionic symmetry-protected topological state in strained graphene*, Phys. Rev. B **96**, 085138 (2017).

[15] Z.-Z. Cao, Y.-F. Cheng, and G.-Q. Li, *Strain-controlled electron switch in graphene*, Appl. Phys. Lett. **101**, 253507 (2012).

[16] A. L. Kitt, V. M. Pereira, A. K. Swan, and B. B. Goldberg, *Lattice-corrected strain-induced vector potentials in graphene*, Phys. Rev. B **85**, 115432 (2012).

[17] A. L. Kitt, V. M. Pereira, A. K. Swan, and B. B. Goldberg, *Erratum: Lattice-corrected strain-induced vector potentials in graphene [Phys. Rev. B 85, 115432 (2012)]*, Phys. Rev. B **87**, 159909 (2013).

[18] T. Guo, P. Nikolaev, A. Thess, D. T. Colbert, and R. E. Smalley, *Catalytic growth of single-walled manotubes by laser vaporization*, Chem. Phys. Lett. **243**, 49 (1995).

[19] S. Iijima and T. Ichihashi, *Single-shell carbon nanotubes of 1-nm diameter*, Nature **363**, 603 (1993).

[20] A. C. McRae, *Graphene Quantum Strain Transistors and Two-in-One Carbon Nanotube Quantum Transistors*, PhD thesis, (2018).

[21] M. J. Allen, V. C. Tung, and R. B. Kaner, *Honeycomb Carbon: A Review of Graphene*, Chem. Rev. **110**, 132 (2010).

[22] A. H. Castro Neto, F. Guinea, N. M. R. Peres, K. S. Novoselov, and A. K. Geim, *The electronic properties of graphene*, Rev. Mod. Phys. **81**, 109 (2009).

[23] M. Oliva-Leyva and G. G. Naumis, *Generalizing the Fermi velocity of strained graphene from uniform to nonuniform strain*, Phys. Lett. A **379**, 2645 (2015).

[24] A. Kretinin et al., *Quantum capacitance measurements of electron-hole asymmetry and next-nearest-neighbor hopping in graphene*, Phys. Rev. B **88**, 165427 (2013).

[25] J.-C. Charlier, X. Blase, and S. Roche, *Electronic and transport properties of nanotubes*, Rev. Mod. Phys. **79**, 677 (2007).

[26] E. A. Laird et al., *Quantum transport in carbon nanotubes*, Rev. Mod. Phys. **87**, 703 (2015).

[27] J. W. G. Wilder, L. C. Venema, A. G. Rinzler, R. E. Smalley, and C. Dekker, *Electronic structure of atomically resolved carbon nanotubes*, Nature **391**, 59 (1998).

[28] J. W. Ding, X. H. Yan, and J. X. Cao, *Analytical relation of band gaps to both chirality and diameter of single-wall carbon nanotubes*, Phys. Rev. B **66**, 073401 (2002).

[29] Y. Matsuda, J. Tahir-Kheli, and W. A. Goddard, *Definitive Band Gaps for Single-Wall Carbon Nanotubes*, The Journal of Physical Chemistry Letters **1**, 2946 (2010).

[30] K. Grove-Rasmussen, H. I. Jørgensen, and P. E. Lindelof, *Fabry–Perot interference, Kondo effect and Coulomb blockade in carbon nanotubes*, Physica E **40**, 92 (2007).

[31] Y. Jiang et al., *Visualizing Strain-Induced Pseudomagnetic Fields in Graphene through an hBN Magnifying Glass*, Nano Lett. **17**, 2839 (2017).

[32] Y. Efroni, S. Ilani, and E. Berg, *Topological Transitions and Fractional Charges Induced by Strain and a Magnetic Field in Carbon Nanotubes*, Phys. Rev. Lett. **119**, 147704 (2017).

[33] D. Metten, G. Froehlicher, and S. Berciaud, *Monitoring electrostatically-induced deflection, strain and doping in suspended graphene using Raman spectroscopy*, 2D Mat. **4**, 014004 (2017).

[34] E. D. Minot, Y. Yaish, V. Sazonova, and P. L. McEuen, *Determination of electron orbital magnetic moments in carbon nanotubes*, Nature **428**, 536 (2004).

[35] N.-K. Chang, C.-C. Su, and S.-H. Chang, *Fabrication of single-walled carbon nanotube flexible strain sensors with high sensitivity*, Appl. Phys. Lett. **92**, 063501 (2008).

[36] A. C. McRae, G. Wei, and A. R. Champagne, *Graphene Quantum Strain Transistors*, Phys. Rev. Appl. **11**, 054019 (2019).

[37] G. Wei, A. C. McRae, and A. R. Champagne, *Quantum Transport Strain Engineering in Graphene*, In Preparation (2021).

[38] N. Agrait, A. L. Yeyati, and J. M. van Ruitenbeek, *Quantum properties of atomic-sized conductors*, Phys. Rep. **377**, 81 (2003).

[39] A. R. Champagne, A. N. Pasupathy, and D. C. Ralph, *Mechanically Adjustable and Electrically Gated Single-Molecule Transistors*, Nano Lett. **5**, 305 (2005).

[40] J. O. Island, V. Tayari, A. C. McRae, and A. R. Champagne, *Few-Hundred GHz Carbon Nanotube Nanoelectromechanical Systems (NEMS)*, Nano Lett. **12**, 4564 (2012).

[41] M. T. Postek, *An approach to the reduction of hydrocarbon contamination in the scanning electron microscope*, Scanning **18**, 269 (1996).

[42] T. Yamada et al., *Size-selective growth of double-walled carbon nanotube forests from engineered iron catalysts*, Nat. Nanotechnol. **1**, 131 (2006).

[43] A. C. McRae, V. Tayari, J. M. Porter, and A. R. Champagne, *Giant electron-hole transport asymmetry in ultra-short quantum transistors*, Nat. Commun. **8**, 15491 (2017).

[44] V. Tayari, *Quantum charge transport in 10-nanometer scale suspended graphene transistors*, PhD thesis, (2014).

[45] F. M. D. Pellegrino, G. G. N. Angilella, and R. Pucci, *Transport properties of graphene across strain-induced nonuniform velocity profiles*, Phys. Rev. B **84**, 195404 (2011).

[46] J. Tworzydło, B. Trauzettel, M. Titov, A. Rycerz, and C. W. J. Beenakker, *Sub-Poissonian Shot Noise in Graphene*, Phys. Rev. Lett. **96**, 246802 (2006).

[47] V. M. Pereira, A. H. Castro Neto, and N. M. R. Peres, *Tight-binding approach to uniaxial strain in graphene*, Phys. Rev. B **80**, 045401 (2009).

[48] F. A. Chaves, D. Jiménez, A. W. Cummings, and S. Roche, *Physical model of the contact resistivity of metal-graphene junctions*, J. Appl. Phys. **115**, 164513 (2014).

[49] S. Heinze et al., *Carbon Nanotubes as Schottky Barrier Transistors*, Phys. Rev. Lett. **89**, 106801 (2002).

[50] M. A. H. Vozmediano, M. I. Katsnelson, and F. Guinea, *Gauge fields in graphene*, Phys. Rep. **496**, 109 (2010).

[51] S.-M. Choi, S.-H. Jhi, and Y.-W. Son, *Effects of strain on electronic properties of graphene*, Phys. Rev. B **81**, 081407 (2010).

[52] Y. Wu et al., *Quantum Behavior of Graphene Transistors near the Scaling Limit*, Nano Lett. **12**, 1417 (2012).

[53] E. B. Kolomeisky, H. Zaidi, and J. P. Straley, *Interplay of Aharonov-Bohm, chirality, and aspect-ratio effects in the axial conductance of a nanotube*, Phys. Rev. B **85**, 073404 (2012).

[54] G. D. Mahan, *Many-Particle Physics*, Springer US, (2000).

[55] S. Ilani, L. A. K. Donev, M. Kindermann, and P. L. McEuen, *Measurement of the quantum capacitance of interacting electrons in carbon nanotubes*, Nat. Phys. **2**, 687 (2006).

[56] L. Yang and J. Han, *Electronic Structure of Deformed Carbon Nanotubes*, Phys. Rev. Lett. **85**, 154 (2000).

[57] M. J. Biercuk, S. Ilani, C. M. Marcus, and P. L. McEuen, *Electrical Transport in Single-Wall Carbon Nanotuebs*, volume 111, pages 455–493, Springer, Berlin, Heidelberg, (2008).

[58] A. D. Smith et al., *Piezoresistive Properties of Suspended Graphene Membranes under Uniaxial and Biaxial Strain in Nanoelectromechanical Pressure Sensors*, ACS Nano **10**, 9879 (2016).

[59] S. Chun, Y. Choi, and W. Park, *All-graphene strain sensor on soft substrate*, Carbon **116**, 753 (2017).

[60] C. Yesilyurt, S. G. Tan, G. Liang, and M. B. A. Jalil, *Perfect valley filter in strained graphene with single barrier region*, AIP Adv. **6**, 056303 (2016).

[61] H. Yoo et al., *Reconfigurable Complementary Logic Circuits with Ambipolar Organic Transistors*, Sci. Rep. **6**, 35585 (2016).